

# Design and Implementation of a Modular Test Bed Platform for Hardware-In-the-Loop Simulation of Electric Vehicles

by

Martin Robert Kardasz

A thesis  
presented to the University of Waterloo  
in fulfillment of the  
thesis requirement for the degree of  
Master of Applied Science  
in  
Electrical and Computer Engineering

Waterloo, Ontario, Canada, 2019

© Martin Robert Kardasz 2019

I hereby declare that I am the sole author of this thesis. This is a true copy of the thesis, including any required final revisions, as accepted by my examiners.

I understand that my thesis may be made electronically available to the public.

## Abstract

Over the course of the last decade, electric vehicles have seen explosive growth and interest with public adoption and shifting research and development priorities by original equipment manufacturers towards these new powertrains. However, the development of electric vehicles remain costly due to new technologies being implemented in the vehicle with the final cost ultimately being passed down to consumers. This method of developing new products where the price does not justify the product in the eyes of consumers hinders the adoption of the next generation of environmentally friendly vehicles.

To verify electric vehicle drivetrain platforms and software models, test beds with specific capability to simulate the entire vehicle are required. Currently, an abundance of valuable engineering resources are dedicated to creating full-scale test beds and full-sized vehicles for testing. Only then, at this stage in the development cycle, are drivetrain tests conducted outside of simulation models. Getting to this first level of functional testing requires using valuable time waiting for components to be designed, manufactured, validated, and installed before the system can be tested. The full-scale vehicle test bed becomes expensive, consumes a lot of space, and cannot be reconfigured easily without changing key components.

Therefore, this thesis presents a systematic approach to down-scaling full-size electric vehicles' parameters and environmental conditions to a level that can be handled by a small-scale hardware-in-the-loop simulation test bed. The method for taking the results obtained from the test bed and scaling them back up to the full-size vehicle level are also examined for completion. The hardware-in-the-loop test bed is realized using a two-electric machine system. The electric machine responsible for the electric vehicle propulsion is the traction motor and is tasked with maintaining the vehicle speed. The other electric machine, directly coupled to the first machine, is controlled by the simulation environment. This machine is the load motor which emulates the vehicle operating environment including the forces acting on the vehicle. This motor also compensates for all losses experienced by the actual hardware setup.

A detailed explanation of the entire hardware-in-the-loop setup is discussed with specific details relevant to the system design. The modularity of the system, allowing each block of the setup to be easily replaced, and making the test bed highly re-configurable, is also discussed in detail.

## Acknowledgements

Firstly, I would like to express my deepest thanks and gratitude to my supervisor, Dr. Mehrdad Kazerani. This thesis project would not have been accomplished without his support, guidance, and empathy shown on too many levels to count. I am very grateful for the opportunity to learn, the enormous amount of trust given to me to get everything done, and the countless encouragements along the way that made this thesis project a success.

I would like to thank Dr. Mahmoud Allam for being such a great co-worker and friend. All the great inspiring conversations we have had about ideas, problems, and life, well into the morning hours countless times, have made the lab a great and fun place to work.

I would also like to thank Marten Pape for being a great co-worker and friend. He has also provided the base microcontroller code structure to make all the control modules run so robustly which would have taken countless hours to accomplish without his help. The entire lab setup would not have been possible without all those purchase orders coming in so quickly.

I would like to thank my mother, Barbara Kardasz, and brother, Philip Kardasz, for supporting and understanding the enormous time commitment required to get this project done.

I would like to thank my wife, Lily Kardasz, for all the love, patience, and support she has provided me with over the years. This thesis project would have been nothing without her understanding of the magnitude of time needed from start to end.

Finally, I would like to thank my father, Gregory Kardasz. I would have never started down this path if it wasn't for him.

## **Dedication**

To my wife, Lily, for always supporting and believing in me.

# Table of Contents

List of Tables	x
List of Figures	xi
Nomenclature	xiii
<b>1 Introduction</b>	<b>1</b>
1.1 Motivation . . . . .	1
1.2 Literature Review . . . . .	2
1.2.1 Hardware-in-the-Loop . . . . .	2
1.2.2 Scaling . . . . .	5
1.3 Objectives . . . . .	6
1.4 Organization of Thesis . . . . .	6
<b>2 Background Review</b>	<b>8</b>
2.1 Inverter Topology . . . . .	8
2.1.1 Voltage-Source Inverter . . . . .	8
2.1.2 Current-Source Inverter . . . . .	9
2.2 Pulse Width Modulation . . . . .	10
2.2.1 Sinusoidal PWM . . . . .	11
2.2.2 Space Vector PWM . . . . .	12

2.3	Variable Frequency Drives . . . . .	13
2.4	ABC- $\alpha\beta$ -DQ . . . . .	14
2.5	Current and Voltage Sensors . . . . .	14
<b>3</b>	<b>Scaling</b>	<b>16</b>
3.1	Vehicle and Motor Fundamentals . . . . .	16
3.2	Scaling factor . . . . .	17
3.3	Scaling Up . . . . .	22
3.3.1	Advantages . . . . .	23
3.4	Scaling Approach Verification . . . . .	24
3.5	Simulation Results . . . . .	25
<b>4</b>	<b>Hardware-in-the-Loop Test Bed Design</b>	<b>30</b>
4.1	System Layout . . . . .	30
4.2	Source . . . . .	30
4.3	AC/DC Converter . . . . .	32
4.3.1	Background . . . . .	32
4.3.2	Current and Voltage Sensors . . . . .	34
4.3.3	Filter Design . . . . .	34
4.3.4	Design of Soft-Start Circuit with Normal and Emergency Shutdowns	36
4.3.5	Complete AC/DC module . . . . .	37
4.4	DC/DC Converter . . . . .	37
4.4.1	Topology . . . . .	37
4.4.2	Duty Cycle Limits . . . . .	38
4.4.3	Controller Design . . . . .	41
4.4.4	Current and Voltage Sensors . . . . .	42
4.4.5	Filter Design . . . . .	42
4.4.6	System Hardware . . . . .	43

4.4.7	Complete DC/DC module . . . . .	44
4.5	DC/AC Design . . . . .	44
4.5.1	Topology . . . . .	44
4.5.2	Controller and Hardware . . . . .	47
4.5.3	Motor Cradle and Shaft . . . . .	47
4.5.4	Motor Control . . . . .	52
4.5.5	Slip . . . . .	54
4.5.6	D-Axis Flux . . . . .	54
4.5.7	Motor Power . . . . .	55
4.5.8	Quadrature Encoder Pulse . . . . .	55
4.5.9	Current and Voltage Sensors . . . . .	56
4.5.10	Motor Operating Regions . . . . .	56
4.5.11	Complete DC/AC module . . . . .	57
4.6	Communication . . . . .	59
4.7	HIL Test Bed Results . . . . .	60
<b>5</b>	<b>Result Analysis</b>	<b>64</b>
5.1	System Layout . . . . .	64
5.2	Scaled Result Comparison . . . . .	64
5.2.1	Maximum Power . . . . .	65
5.2.2	Maximum Speed . . . . .	68
5.2.3	Maximum Torque . . . . .	72
<b>6</b>	<b>Conclusion and Recommendations</b>	<b>76</b>
6.1	Conclusion . . . . .	76
6.2	Recommendations . . . . .	77
	<b>References</b>	<b>79</b>



<b>APPENDICES</b>	<b>83</b>
<b>A Inductor Core Windings</b>	<b>84</b>
A.1 AC/DC Inductor Core Winding . . . . .	84
A.2 DC/DC Inductor Core Winding . . . . .	87
<b>B Main Controller Code</b>	<b>90</b>
B.1 AC/DC Controller Code . . . . .	90
B.2 DC/DC Controller Code . . . . .	91
B.3 DC/AC Speed Controller Code . . . . .	93
B.4 DC/AC Torque Controller Code . . . . .	97
<b>C Sensor Design and BOM</b>	<b>102</b>
C.1 Sensor Design Schematic . . . . .	102
C.2 AC/DC Module Sensor BOM . . . . .	105
C.3 DC/DC Module Sensor BOM . . . . .	107
C.4 DC/AC Module Sensor BOM . . . . .	108
<b>D Induction Machine Derivations</b>	<b>109</b>
D.1 Slip and Torque Derivation . . . . .	109
D.2 D-Axis Rated Flux Derivation . . . . .	112
<b>E Mechanical Design of Motor Cradle and Shaft</b>	<b>114</b>
E.1 Motor Cradle Mechanical Drawings . . . . .	114
E.2 Motor Shaft Mechanical Drawings . . . . .	119
<b>F AC/DC Module Soft-Start Circuit Derivations</b>	<b>120</b>
F.1 Capacitor Discharge Level . . . . .	120
<b>G Fiber Optic BOM</b>	<b>123</b>
G.1 Fiber Optic Transmitter BOM . . . . .	123
G.2 Fiber Optic Receiver BOM . . . . .	124

# List of Tables

3.1	Full-size and Scaled Vehicle Parameters . . . . .	27
4.1	Advanced Motors and Drives ACX-2043 Induction Motor Specifications . .	46
5.1	UDDS Cycle at Maximum Power (195 Seconds) Comparing Theoretical, Simulation, and Test Bed Results . . . . .	68
5.2	UDDS Cycle at Maximum Speed (240 Seconds) Comparing Theoretical, Simulation, and Test Bed Results . . . . .	72
5.3	UDDS Cycle at Maximum Torque (454 Seconds) Comparing Theoretical, Simulation, and Test Bed Results . . . . .	75
C.1	AC/DC Module, AC Current Sensor BOM . . . . .	105
C.2	AC/DC Module, AC Voltage Sensor BOM . . . . .	105
C.3	AC/DC Module, DC Voltage Sensor BOM . . . . .	106
C.4	DC/DC Module, DC Current Sensor BOM . . . . .	107
C.5	DC/DC Module, DC Voltage Sensor BOM . . . . .	107
C.6	DC/AC Module, AC Current Sensor BOM . . . . .	108
C.7	DC/AC Module, AC Voltage Sensor BOM . . . . .	108
G.1	Fiber Optic Transmitter BOM . . . . .	123
G.2	Fiber Optic Receiver BOM . . . . .	124

# List of Figures

1.1	Signal Level HIL . . . . .	3
1.2	Power Level HIL . . . . .	3
1.3	Mechanical Level HIL . . . . .	4
2.1	Three-Phase Voltage-Source Inverter . . . . .	9
2.2	Three-Phase Current-Source Inverter . . . . .	10
2.3	Sinusoidal Pulse Width Modulation . . . . .	11
2.4	Space Vector PWM . . . . .	12
3.1	Forces Acting on the Vehicle . . . . .	17
3.2	Scaling Map . . . . .	18
3.3	UDDS Drive Cycle . . . . .	25
3.4	UDDS Drive Cycle Energy Consumption . . . . .	26
3.5	Test Bed Simulation Results of Scaled Vehicle . . . . .	29
4.1	Test Bed Setup . . . . .	31
4.2	AC/DC Module of Test Bed System . . . . .	33
4.3	AC/DC Soft-Start with Normal and Emergency Shutdowns . . . . .	38
4.4	Fiber Optic Transmitter and Receiver . . . . .	39
4.5	AC/DC Module of Test Bed . . . . .	40
4.6	Bidirectional Buck-Boost Converter Schematic . . . . .	41
4.7	Bidirectional Buck-Boost Converter Logic . . . . .	42

4.8	DC/DC Module of Test Bed . . . . .	45
4.9	DC/AC Speed Module of Test Bed . . . . .	48
4.10	DC/AC Torque Module of Test Bed . . . . .	49
4.11	Motor with Cradle . . . . .	50
4.12	Motor Cradle Coupling . . . . .	51
4.13	Motor Shaft . . . . .	51
4.14	Motor Shaft Coupling . . . . .	52
4.15	Synchronously Rotating Reference Frame Motor Schematics . . . . .	53
4.16	Induction Machine Modes of Operation . . . . .	57
4.17	DC/AC Module of Test Bed . . . . .	59
4.18	Test Bed Communication Scheme . . . . .	60
4.19	HIL Test Bed Results of Scaled Vehicle . . . . .	63
5.1	Simulation - UDDS Cycle at 195 Seconds Showing Maximum Power . . . . .	66
5.2	Test Bed - UDDS Cycle at 195 Seconds Showing Maximum Power . . . . .	67
5.3	Simulation - UDDS Cycle at 240 Seconds Showing Maximum Speed . . . . .	70
5.4	Test Bed - UDDS Cycle at 240 Seconds Showing Maximum Speed . . . . .	71
5.5	Simulation - UDDS Cycle at 454 Seconds Showing Maximum Torque . . . . .	73
5.6	Test Bed - UDDS Cycle at 454 Seconds Showing Maximum Torque . . . . .	74
C.1	AC Voltage and Current Sensor Schematic . . . . .	103
C.2	DC Voltage and Current Sensor Schematic . . . . .	103
D.1	Synchronously Rotating Reference Frame Motor Schematics . . . . .	110
E.1	Motor Cradle Mechanical Drawings . . . . .	118
E.2	Motor Shaft . . . . .	119

# Nomenclature

AC	Alternating Current
ADC	Analog-to-Digital Converter
BEV	Battery Electric Vehicle
BOM	Bill of Materials
CSI	Current Source Inverter
CVT	Continuously Variable Transmission
DC	Direct Current
DMA	Direct Memory Access
DTC	Direct Torque Control
DUT	Device-Under-Test
EMR	Energetic Macroscopic Representation
EPA	Environmental Protection Agency
EPDM	Ethylene Propylene Diene Monomer
EV	Electric Vehicle
FOC	Field Oriented Control
HIL	Hardware-In-the-Loop
I2C	Inter-Integrated Circuit

IC	Integrated Circuit
ICE	Internal Combustion Engine
IFOC	Indirect Field Oriented Control
IGBT	Insulated Gate Bipolar Transistor
kVA	kilo-Volt-Ampere
LED	Light Emitting Diode
OEM	Original Equipment Manufacturer
PCB	Printed Circuit Board
PLL	Phase Locked Loop
PWM	Pulse Width Modulation
QEP	Quadrature Encoder Pulse
RC	Remotely Controlled
RX	Receive
SCL	Serial Clock
SDA	Serial Data
SPWM	Sinusoidal Pulse Width Modulation
SVPWM	Space Vector Pulse Width Modulation
THD	Total Harmonic Distortion
TX	Transmit
UART	Universal Asynchronous Receiver-Transmitter
UDDS	Urban Dynamometer Driving Schedule
VSI	Voltage Source Inverter

# Chapter 1

## Introduction

### 1.1 Motivation

Over the past two decades, there have been many advancements in battery technology and in more robust electronic semiconductor technology. These advancements, combined with the increased interest in reducing global greenhouse gas emissions, and a growing environmental movement towards moving away from oil dependency have resulted in enhanced interest in the development of electric vehicles. This new generation of vehicles are finally able to compete with conventional internal combustion engine (ICE) vehicles with enhanced performance and declining research and development cost.

The traditional vehicle release cycle has been dominated by combustion-powered vehicles. Based on decades of developmental experience, minor improvements are done to each vehicular model generation resulting in an overall lower developmental cost. With the growing interest in electric vehicles, the propulsion system is very different than that of combustion vehicles. This change has resulted in ample resources being dedicated towards validating the powertrain and innovating methods for higher efficiency. The costs of new vehicle development are still very high and are usually reserved for original equipment manufacturers (OEMs), tiered suppliers, or large research groups who are able to afford such large-scale and expensive projects. Smaller organizations and academia must have adequate funding to support such projects, have very focused teams, and the time to complete these full-scale projects. Without all research groups being able to work on these projects, the development advancement is slowed down. This has resulted in vehicles that are comparatively more expensive than their ICE counterparts for a longer period of time.

The use of simulation software has allowed considerable reduction in the vehicular development time. Computing power is virtually unlimited and multiple instances of the same simulation with minor tweaks can be run in parallel simultaneously for iterative design approaches. Major mistakes can be caught early on in the design phases and corrected before initial prototypes are created. For the simulation to work properly, one must create or have the correct models to predict vehicle behavior in various driving conditions. When developing a new model, it is difficult to know if the simulation model is providing the correct behavior until the model is tested on hardware with the results being brought back into simulation and compared, resulting in a full-circle iteration design.

The models used for simulating electric vehicles currently on the market are found in commonly-used software programs. These models are constantly being refined for higher accuracy and updated to show information that is not available through physical measurements. To verify simulation models, practical test data must be obtained by running the software on hardware. Running these types of tests on the road with full-size hardware is time- and cost-prohibitive, along with being unfeasible due to the extreme difficulty of being able to reproduce all driving conditions. A technique known as hardware-in-the-loop (HIL) simulation is used to test and validate specific vehicle functions on an embedded system where the driving conditions can be controlled.

## 1.2 Literature Review

### 1.2.1 Hardware-in-the-Loop

Using a HIL simulation during engineering development stage is gaining popularity. It provides an effective environment and platform for the test and performance analysis of hardware devices and their control algorithms. New software models designed in simulation can be tested on the HIL test bed quickly and easily. Compared to real-world experiments, hardware-in-the-loop simulation is characterized by low cost, safety, and re-usability [1].

From literature, there are three main types of HIL setups for electric vehicles [2–5] comprised of:

- Signal Level
- Power Level
- Mechanical Level

The most basic type of setup, known as Signal Level, involves testing the device-under-test (DUT) by injecting signals from a simulation environment that represent sensor data



and having the simulation environment read the data coming back from the DUT as shown in Figure 1.1. The signals injected by the simulation environment would represent the data obtained from external sensors or devices.

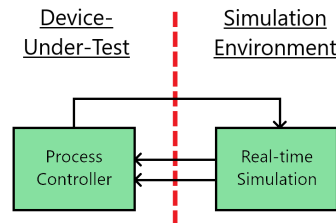


Figure 1.1: Signal Level HIL

An extension of the signal level HIL method involves adding a high-power section to the DUT and is known as Power Level HIL. The simulation environment still sends representative sensor data to the DUT controller but now the DUT controller controls a physical power electronic system with its own feedback loop. The simulation environment controls an electronic load which is interfaced to the power electronic system, as shown in Figure 1.2. The DUT is shown on the left hand side of the image where the controller and power electronics have a physically connected control and feedback loop. The power electronics system drives an electronic load which is controlled by a simulated environment. Signals between the simulated environment and the physical controller are exchanged to mimic a real system.

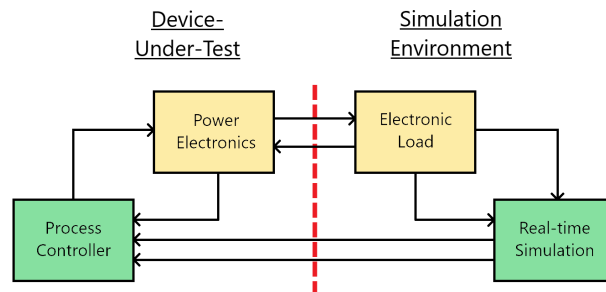


Figure 1.2: Power Level HIL

A further extension of this mode, referred to as Mechanical Level HIL, involves all the components of the power level HIL but with the addition of electrical machines. The electronic load in the simulation environment is removed and replaced with a load power

supply and electrical load machine which are connected together and controlled by the real time simulation. On the DUT, side, an electrical machine is added, which interfaces with the simulation environment through the electrical load machine. The power electronics interface with the electrical machine and both parts of the DUT are controlled by the process controller as shown in Figure 1.3. The configuration is similar to the power level HIL with the addition of a physical electrical machine for the DUT and a load machine in the simulated environment. Additional feedback signals are sent to the physical controller from the electrical machine. Feedback signals are also sent back from the load machine to the simulated environment controller.

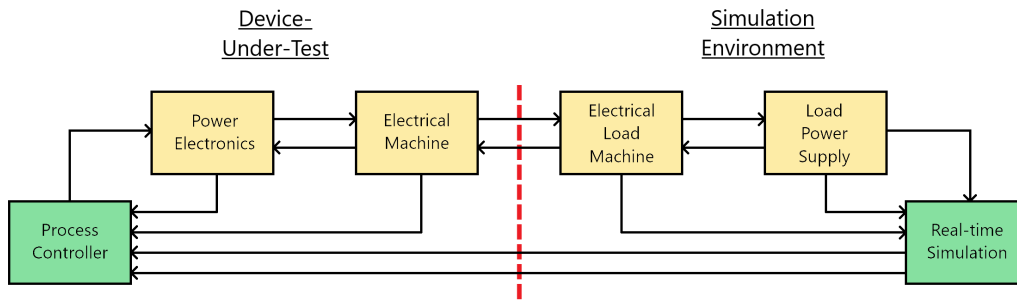


Figure 1.3: Mechanical Level HIL

Each of the HIL topologies increases system complexity. The HIL simulations contained fully within an emulated environment can be reconfigured endlessly, with the only limit being the speed at which instructions can be executed on the hardware controller. The HIL simulations with physical machines result in the most accurate real-world test results, but with the caveat of being able to operate in a very specific region according to the size and type of the machine being used. The results obtained offer the most insight into what an actual system will do in a real-world driving scenario once delays, nonlinearities, and code errors enter the decision making code of the DUT.

The immunity of the HIL to different hardware is dependent on the software models being developed. If the software models being developed are directly correlated with the hardware technology, then either an additional software model that bridges the two technologies together is needed or the hardware in the HIL system needs to change. Having a reduced scaled HIL design allows for quick changes to the hardware, especially once multiple modules have been created, by removing the existing module and putting in the new module needed for the desired test. However, if the software model being created is purely algorithmic to try and perform a current task more efficiently or differently, then the type of hardware does not matter. In addition, software models created for the same hardware

technology used in the HIL can also be used with the creation of a look-up-table to scale efficiency.

This thesis will follow the Mechanical Level HIL configuration. There will be two motors connected together on a test bed, whereby the DUT will be the traction motor and its controller. The load motor and its own controller will create the simulation environment necessary for the traction motor to operate in. Both the DUT and simulation environments will be created using the same hardware. The DUT and simulation environment will also be powered through their own individual power supplies to isolate any potential power problems. Both the simulation environment and DUT will run through a test cycle. The real-time simulation will follow a torque reference and use torque feedback of the load motor, while the process controller of the DUT will track a speed reference and use speed feedback from the traction motor.

## 1.2.2 Scaling

The construction of full-size test beds is expensive and consumes a lot of physical space. The use of smaller components allows the system to be much less expensive and can be constructed in a much smaller space. To obtain the same results as those of a full-size HIL system, there have been many approaches in the past on how to obtain results that can be extrapolated to full-size vehicles.

The most common methodology used is to physically scale down a vehicle to one similar in size to a remotely-controlled (RC) vehicle and perform actual tests on this miniaturized model [6–8]. The limitations of the RC model approach include limited availability of components to choose from to make the scaled vehicle. All the corresponding components of the model vehicle must also be available within the scaled range or a different scaling factor will need to be used where all the components within the desired range are available. The model vehicle also requires a relatively large area to navigate in to perform tests. The environment cannot be controlled precisely and is limited to what can be constructed physically for the RC vehicle to drive on. Finding corner edge cases also becomes problematic as all test cases cannot be reproduced with ease and the results for the same case will not be identical in subsequent repetition of the test.

Another scaling methodology exists where an Energetic Macroscopic Representation (EMR) model is used to represent the system where user-defined components are able to be scaled down according to the conservation of energy [9, 10]. This method is useful to examine system performance with many components acting together to verify system performance. The methodology involves using models available in simulation tools and it

is required that these models are accurate. The development of new models involves going back to the simulation tools, creating the model, and finding a means of verifying it, before implementing it using the EMR software.

## 1.3 Objectives

The main goal of this thesis is to create a low-cost HIL test bed for an academia laboratory capable of emulating any electric vehicle in a scaled down manner, running a test drive cycle, and scaling up the results back to the full-size electric vehicle. The test bed should also be capable of knowing its own losses and compensating for them during a test drive cycle so the results maintain accuracy. The HIL setup should also be comprised of easy to remove or replace modules for quickly changing or adding hardware as required. The test bed should also have a wide area of operation to allow as many scaling factors to be used as possible to ensure all test cycles can be run without changing modules.

Therefore, this thesis presents a modular HIL test bed with physical electric machines that have the ability to run a reduced-scale test drive cycle, where the scaled results can be taken to create full-scale vehicle results. The maximum power of any one module (power electronic converter or machine) is limited to  $6kVA$ . Every module is capable of bidirectional power transfer, and regenerative braking is possible, if required. Two degrees of scaling freedom are implemented to ensure all vehicles can be run on the HIL system.

## 1.4 Organization of Thesis

The structure of this thesis is organized as follows:

Chapter 2 discusses the background review associated with the technological aspects of the test bed as well as various design decisions considered. The important aspects of each module are broken down and analyzed as required.

Chapter 3 addresses the theoretical aspects of scaling the system parameters down to the model level and then down to the level that can be run on the test bed. The simulation results from running a full drive cycle test are shown and discussed.

Chapter 4 deals with the design of the HIL test bed setup. Each module and the corresponding design decisions are analyzed in detail. The results from a full drive cycle on the HIL system are shown and discussed.

Chapter 5 takes the simulation and HIL results from the drive cycle and scales them up to the level of a full-size vehicle. Analysis is conducted and the design of the scaled test bed is verified.

Chapter 6 presents the conclusions for this thesis and the recommendations for future work and ways for expanding the HIL test bed.

# Chapter 2

## Background Review

### 2.1 Inverter Topology

Battery-powered electric vehicles have a variable voltage-source, the battery, and either one or multiple three-phase AC motors to propel the vehicle. To have full control of the motors' speed and torque, there are two converter topologies that can be used, i.e., Voltage-Source Inverter (VSI) and Current-Source Inverter (CSI) [11].

#### 2.1.1 Voltage-Source Inverter

The circuit diagram of voltage-source inverter is shown in the Figure 2.1. There are six switches in a three-legged converter where each switch is able to turn on and off as desired. Anti-parallel diodes are added, if not built in the switch, to prevent the  $L \frac{di}{dt}$  voltage resulting from interruption of inductive load (e.g., motor) current from rising and destroying the switches. There are three switches on at any particular time, only one switch per leg. Turning on two switches in the same leg will result in a short circuit, or 'shoot through', across the DC-bus voltage source and will destroy either one or both of the switches in an over current event very quickly.

The control of VSI is based on a type of pulse width modulation (PWM), which will be discussed in the following section. The voltage on the DC bus is held regulated with the assistance of a capacitor while the switches are turned on and off, creating a pulsed ac voltage at the motor terminals. This technique results in a controllable low-frequency sinusoidal waveform (fundamental component) that is used to control the torque and thus

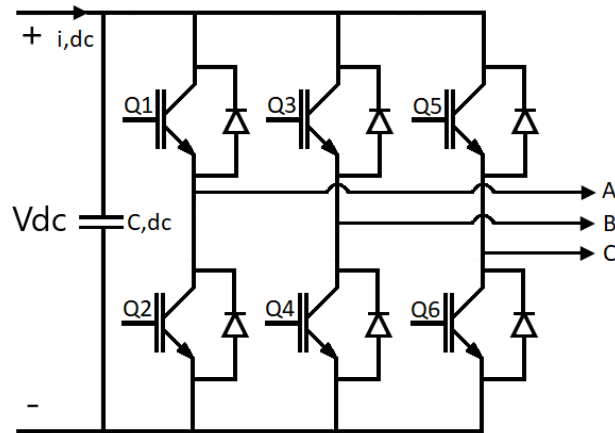


Figure 2.1: Three-Phase Voltage-Source Inverter

speed of the motor. Typically, the switching frequency is selected as high as possible for the best waveform quality results, but limited by the capabilities of switches and thermal management system. A high switching frequency results in moving the radiated and conducted harmonics to higher frequency bands, requiring smaller filtering components of lower ratings.

### 2.1.2 Current-Source Inverter

A current-source inverter operates on the principle of having a regulated current source on the DC-side. This is usually created by applying a variable voltage to a rather large inductance, whereby increasing the voltage will increase the current and vice versa. In the CSI topology, shown in Figure 2.2, there is a series diode connected to each switch to prevent application of a negative voltage across the switch. Also, there is a capacitive filter bank at the AC terminals to suppress the switching harmonics in the terminal currents.

The control of CSI is also based on a type of PWM. The switches are turned on and off at the duty cycle required to obtain the desired output voltage/current at the motor terminals. On the contrary to VSI, shoot through state is permitted in CSI. Also, CSI offers an inherent current-limiting feature in the event of a short-circuit fault due to continuous control on the DC-side current.

In an electric vehicle, fast dynamic response is desired. With a CSI topology, the inductor size proportionally affects the rate of change of current over time and thus reduces dynamic performance, while in a VSI topology, the DC link capacitor delivers instantaneous

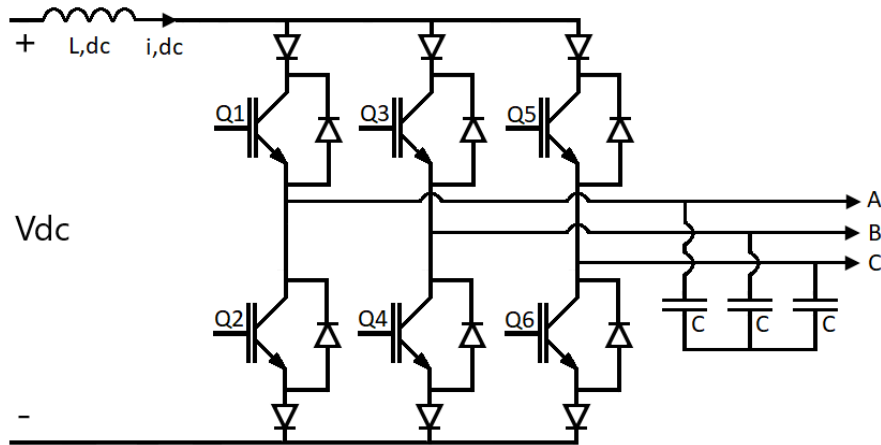


Figure 2.2: Three-Phase Current-Source Inverter

energy to the motor, maintaining high dynamic performance. From a physical standpoint, an inductor is also bulky when compared to a capacitor, and requires a lot of room to handle the maximum current. From a topology perspective, the conduction losses can be high due to the doubling of voltage drop due to series diodes and ohmic losses of the inductor. Finally, the CSI is also more expensive than VSI due to the addition of diodes, filter capacitors, and the large main inductor. VSI is very established from technological point of view and well-supported by research and abundance of control techniques. Therefore, VSI topology has been adopted in many industrial applications and will be the converter of choice in this thesis.

## 2.2 Pulse Width Modulation

The operation of the converter requires signals to be sent to the gates of the switches. In pulse width modulation (PWM) control of a VSI, the desired low-frequency waveform (or fundamental component) of AC-side voltage is modulated in the widths of the high-frequency pulses produced at the output terminals by switching the voltage of each phase between the upper and lower rails of DC-side voltages. At a single point in time, three switches are on, all in different legs of the converter. The possible combinations of on switches are: two top switches and one bottom switch, two bottom switches and one top switch, three top switches, or three bottom switches may be on. In addition, to prevent a shoot through event, there must be some dead time allocated to ensure the two switches in the same leg are never on at the same time. There are two main PWM approaches that



are commonly used in variable speed drives: sinusoidal PWM (SPWM) and space vector PWM (SVPWM) [12].

### 2.2.1 Sinusoidal PWM

Sinusoidal PWM (SPWM) compares three sinusoidal reference signals with a triangular carrier signal to generate the output signals that go to the gates of the transistors in the converter. The sinusoidal reference signals are spaced 120 degrees apart from one another. The switching frequency is dictated by the frequency of the carrier signal while the modulating signal frequency determines the fundamental frequency of the voltage applied to the machine. The intersection of the two signals decides the time of transition between on and off states of the transistor. In Figure 2.3,  $v_{tri}$  is the carrier signal and  $v_g$  is the modulating signal, shown for only one phase. For a three-phase system, there are three modulated waveforms compared with the same carrier waveform but offset by  $\pm 120$  degrees. Equation (2.1) defines modulation index, as the ratio of peak value of modulating signal to peak value of carrier signal. The largest possible modulation index that can occur in the linear region of operation is 1, where the carrier has the same amplitude as the modulating sine wave, to avoid overmodulation.

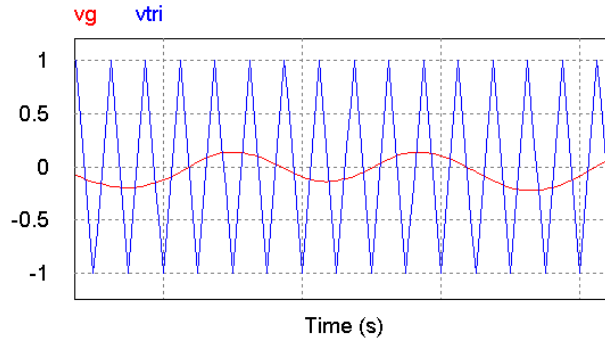


Figure 2.3: Sinusoidal Pulse Width Modulation

$$m_a = \frac{\widehat{V}_g}{\widehat{V}_{tri}} \quad (2.1)$$

For the line to line voltage, given by (2.2), to reach the rated (nameplate) AC voltage of the motor, the DC side voltage must be higher than the peak value of the desired line to line voltage. It should be noted that if the DC bus voltage is very close to its lower limit,

the control circuit will be working near maximum modulation index. This will cause the number of small duty cycle pulses to increase, resulting in loss of efficiency in the converter due to increased switching losses and dead time allotment between switching states of switches in the same leg.

$$V_{LL,rms,SPWM} = \frac{\sqrt{3}V_{DC}}{2\sqrt{2}}m_a \quad (2.2)$$

### 2.2.2 Space Vector PWM

Space Vector PWM (SVPWM) is a modulation scheme where the main goal is to derive the switching pattern based on a desired sinusoidal output voltage waveform. With six switches having two possible switching states, each, there are eight possible switch configurations that can be selected from to make the six individual active vectors, shown in Figure 2.4. By identifying the sector in which the desired voltage space vector falls, and resolving the desired vector along the adjacent active vectors, the time periods corresponding to switching states representing the adjacent active vectors and the zero vector, realizing the lowest number of switchings, can be determined.

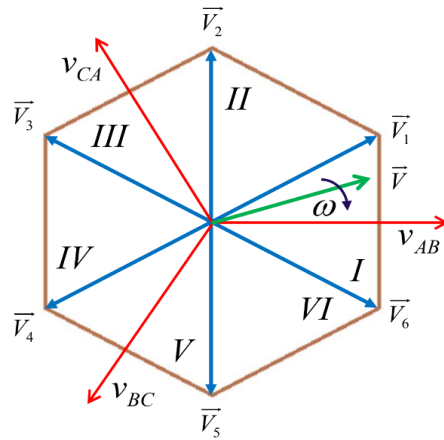


Figure 2.4: Space Vector PWM

As the resultant vector follows the inside of the hexagon, the magnitude at the midpoint between two vectors is lower than the magnitude directly on only one of the vectors. This creates a more square voltage waveform than what is achievable by SPWM [13]. The DC bus utilization is also higher, requiring a lower DC bus voltage to achieve the same line to

line voltage, as shown by (2.3) [14]. This results in a 15.47% higher DC bus utilization and reduces the total harmonic distortion (THD) in the system [15]. This allows the system to be more efficient [16]. Therefore, SVPWM will be used to control the traction and load motors in this thesis.

$$V_{LL,rms,SVPWM} = \frac{V_{DC}}{\sqrt{2}} m_a \quad (2.3)$$

## 2.3 Variable Frequency Drives

There are multiple approaches to controlling AC motors, consisting of scalar and vector control methods. Scalar control in induction machines is called Volts per Hertz (V/Hz) control and is one of the simplest forms of motor speed control. This control scheme can run in open loop where increasing the motor frequency will result in an increased voltage at the motor terminals. The ratio between the voltage and frequency is usually kept constant throughout this region of operation according to the motor nameplate ratings. With closed loop control, the motor speed can be measured, and the frequency can be increased to compensate for the error [17].

A more sophisticated control methodology can be subdivided into direct torque control (DTC) and Field Oriented Control (FOC). DTC involves calculating the motors flux, torque, and angle of the stator flux from the voltage and current sensors. The flux and torque errors are compared using two hysteresis comparators where the flux is compared with two discrete levels and the torque is compared with three discrete levels. The stator flux angle is discretized into six 60-degree sections to determine the firing pattern of the transistors [18].

Field Oriented Control turns all the time-varying parameters of the motor into DC motor-like parameters that can be more easily controlled. There are multiple ways in which the reference can be aligned for computations. The easiest of these in terms of motor control is the alignment of all parameters to the synchronously rotating reference frame where all computations are aligned with the electrical angular velocity of the stator magnetic field of fundamental frequency. The control scheme can be expanded even further into direct FOC and indirect FOC. In direct FOC, flux magnitude and angle feedback are calculated from the voltage and current models. In indirect FOC, the currents and rotor speed are measured first and then the flux space angle is derived through the summation of rotor speed and the slip speed. There is an extension of this method where no speed

sensor is used, known as Sensorless Field Oriented Control while the method utilizing a speed sensor is called Sensored Field Oriented Control [19].

In this thesis, both the speed and torque motors are controlled through Sensored Indirect Field Oriented Control aligned in the synchronously rotating reference frame.

## 2.4 ABC- $\alpha\beta$ -DQ

The control of the AC/DC and DC/AC converters is commonly performed in the direct-quadrature (DQ) reference frame. This is done by transforming the time varying variables from the ABC frame to a synchronously-rotating DQ frame, where the space vector does not rotate. The advantage of this approach is that in the DQ frame, at steady-state, variables such as voltages and currents assume constant values, making the control much less complicated. To go back to ABC frame, the reverse transformation is used. The DQ transformations are known as Park's transformations.

The ABC frame can also be expressed in a two-axis reference frame known as  $\alpha\beta$  where the  $\alpha$ -axis component is aligned with phase a and the  $\beta$ -axis component is orthogonal to the  $\alpha$ -axis, also known as the stator reference frame where the space vector now rotates synchronously with the ABC frame. Control in this reference frame is still difficult due to the time-varying components and will only be used on the DC/AC modules that utilize SVPWM as the rotating two axis reference frame makes it ideal for selecting space vectors automatically. The  $\alpha\beta$  transformations are also known as Clarke's transformations.

## 2.5 Current and Voltage Sensors

The voltage and current of the system can be measured in direct or indirect ways.

Direct sensing of AC voltages can be done through either a resistive or capacitive divider. Both topologies can be capacitively coupled with a DC bias before directly entering the analog-to-digital converter (ADC). DC voltage sensing does not require a DC bias as the voltage does not go below zero. For AC current measurements, a small valued resistor is required to be placed in series with the phase. The voltage drop across the resistor is amplified, biased, and fed to an ADC. The DC current measurement is done in the same way without the bias requirement.

Indirect ways of sensing the voltage and current rely on isolated topologies providing galvanic isolation between the primary and secondary sides. These sensors can either be

open-loop or closed-loop. Both types have a hall effect sensor mounted inside the air gap of the magnetic core which measures the magnetic field created by the primary side current and generates a proportional output voltage that is amplified and fed to an ADC. For voltage measurements, a high accuracy resistor is used to make a proportional current on the primary side and the same strategy mentioned above is used. Closed-loop sensors differ in the fact that the hall effect sensor injects a current into the secondary winding to zero the flux that is produced by the magnetic field in the primary winding current. This allows the output signal to be very immune to electrical noise, have a high accuracy, and compensate for any offsets developed over time. The added benefit of being isolated is providing protection to the operator which is a very high priority in the test lab setup [20].

The closed-loop hall effect voltage and current sensors are the sensor types that will be used in this thesis.

# Chapter 3

## Scaling

### 3.1 Vehicle and Motor Fundamentals

The design of the cars on the road today is dictated by the laws of physics. The size and shape of the vehicle greatly affects how it is able to respond to changes requested by the driver and how much the environment plays a role in affecting it. The forces acting on a vehicle can be divided into the following four main categories:

- Forward Force
- Rolling Resistance
- Gravitational Force
- Aerodynamic Drag

The forces mentioned are shown in Figure 3.1 acting on a simplified high-level model of the electric vehicle, when moving on a road making an angle  $\theta$  with the horizontal plane. This model will be the main focus of the scaling approach throughout this chapter.

Based on the model shown in Figure 3.1, the forces acting on the vehicle can be expressed by (3.1).

$$F = ma + \mu mg \cos(\theta) + mg \sin(\theta) + 0.5\rho C_d A_f (v + V_w)^2 \quad (3.1)$$

In (3.1),  $F$  is the total force acting on the vehicle,  $m$  vehicle's mass,  $a$  acceleration,  $\mu$  coefficient of friction,  $g$  gravitational acceleration,  $\theta$  road's angle with respect to the horizontal plane,  $\rho$  air density,  $C_d$  drag coefficient,  $A_f$  equivalent frontal area of the vehicle,  $v$  vehicle velocity, and  $V_w$  velocity of wind against the vehicle's movement.

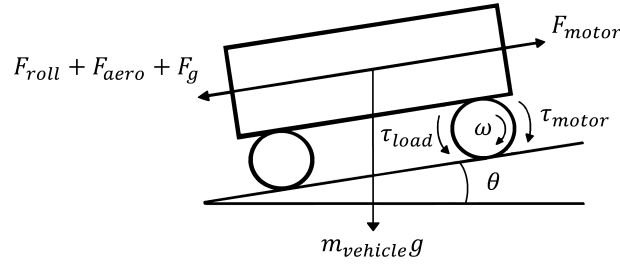


Figure 3.1: Forces Acting on the Vehicle

The power of an electric motor can be expressed by (3.2), where  $P$  is the motor power,  $\tau$  motor torque, and  $\omega$  angular velocity. This model remains the same regardless of the motor type being used.

$$P = \tau\omega \tag{3.2}$$

In this Chapter, the theory behind the proposed scaling approach is discussed in detail and shown through equations. The relationship between the full-size vehicle, the scaled vehicle, and the electric motors used on the test bed are also provided. The inverse scaling process, taking the results from the scaled model back to the full-size vehicle are also provided, and a way to take the test bed model straight to the full-size vehicle is also discussed. The relationship between the three different types of models are shown in Figure 3.2.

### 3.2 Scaling factor

A scaling factor can be introduced to (3.1) to scale down the individual vehicular parameters of the full-scale vehicle down to those of a scaled version of the vehicle. This scaling factor will focus on the individual vehicular parameters rather than scaling the vehicle geometrically. If a geometric scaling approach was used, physically creating a model vehicle may not be possible as all components may not be available. Hence, the idea behind scaling the individual vehicle parameters allows this system is to provide a simple, yet effective way to reproduce all important vehicular parameters on a smaller scale, making test and design validations easier, faster, and less expensive. For simplicity, a scaling factor of  $x$  will be applied to each of the individual parameters in (3.1), and by following the laws of kinematics, the mass, acceleration, velocity, and wind velocity are scaled by a factor of  $x$

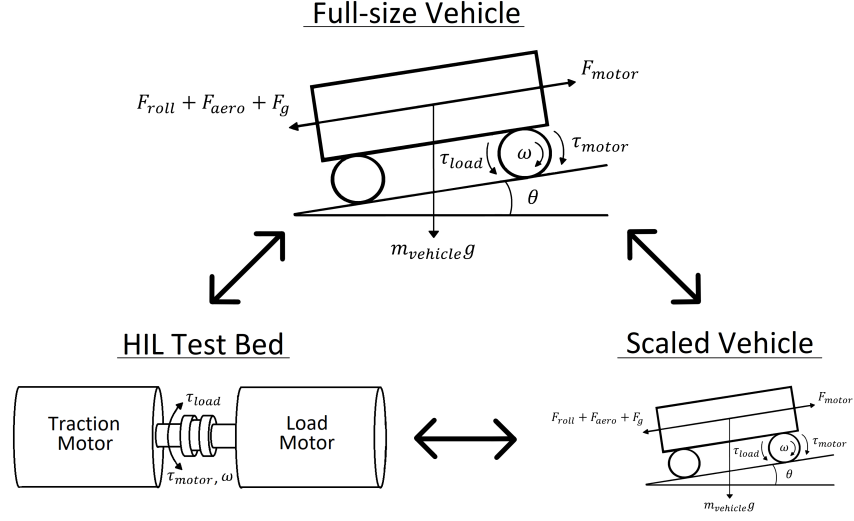


Figure 3.2: Scaling Map

while the frontal area is scaled by a factor of  $x^2$ . This is done by keeping time common between the original and scaled-down system. It should be mentioned that the time can also be scaled as a separate variable irrespective of the scaling factor  $x$ , but this option is outside the scope of this thesis.

The scaling factor does not have to be constant among all the various forces in the vehicular equation and can be different if a scaled physical model is to be made using available components. However, the total amount of energy of the full-scale vehicle has to be scaled to that of the scaled model using a constant factor and possible error be compensated accordingly in the physical model.

When scaling the full-size vehicular model, (3.3) is obtained. This equation obtains the vehicle force of the scaled model using only parameters of the full-size vehicle.

$$F_2 = \frac{(m_1 a_1 x^2 + \mu m_1 g \cos(\theta) x^3 + m_1 g \sin(\theta) x^3 + 0.5 \rho A_{f1} C_d v_1^2 + \rho A_{f1} C_d v_1 V_{w1} + 0.5 \rho A_{f1} C_d V_{w1}^2)}{x^4} \quad (3.3)$$

In (3.3), the parameters are the same as those described in (3.1) with  $x$  representing the scaling factor, subscript 1 the full-size vehicle and subscript 2 the scaled vehicle model.

This unidirectional scaling approach does not provide a useful means of using the results obtained from a simulation or test bed test cycle run to determine the full-size vehicle



test results. Under a normal use scenario, the full-size vehicle parameters are already known since the scaled model parameters were originally defined from them. To allow full capability of the system, it is useful to allow the full-size vehicle to be scaled down with the ability to change model parameters and scale the results back to full-size. An inverse transformation approach has been devised and is shown in (3.4) where the full-size vehicle force is obtained using only the model parameters.

$$F_1 = F_2x^4 - m_2a_2x^4 + m_2a_2x^2 - \mu m_2g \cos(\theta)x^4 + \mu m_2g \cos(\theta)x - m_2g \sin(\theta)x^4 + m_2g \sin(\theta)x \quad (3.4)$$

The parameters in (3.4) are the same as those described in down-scaling represented by (3.3). Based on these two equations, the vehicle parameters can be scaled bidirectionally in terms of forces. To obtain mechanical power, the appropriate full-size or scaled velocity factor must be multiplied by the respective force equation.

The velocity factor can be found in (3.5) where the scaling factor is still chosen to be  $x$ .

$$v_2 = \frac{v_1}{x} \quad (3.5)$$

The power of the full-size or scaled vehicle can now be obtained using (3.6) where  $P$  is the vehicle power,  $F$  vehicle force, and  $i$  subscript assuming values 1 and 2 when representing full-size vehicle and scaled vehicle, respectively.

$$P_i = F_i v_i \quad (3.6)$$

The linear power of the vehicle, full-size or scaled, can be transferred to the rotational domain using (3.7).

$$P = \tau\omega = J\alpha\omega \quad (3.7)$$

In (3.7),  $P$  is power,  $\tau$  torque,  $\omega$  angular velocity,  $J$  moment of inertia, and  $\alpha$  angular acceleration. The unknown parameters, inertia and angular velocity, can be obtained by examining the internal structure of the motor. For the test bed setup, two motors, both ACX-2043 from Advanced Motors and Drives are used. The inertial components of the motors are made up from two solid cylinders inside each motor. The large solid cylinder is

the rotor of the motor and the other solid cylinder is a small protrusion for the connection point to the motor shaft. The inertia of the motor can be represented by (3.8).

$$J_{motor} = J_{rotor} + J_{shaft} + J_{coupling} = \frac{\tau}{\alpha} = \frac{\tau r_{motor}}{a} = \frac{m_r r_r^2}{2} + \frac{m_s r_s^2}{2} + \frac{m_c r_c^2}{2} \quad (3.8)$$

In (3.8),  $J$  is the motor inertia,  $\tau$  motor torque,  $\alpha$  motor acceleration,  $r_{motor}$  motor rotor radius,  $a$  linear acceleration,  $r$  solid cylinder radius,  $m$  solid cylinder mass, where subscripts  $r$ ,  $s$ , and  $c$  refer to rotor, shaft, and coupling, respectively. Since the velocity and radius are both scaled by the same scaling factor, the angular velocity cannot be scaled in both full-size and scaled vehicle models when following the laws of kinematics, as shown in (3.9).

$$\omega = \frac{v}{r} = \frac{v_1}{r_1} = \frac{\frac{v_1}{x}}{\frac{r_1}{x}} = \frac{v_2}{r_2} \quad (3.9)$$

In (3.9),  $\omega$  is the angular velocity,  $v$  velocity,  $r$  radius,  $x$  scaling factor, and subscripts 1 and 2 denote full-size and scaled vehicle models, respectively. When transferring the vehicle models from full-size vehicle to test bed, the angular velocity will not change as shown above.

There are two main problems with this that need to be addressed. The first issue is that the actual motor in the full-size vehicle may be able to spin at a much higher speed than the motors on the test bed. The second issue is the inertial mismatch between the full-size vehicle and the test bed model.

The first issue can be addressed by installing a physical gearbox or implementing one in software. The majority of transmissions in electric vehicles are based on a single speed gearbox with a reduction gear ratio. The reason for only one gear is to maintain high efficiency of the motor across its entire operating range. However, in a test bed setup that is capable of testing different vehicles, the full-size vehicle gearing ratio can differ among vehicle models and manufacturers. To maintain a modular test bed setup, a single speed gearbox cannot be used, as the output angular speed will not match all full-size vehicle motors. Another option is to implement a continuously variable transmission (CVT). Compared with single speed gearboxes, CVT transmissions with a belt drive have a lower efficiency due to finding a middle ground between choosing between a higher clamping force or more slip in the belt [21]. To counter these inefficiencies, there has been some developmental work to improve the efficiency compared to other gearing approaches [22].

Another option to change the angular velocity of the test bed system is to implement a gearbox in software. The advantage of this strategy compared to the one above is that it can be easily reconfigured to run at different speeds. This maintains the same shaft output power. However, due to the different motor operating points, the efficiency is different and would need to be compensated for depending on the type of test being done. With the test bed setup having back to back motors, this is not a very large problem as the second motor can be used to compensate for the efficiency loss or gain in the first motor. This is the approach that is taken in this thesis to maintain the modularity of the system.

The second issue is due to the inertial mismatch between full-size and test bed motors. Since the test bed does not have the same inertia as the scaled vehicle model, having two motors coupled together allows the load motor to perform various functions in the system setup. The main function is to emulate the environment so that the traction motor tracks the same energy profile that the full-size vehicle would have. Secondly, the inertia of the entire system can be compensated for through the addition or subtraction of the torque that the traction motor would see. Thirdly, any additional losses that are present in the bench setup can also be compensated for by the same motor.

When implementing a gearbox, whether physically or in software, the speed and torque are changed proportionally, but the inertia is changed by the square of the gear ratio [23], as shown by (3.10).

$$J_{total} = J_T + J_{G1} + \left(\frac{N_1}{N_2}\right)^2 [J_{G2} + J_{C+L} + J_{virtual}] \quad (3.10)$$

In (3.10),  $J_{total}$  is the test bed inertia,  $J_T$  inertia of the traction motor,  $J_{G1}$  inertia of the gear closest to the traction motor,  $N_1$  gear ratio closest to the traction motor,  $N_2$  gear ratio on the load motor side,  $J_{G2}$  inertia of the gear closest to the load motor,  $J_{C+L}$  coupling and load motor inertia, and  $J_{virtual}$  virtual inertia that is required to be added to or subtracted from the total system inertia.

Substituting the inertia,  $J$ , in (3.8) into (3.7) allows the total power of the test bed to be obtained. The test bed traction motor power must match that of the scaled model found in (3.6) while maintaining the conservation of energy. With a gearbox implemented in software, both motors still spin at the same speed as they are coupled together, and this must be taken into account in the inertia calculation. Depending on the scaling factor chosen for the scaled model, and the gearbox ratio, the amount of virtual inertia that is added or removed to maintain energy conservation will differ on the test bed. The load motor will also be compensating for all system losses simultaneously that are not included in the inertia calculation.

### 3.3 Scaling Up

To maintain the usefulness of the scaling model, it is imperative to be able to scale the results of tests on the test bed back to the full-size vehicle and to the scaled vehicle. The equations above have been focused mainly on scaling the vehicle down to a small-scale model and then to the test bed level through the addition or removal of virtual inertia. It was briefly touched upon earlier that a bidirectional scaling for the linear model exists where the full-size vehicle parameters can be used to obtain scaled model power and the scaled parameters can be used to obtain full-size power.

The method to scale back up to the full-size force vehicle straight from the test bed involves utilizing the traction motor torque shown by (3.11).

$$F_1 = \frac{\tau_2 x^4}{G_2 r_2} \quad (3.11)$$

In (3.11),  $\tau_2$  is the test bed torque,  $x$  scaling factor,  $r_2$  test bed motor's rotor diameter,  $G_2$  test bed virtual gearbox ratio, and subscript 2 represents the scaled vehicle. To find the full-size vehicle torque, (3.11) is multiplied by the full-size vehicle motor radius,  $r_1$ , and divided by the full-size vehicle gear ratio,  $G_1$  resulting in (3.12).

$$\tau_1 = \frac{F_1 r_1}{G_1} \quad (3.12)$$

The scaling from the test bed model to the scaled down vehicle can be done using the test bed torque, speed, and scaling factor as shown by (3.13).

$$F_2 = \frac{\tau_2 \omega_2}{v_2} + \left( \frac{m_1 a_1 (x^2 - 1) + (\mu m_1 g \cos(\theta_1))(x^3 - 1) + (m_1 g \sin(\theta_1))(x^3 - 1)}{x^4} \right) \quad (3.13)$$

In (3.13),  $\tau_2$  is the torque,  $\omega_2$  rotational speed,  $v_2$  vehicle linear velocity,  $m_1$  vehicle mass,  $a_1$  vehicle acceleration,  $x$  the scaling factor,  $\mu$  coefficient of friction,  $g$  gravitational acceleration, and  $\theta_1$  angle with respect to the road.

The speed,  $\omega$ , between the test bed model and scaled down vehicle requires no scaling and remains the same.

Finally, the speed of both the test bed and scaled down vehicles can also be easily brought up to a full-size vehicle as shown in (3.14).

$$\omega_{rpm,1} = \frac{\omega_{rpm,2} r_2 G_1 G_2 x}{r_1} \quad (3.14)$$

In (3.14),  $\omega_{rpm}$  is the speed in rpm,  $r$  motor shaft radius,  $G$  gearbox ratio,  $x$  scaling factor, subscript 1 represents the full-size vehicle and subscript 2 represents the scaled vehicle model/test bed model.

The method to scale up the results of the hardware-in-the-loop system is straight forward. The inertia of the system was already compensated for in the down scaling procedure to obtain results that can be easily brought back up to the full-size model. When following these equations to get the final output, it can easily be verified if the full-size vehicle meets or fails to meet any design criteria and by what margin.

### 3.3.1 Advantages

Some of the advantages of using the scaling approach to create a scaled-down test bed are as follows:

- Smaller Space
- Ease of Reconfiguration
- Shorter Time
- Lower Cost
- Less Personnel

The main advantage of creating a physical test bed is the ability to verify and validate simulation models without building the full-size vehicle model. This allows new designs to be iterated very quickly before a full-size version of the model is built. Testing the behavior of the system with rotating components will lead to a more realistic insight, as rotational inertia can have a significant effect on the results. The electrical power consumption of the test bed traction motor can also be measured, and correlated via a lookup table to that of the full-size vehicle, and scaled up to a full-size vehicle. This can be done by knowing the power, torque, and rpm curves versus efficiency of both scaled and full-size motor. This information is known from the motor manufacturer or can be easily mapped through the motor operating range.

Another advantage of a test bed setup is in the ability to easily reconfigure the design. Additional physical components, such as a battery pack, can be used if required, or these components can be emulated in software. With the addition of a battery pack, tests such as life cycle testing can be done. If a physical battery is added, a reduced version can

be connected to emulate the scaled vehicle power draw or charge. The test bed with the battery pack may also be moved into an environmental chamber to conduct vehicle range testing.

The ease of reconfiguration and small size of the system also save time. When adding a new component to the test bed, or replacing an existing section, the components can easily be linked together with a few connections in a short amount of time. However, in a full-scale vehicle, the components may not have the room required to fit and may need extensive work and time to be ready for use again.

The scaling approach brings the cost of development and research down to a level that is more affordable by educational institutions, small companies, and even individuals, since large teams of personnel are not required. New concepts and models can be quickly validated and iterated upon in a short time frame. This aids in speeding up innovation and shortens the time-to-market for the technology.

### 3.4 Scaling Approach Verification

To demonstrate the performance and capability of the two-way scaling approach described in this chapter, a 2016 Tesla Model S Performance (85kWh) is used as the test vehicle. The purpose of scaling the parameters of an existing vehicle down to those that can be used on the test bed has two main purposes. The first is to verify that the math and methodology of scaling the vehicular parameters down to the scaled model and then back up to the full-size vehicle is working. The second purpose is to verify the functionality of the test bed by comparing the results to those obtained in simulation. By confirmation of matching results, the HIL system can be confirmed to work as intended. New software models can now be created and the test bed can be used to validate them with certainty.

To evaluate the performance of the vehicle, the Environmental Protection Agency (EPA) Urban Dynamometer Driving Schedule (UDDS) drive cycle for battery electric vehicles (BEVs) is used. This drive cycle, shown in Figure 3.3 goes through an abundance of speed changes [24].

The full-size vehicle parameters have been scaled by the scaling factor and the model parameters following the scaling procedure have been recorded in Table 3.1. A constant wind velocity of  $5m/s$  against the car has been set throughout the entire drive cycle. No inclination angle has been set throughout the drive cycle. These two parameters have been set for consistency and to demonstrate that the external parameters are indeed taken into account during the simulation.

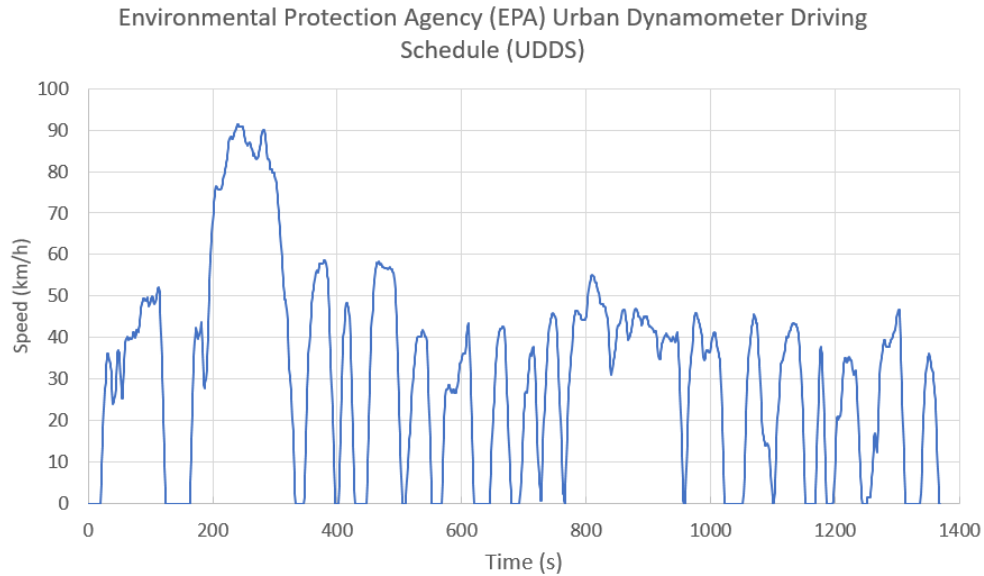
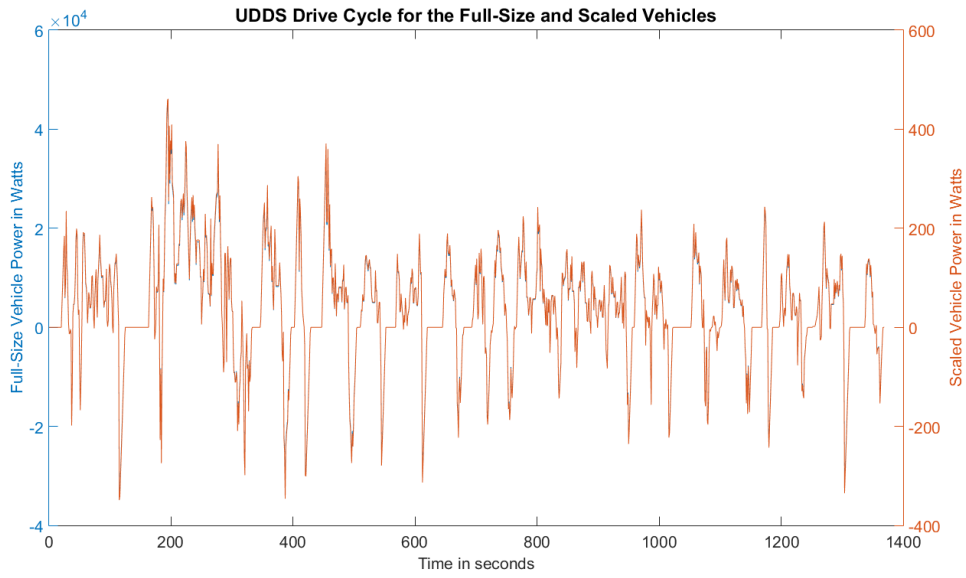


Figure 3.3: UDDS Drive Cycle

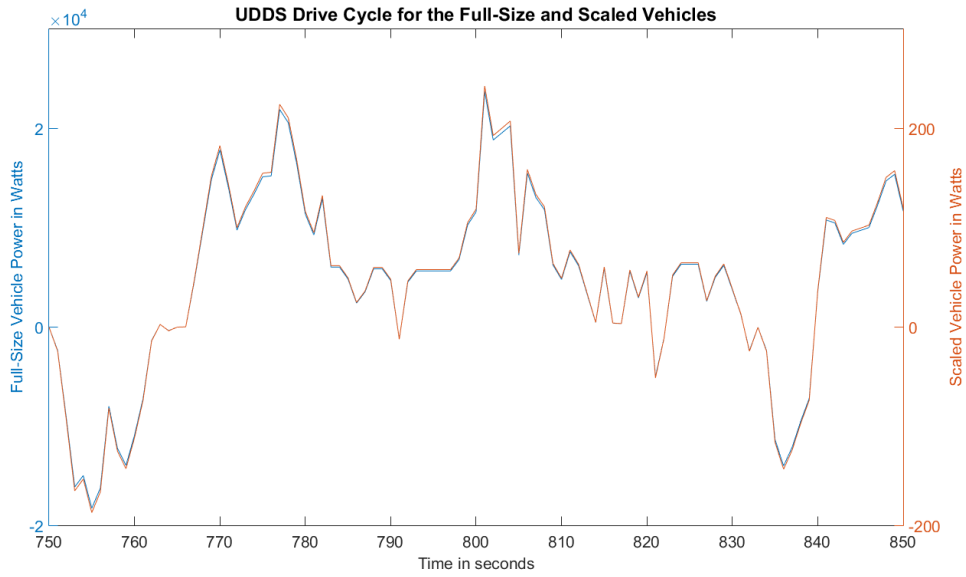
To validate the procedure of scaling the full-size vehicle, the conservation of energy must be maintained. The power of the full-size vehicle can be overlaid in time with the power of the scaled vehicle, as shown in Figure 3.4(a). The area under each curve is the energy of each vehicle. Looking at a zoomed-in portion of the cycle in Figure 3.4(b), it can be seen the rising and falling slopes are the same. The peaks are slightly offset with respect to one another due to a vertical gain mismatch between the two graphs. The zero-crossing point is the same for both, showing the energy is indeed conserved. The scaling equation can now be used for the development of a model vehicle or can be translated into the HIL test bed.

### 3.5 Simulation Results

The UDDS drive cycle allows the capabilities of the scaling mechanism and test bed traction motor to be evaluated extensively. For the purposes of the simulation, the entire model was validated. This includes the mechanical coupling between the two motors, the control scheme for the speed and torque references, and power flow. The simulation was conducted in Powersim PSIM, where each element of the system was modeled separately, and the entire controller was created from discrete components. The simulation results of the



(a) Total Drive Cycle



(b) Zoomed in Drive Cycle Section

Figure 3.4: UDDS Drive Cycle Energy Consumption

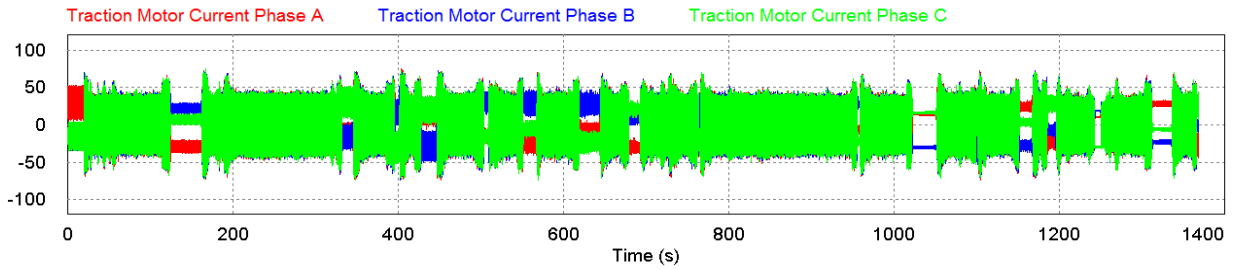


Table 3.1: Full-size and Scaled Vehicle Parameters

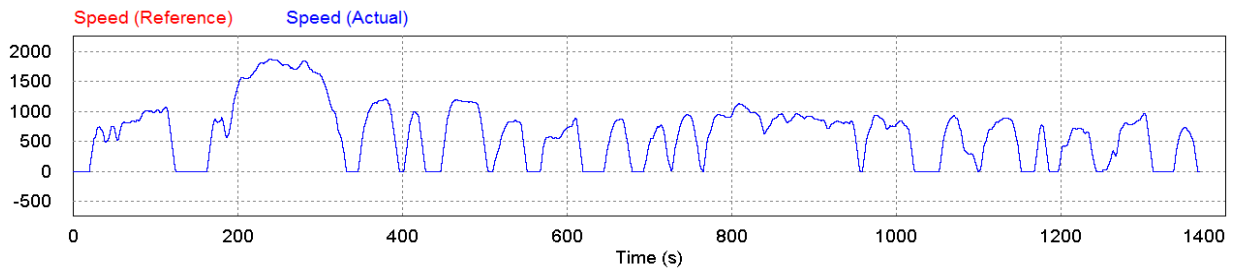
2016 Tesla Model S Performance (85kWh)		
Parameter	Full-size	Scaled
Mass, $m$ (kg)	2,108	843.2
Maximum Acceleration, $a$ ( $m/s^2$ )	7.87	3.148
Drag Coefficient, $C_d$	0.28	0.28
Frontal Area, $A_f$ ( $m^2$ )	2.15	0.344
Friction coefficient on asphalt [13] – $\mu$	0.017	0.017
Wheel radius, $r$ (m)	0.352	0.1408
Air Density, $\rho$ ( $kg/m^3$ ) [14]	1.225	1.225
Gravitational acceleration, $g$ ( $m/s^2$ )	9.81	9.81
Wind Velocity, $V_w$ (m/s)	5	2
Inclination, $\theta$ (deg)	0	0
Gearbox Ratio, $g$	1:3	
Scaling Factor, $x$	2.5	

entire drive cycle are shown in Figure 3.5.

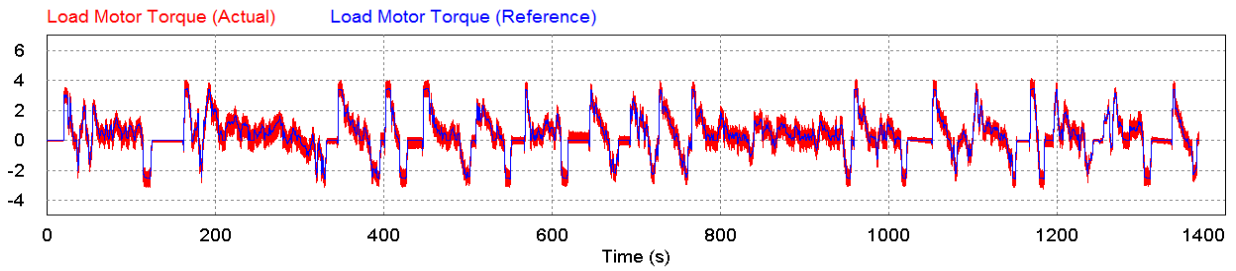
In Figure 3.5, the simulated results of the UDDS drive cycle are shown. Figure 3.5(a) shows the AC currents in the traction motor. The points where the motor currents are constant indicates the motor has stopped rotating and is maintaining its magnetic field flux. The only task of the traction motor control loop is to track the reference speed which is shown in Figure 3.5(b). The load motor torque reference and tracked torque are shown in Figure 3.5(c) where the control loop’s only purpose is to track the torque requirements of the load motor. Based on the combination of speed output provided by the traction motor and the torque output provided by the load motor, the traction motor has to provide a set torque according to the scaling equations. There is no reference for the traction motor torque and the output is strictly from the control of the traction motor torque and the load motor torque. The result is shown in Figure 3.5(d). Finally, Figure 3.5(e) shows the traction motor mechanical power. This is just a multiplication of the angular speed with the torque for easier viewing. However, it can be easily compared to the conservation of energy results which shows the simulation of the system in PSIM follows the scaling results shown in MATLAB.



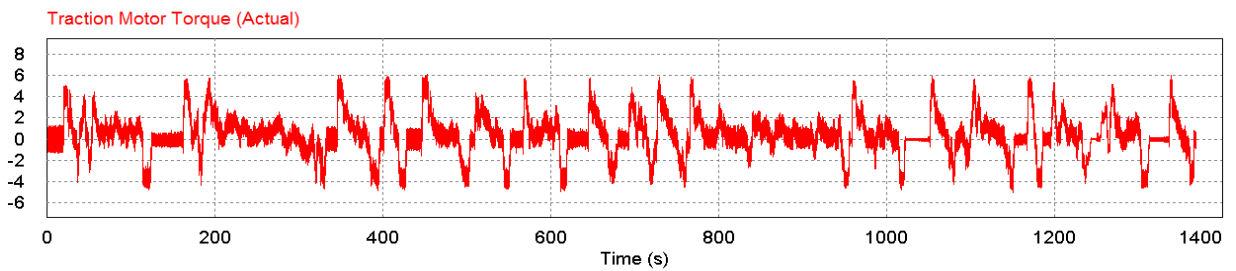
(a) Traction Motor AC Currents in A



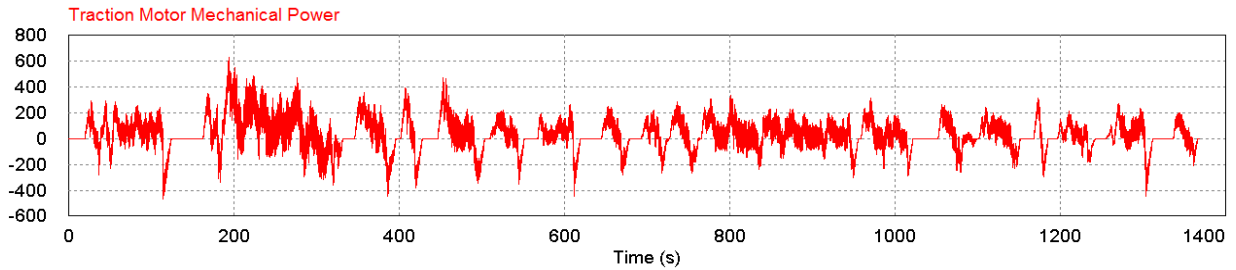
(b) Traction Motor Speed Reference and Tracked Speed in RPM



(c) Load Motor Torque Reference and Tracked Torque in Nm



(d) Traction Motor Torque in Nm



(e) Traction Motor Mechanical Power in W

Figure 3.5: Test Bed Simulation Results of Scaled Vehicle

These results presented in Figure 3.5 have been obtained based on a scaling factor of 2.5 and a virtual gearbox with a ratio of 1:3, as shown in Table 3.1. The gearbox employs a speed reduction and a torque increase to move the operating point of the machine to a more midpoint area for larger torque variations during the drive cycle so that more resolution can be obtained, and any errors can be seen more clearly.

Examining the two torque graphs, in Figures 3.5(c) and 3.5(d), shows that there is some noise associated with the results indicated by the thicker lines. There are many sources for this, one being the time stamp interval of the simulation program. Due to the lengthy simulation time and large simulation file, the largest allowable computation step size was chosen and only one point in every two hundred calculations was recorded. The large step size may create oscillations between calculated results about the ideal operating point. The points recorded may also exaggerate this issue depending on when the data is recorded. Another source of error could be from the control loop of the motors. The motors require a constant flux to maintain a constant magnetic field. Any disturbances in this field will create torque ripples that could be seen on the motor shafts as there is not much inertia to prevent this oscillation from occurring. A third source of error could be a natural torque oscillation from the two motors being coupled together where the torque ripple is transferred back and forth between machines. However, this ripple is relatively small and by inserting a 'gearbox' into the calculations along with the scaling, the amount of noise is reduced every time the gear ratio is decreased, causing a torque increase. An acceptable ratio was used where the signal could easily be extracted and one where the actual hardware in the test lab could run without issues.

# Chapter 4

## Hardware-in-the-Loop Test Bed Design

### 4.1 System Layout

The system was designed around modularity with each individual section being able to be taken out or replaced if desired. The block diagram of the system is shown in Figure 4.1. The following four main electrical modules make up this system:

- AC/DC converter
- DC/DC converter
- DC/AC Speed or Traction Motor Controller
- DC/AC Torque or Load Motor Controller

The mechanical connection between the DC/AC Speed and DC/AC Torque blocks is comprised of two motors, motor cradle, motor shafts, and a mechanical coupling. In Figure 4.1, the source block represents a connection point to an external AC power source, such as AC grid.

### 4.2 Source

The power source for the test bed is a 208V, 40A, 60Hz, 3-phase, 4-wire electrical connection to the University of Waterloo Centre for Environmental & Information Technology

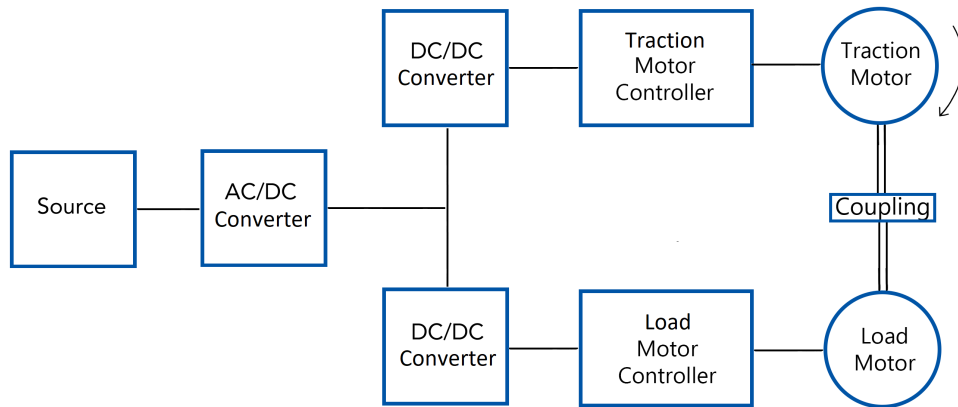


Figure 4.1: Test Bed Setup

distribution system. The plug used to connect to the receptacle was a Hubbell CS8365C. The four wires are connected to a 3-pole, 30A breaker mounted on the test bed serving as a close proximity power shut off switch. The breaker is complimented by Ametherm AS32 5R020 inrush current limiters, one on each phase. The inrush current limiters are rated at 20A and are connected to a 6kVA delta-wye Fortress Series transformer by Hammond Power Solutions Inc., whose secondary is connected to the test bed system.

The inrush current limiters were selected based on the cold on-resistance specification of at least  $5\text{ohms}$ , and a low hot on-resistance specification of less than  $0.025\text{ohm}$ , resulting in a low voltage drop of  $0.5V$  at maximum rated continuous current. The 20A continuous current limit of the device does not limit the maximum power of the system which is dictated by the 6kVA transformer. Overloading of the transformer to some extent is possible but not for a considerable length of time. However, for future expansion of the system in the event the current limiters are required to dissipate more than  $600J$  of energy, a larger inrush current limiter, i.e., Ametherm AS35 5R025, capable of dissipating  $1.2kJ$  of energy is available as a drop in replacement having the same hot and cold on-resistances.

The transformer delta-wye configuration was chosen to trap the third harmonic components in the delta winding. In addition, this transformer provides additional protection by isolating the grid from the converter and the rest of the system, and has taps on the primary side for 95%, 100%, and 105% winding ratios. This provides a little more fine-tuning flexibility for the converter in the event the primary side voltage is too high or too low for the converter operation.

One main disadvantage of introducing the transformer into the system is associated with size, weight, and cost. The other disadvantage of adding the transformer is additional

conduction and core losses. The conduction losses are an ohmic function solely dependent on the resistance of the enamel windings and the current required by the system. The core losses are due to the alternating flux and are comprised of eddy current and hysteresis losses. In addition, the selection of a  $6kVA$  transformer over one with a higher rating was done based on the current needs and power requirements of the current test bed with some power overhead margin. Due to the topology layout with back-to-back motors connected together, once the motors are turning at constant velocity, the power is circulated internally, with the external source providing only the energy losses. This topology limits losses further and prevents the unnecessary addition of larger components, as one machine acts as a motor and the other a generator, at any given moment in time. A  $9kVA$  version of the same transformer family exists if the need to upgrade arises in the future. The secondary side of the transformer is connected to the input terminals of the AC/DC module.

## 4.3 AC/DC Converter

### 4.3.1 Background

The core design of the AC/DC firmware was created by a graduate student from the University of Waterloo and can be referenced in his MASc thesis [25]. The firmware was coded for a Texas Instruments Delfino TMS320F28335 microcontroller. A brief overview will be conducted on the parts that are relevant to the test bed and the parts that were designed and implemented independently.

A schematic of the AC/DC converter and its control is shown in Figure 4.2. The IGBT module, controller design, sensors, and reactive components are shown in Figure 4.2(a) while the logic that controls the converter is shown in Figure 4.2(b). The soft-start circuit is introduced later in this chapter.

The AC/DC converter is required to create a DC rail for the rest of the system to use. To maintain the power rating of the system, the AC/DC converter was designed with the ability to pull up to  $6kVA$  of power from the grid. An active converter with bidirectional capability is used, with the ability to pull or inject current from/to the grid. The IGBT module used, Powerex PM50CL1A120, consists of six transistors, two in each leg, rated at  $1200V$  and  $50A$ . In anti-parallel with each IGBT switch, there is a body diode between the collector and emitter.

When power is applied to the converter, it behaves as a three-phase diode bridge rectifier allowing the voltage to rise to a maximum of  $280.8V$  on the DC terminals, according to



### 4.3.2 Current and Voltage Sensors

For both AC and DC voltage measurements, LEM LV-20P closed-loop, Hall Effect transducer was used.

On the AC side, only a single sensor was placed on one of the phases to measure the voltage. It was assumed that the AC supply was balanced and the voltages on the other two lines would be of the same magnitude and phase shifted by  $\pm 120$  degrees. A single-phase sensor is adequate for phase locked loop (PLL) synchronization. To maintain an accurate voltage reference, the primary side of the transformer was used for PLL synchronization. As the transformer is delta on the primary and wye on the secondary, a phase shift of 30 degrees is added to the PLL to compensate for phase shift caused by the transformer. The voltage sensor is designed for a peak phase voltage of  $200V$ ,  $140V_{rms}$ . A margin of safety was left from the nominal phase voltage of  $120V$  and the remainder of the measurement range took advantage of the entire ADC range for resolution and accuracy.

The AC current measurements were done using LEM LA55-P transducer. The current sensors on the AC side are required to control the active and reactive power of the system and are placed on all three phases [26]. The current control runs on an inner control loop scheme while the outer loop controls the DC side voltage.

On the DC side, the voltage sensor was placed immediately at the DC output terminals of the IGBT module, but before the soft-start and system protection switches, to sense the voltage on the capacitor bank when the protection switches are closed, and to detect faults in the system when these switches are open. The DC-side voltage sensor was designed for a peak voltage of  $550V$ . The system was initially planned to be operated at a voltage of  $450V$  for lower ohmic losses but due to the voltage requirement of the motors, discussed further in this chapter, the output voltage was lowered to  $350V$ . No current measurements were done on the DC side at this stage, as they are measured in the next stage.

The schematics and equations for measuring the AC and DC voltages and currents can be seen in Figure C.1 and Figure C.2 in Appendix C.1. The component bill of materials (BOM) used for the AC and DC sensors are shown in Table C.1, C.2, and Table C.3 in Appendix C.2.

### 4.3.3 Filter Design

An inductor on the AC side of the AC/DC converter is required to boost the voltage above the diode rectification voltage and buck the voltage down into the grid, when operating in bidirectional mode. Based on the AC/DC module design power limit of  $6kVA$ , the



maximum current on the AC side is  $16.67A_{rms}$ . To reduce the current ripple passing through the electronics, the main inductor was sized to provide less than 30% peak-to-peak ripple of the rated current at the operating switching frequency. This specification was chosen in the interest of generating less electromagnetic interference on all low-voltage lines and to obtain cleaner current measurements for the microcontroller. In addition, this inductance lowers the Total Harmonic Distortion (THD) of line currents when injecting power into the grid. The relationship between the AC-side inductance and current ripple in a 6-switch VSI is given by (4.2) [27].

$$L = \frac{V_{dc}T_s}{2\sqrt{3}I_{pp,ripple}^{max}}m \quad (4.2)$$

In (4.2),  $L$  is the inductance in  $H$ ,  $V_{dc}$  DC voltage in  $V$ ,  $T_s$  switching time period in seconds,  $I_{pp,ripple}^{max}$  max peak-to-peak current ripple in  $A$ , and  $m$  modulation index. For the design specifications,  $V_{dc}$  is  $350V$ ,  $T_s$   $1/20kHz$ ,  $I_{pp,ripple}^{max}$   $5.0A$ , and  $m$  unity. This provides a design inductance equal to or greater than  $1.01mH$ . The core of the inductor was chosen based on meeting the specifications and the availability of the desired material. The core chosen was Micrometals Inc. FS-250026-2.

The final inductor designed has an inductance of  $1.22mH$  when measured under no load. This is very close to the theoretical value of  $1.21mH$  estimated at no load. At full load of  $16.67A$ , the theoretical inductance drops to  $1.10mH$ . Since there is no saturation starting to occur, a linear interpolation can be done to estimate that the final constructed core will have an inductance of  $1.12mH$  under full load. The resultant current ripple is  $4.51A_{pk}$  or 27.1% of max current. This meets the design criteria and is acceptable for the design. The design uses two ferrite cores stacked on top of each other with a single 11 AWG winding. At maximum load, the total losses will be  $14.63W$ , with a temperature rise of 45 degrees Celsius. The entire calculation can be seen in Appendix A.1.

To reduce the DC voltage ripple harmonics, capacitance must be added. A design requirement to keep the peak to peak voltage ripple at or below 0.5% was set indicating the voltage must have a ripple component less than  $1.75V_{pp}$ . The voltage ripple is entirely dependent on the load current and can be calculated through (4.3) [28].

$$C = \frac{I_{out} \times T_s}{8 \times V_{pp,ripple}^{max}} \quad (4.3)$$

In (4.3),  $C$  is the capacitance in  $F$ ,  $I_{out}$  average DC current in  $A$ ,  $T_s$  switching time period in seconds,  $V_{pp,ripple}^{max}$  max peak-to-peak voltage ripple in  $V$ , and  $m$  modulation index.

For the design specification,  $I_{out}$  is 20A,  $T_s$  1/20kHz, and  $V_{pp,ripple}^{max}$  1.75V. A capacitance value of at least  $71.4\mu F$  satisfies this voltage ripple requirement. However, this is for an ideal case where no stray resistance or inductance effects are present in the system. To ensure there is at least a  $-40dB$  noise attenuation at the  $20kHz$  switching frequency, the, capacitance was increased to  $750\mu F$ . Five Kemet C4DEHPQ6150A8TK film capacitors, each with a capacitance of  $150\mu F$  were connected in parallel. With the inductor designed in Appendix A.1, the  $-3dB$  point for the low pass filter is located at  $166Hz$ , which satisfies the switching frequency attenuation requirement.

#### 4.3.4 Design of Soft-Start Circuit with Normal and Emergency Shutdowns

The soft start circuit with normal and emergency shutdowns is shown in Figure 4.3. The soft start circuit was designed to slowly charge the capacitance on the high-side DC bus and be able to discharge all the energy in the system in standard shutdown and emergency shutdown conditions. Having two motors connected back-to-back can be also be used as a load on the system to help discharge energy. This is due to a circulating current that can form where one machine will be a motor, and the other a generator, with energy circulating in the DC bus. As this is an induction machine, maintaining a field flux will also discharge the capacitors in parallel with the shut down circuit.

To design the shutdown circuitry, the case where all the energy in the system must be discharged by the resistors was considered. In this scenario, the power converters connected to the motors open all switches and the motors' fluxes collapse. There are three main DC buses in the system. The first one is created by the AC/DC converter and will be referred to as the high-side DC bus. The two DC/DC converters step down the high-side DC bus voltage, and create two DC buses which will be referred to as the low-side DC buses. The voltage of the high-side DC bus,  $V_{high}$ , is 350V and has a capacitance of  $750\mu F$ . The voltage of the two low-side DC buses,  $V_{low}$ , are set at 100V and each of them has a  $1mF$  capacitor connected. It is imperative to find out how long it takes for the system to discharge in an emergency condition to create a specification for the maximum resistance that can be used. A design criteria of 0.5 seconds was set to define the maximum time that it can take for the system to discharge down to a safe voltage level,  $V_{safe}$ , of 5V in an emergency condition. This was calculated using (4.4) with the derivation shown in Appendix F.1.

$$R_{FastDischarge,max} = \frac{T_{max}}{(-C_1 \ln(\frac{V_{low}}{V_{high}}) - C_2 \ln(\frac{V_{safe}}{V_{low}}))} \quad (4.4)$$

In (4.4),  $R_{FastDischarge,max}$  is the maximum resistance,  $T_{max}$  design time criterion,  $C_1$  high side capacitance of  $750\mu F$ ,  $C_2$  low and high side capacitance of  $2.750mF$ ,  $V_{high}$  high side voltage of  $350V$ ,  $V_{low}$  low side voltage of  $100V$ , and  $V_{safe}$  safe system voltage of  $5V$ .

A maximum resistance of  $54.48ohm$  was obtained from the calculation. The final design resistance was chosen to be  $33ohm$  with a power rating of  $250W_{continuous}$ ,  $6250W_{peak}$  one second pulse power to discharge the voltage to the safe level within  $0.3$  seconds.

The soft start circuit used to charge the capacitors can also discharge the circuit in a normal condition. The time to discharge the entire system was set to  $10s$ , leading to a maximum resistance of  $1,090ohm$ . A resistor of  $680ohm$  was chosen with a power rating of  $180W$ ,  $4500W$  peak one second pulse power to discharge the voltage to a safe level within  $6.24s$ .

The soft-start circuit of Figure 4.3, shows the arrangement of the four IGBTs. The  $680ohm$  resistor is used in both the soft-start resistor and a normal shutdown procedure. The IGBTs are IXYS IXGR24N120C3D1 rated for  $1200V$  and  $48A$ . These are high-side transistors and require isolation from the control board. Signals from the microcontroller are passed through a buffer and an LED optical driver, Broadcom HFBR-1512Z, shown in Figure 4.4(a). The signal travels through a fiber optic cable to a photodiode receiver, Broadcom HFBR-2521Z, which passes the signal to an optically isolated gate driver, Broadcom ACNW3130-000E. Individual isolated DC power supplies,  $+16V/-8V$ , are created for each signal from a Powerex VLA106-15242 module. The entire receiver module is shown in Figure 4.4(b). The BOM for both items is shown in Appendix G.1 for the transmitter and Appendix G.2 for the receiver.

### 4.3.5 Complete AC/DC module

The complete AC/DC module can be seen in Figure 4.5. In Figure 4.5(a), the IGBT module, soft-start circuit, controller, inductors, sensors and fiber optic transmitter and receiver are labeled. The capacitors are shown in Figure 4.5(b).

## 4.4 DC/DC Converter

### 4.4.1 Topology

There were three main requirements for the design of the DC/DC converter. They were:

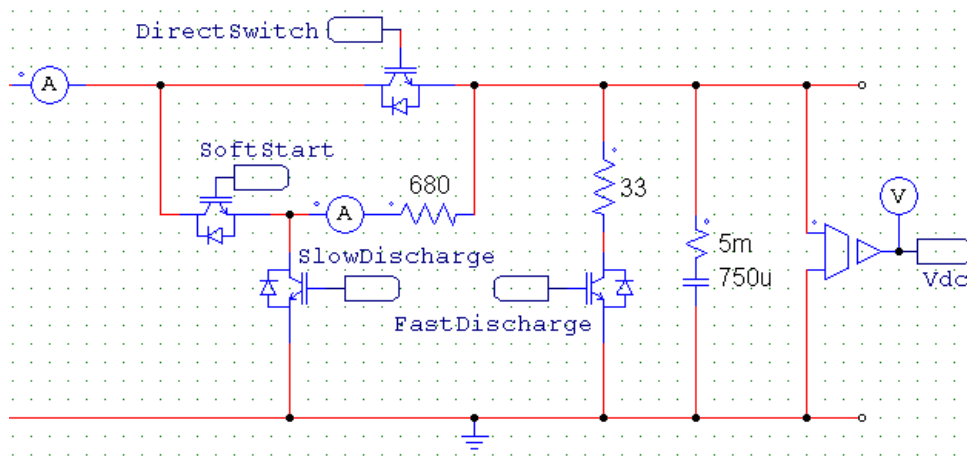


Figure 4.3: AC/DC Soft-Start with Normal and Emergency Shutdowns

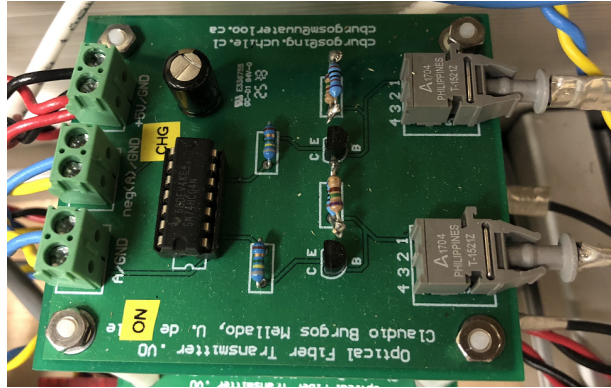
- Step the voltage down to a level with minimal overhead for the AC motors
- Enable bidirectional power flow
- Keep the topology as simple as possible

The topology that satisfies all these requirements is the bidirectional buck-boost converter. The output involves an inductor and capacitor, inherently creating a low pass filter by the design. The schematic of the DC/DC converter topology is shown in Figure 4.6. In the test bed system, there are two of these converters providing an individual power source to each motor from the same high-voltage bus.

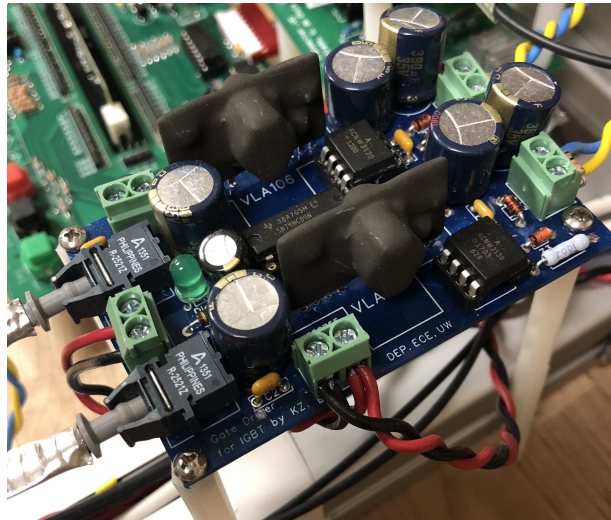
The induction motors are rated for a voltage of  $49.7V_{rms}$ , which is realized by DC/AC converters operating under SVPWM. The minimum DC voltage that will allow the motor voltage to reach this value is  $70.3V$ . To compensate for losses, a low-side DC voltage of  $100V$  was chosen to obtain the motors' rated voltage and have some overhead margin for losses, and proper PWM operation.

#### 4.4.2 Duty Cycle Limits

Under standard operating conditions, the converter behaves like a buck converter. The duty cycle is 28.6%, as given by (4.5), negating any inefficiencies. The duty cycle is relatively low but can change very quickly by the inner current control loop. Once the efficiency factor is incorporated, the duty cycle will increase to compensate for the losses.



(a) Fiber Optic Transmitter

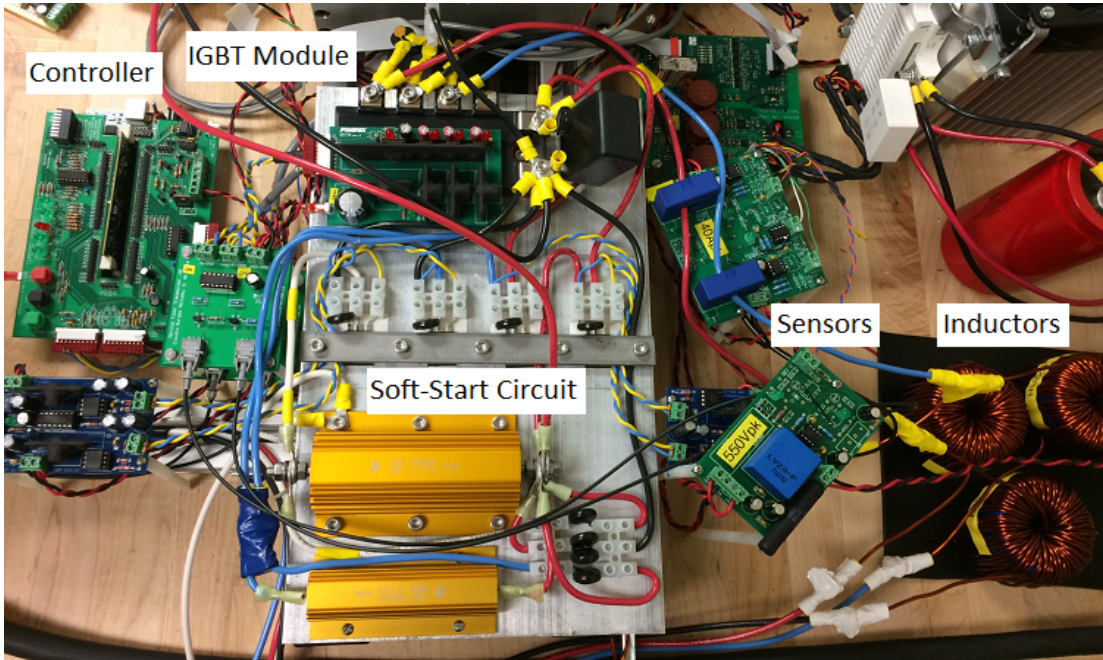


(b) Fiber Optic Receiver

Figure 4.4: Fiber Optic Transmitter and Receiver

$$D = \frac{V_L}{V_H} = \frac{100V}{350V} = 0.286 \quad (4.5)$$

As there are two transistors in one leg, both cannot be turned on simultaneously, as a short circuit across a voltage source would otherwise result. In addition, a duty cycle of 100% cannot be achieved on this converter when operating in bidirectional mode. When the voltage on the low-side DC bus begins to rise, the controller will operate as a buck converter and reduce the duty cycle to allow less current in from the high-side voltage



(a) AC/DC Module Components



(b) AC/DC Module Output Capacitors

Figure 4.5: AC/DC Module of Test Bed

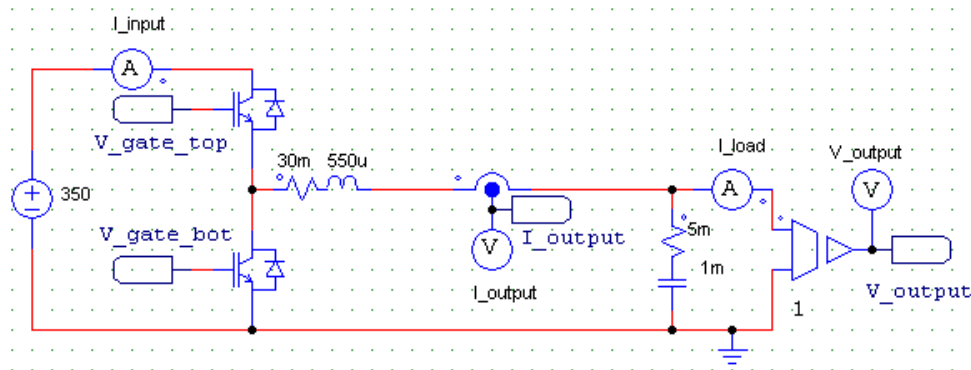


Figure 4.6: Bidirectional Buck-Boost Converter Schematic

rail. With no limitations, the control loop will automatically try to turn on the bottom transistor continuously which would result in a short circuit of the low-voltage DC side to ground. To allow current to be injected back into the high-voltage rail, the inductor is required to charge and effectively limit the duty cycle of the bottom transistor so that it turns off and allow the system to operate as a boost converter.

The case where the top transistor is on 100% of the time is also a problem only when starting up. The controller would want to turn the top transistor on completely, effectively creating a short between the high-side voltage rail into the capacitor through the inductor, resulting in a large transient current. To mitigate this issue, the duty cycle limits are carefully controlled during start up conditions until the desired voltage is achieved, and then set to their normal operating values.

Therefore, for reliability and proper operation, the duty cycle is limited to always be greater than 10% and less than 90%.

### 4.4.3 Controller Design

The controller was designed based on both voltage and current feedback loops for control. The current controller is on the inner loop and responds very quickly to changes in the current. The voltage controller is on the outer loop and responds to changes more slowly compared to the current controller. This provides a robust control as the maximum current flowing through the electronics can be limited through firmware and allows for over-current and over-voltage detection with a relatively quick response. Both the inner current and outer voltage loops are implemented using PI controllers. The main control loop code for

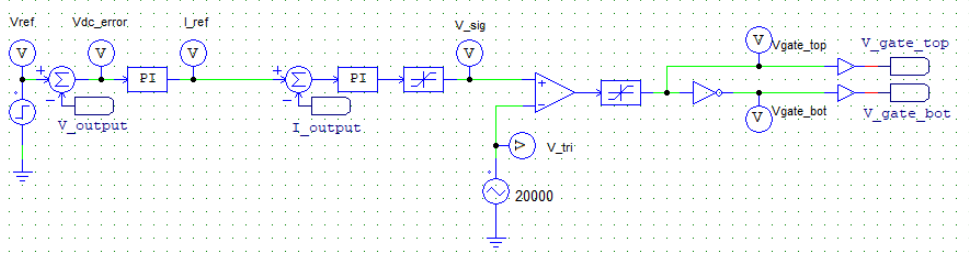


Figure 4.7: Bidirectional Buck-Boost Converter Logic

the DC/DC converter is given in Appendix B.2. The main control loop logic is shown in Figure 4.7.

#### 4.4.4 Current and Voltage Sensors

The sensor design is based on the isolated topology to maintain the safety of the system at the same level as in the case of the AC/DC converter. The voltage is measured using the LEM LV-20P sensor and the current is measured using the LEM LA 150-P sensor. The voltage measurement range was set between 0V to +150V and the current limit was set to  $\pm 100A_{pk}$ . The voltage sensor has some margin left in the event the low-side DC voltage is raised without any hardware modification. The current sensor also has some sensing margin to allow for higher currents in the DC link if the DC bus reference voltage is lowered to be closer to the minimum DC voltage required by SVPWM to meet the full operating range of the motor.

The schematics and equations for measuring the DC voltage and current can be seen in Figure C.2 in Appendix C.1. The component BOM used for the DC sensors are shown in Table C.4 and C.5 in Appendix C.3.

#### 4.4.5 Filter Design

The low pass LC filter was designed to limit the high frequency ripples of the voltage and current. The inductor can be designed based on the current ripple specification and other parameters using (4.6) [29].

$$L = \frac{(V_{in(max)} - V_{out}) \times D}{f_s \times \Delta I_L} \quad (4.6)$$



In (4.6),  $V_{in(max)}$  is the maximum voltage on the high voltage side,  $V_{out}$  voltage on the low-side,  $D$  duty cycle,  $f_s$  switching frequency,  $L$  inductance, and  $\Delta I_L$  peak-to-peak current ripple. The system inductance can be designed having a high-side voltage of  $350V$ , low-side voltage of  $100V$ , duty cycle of  $0.286$ , switching frequency of  $20kHz$ , and the design specification for a current ripple of  $15\%$ . For a  $6kVA$  system power flow at  $100V$ , the current is  $60A$ , with a  $9A_{pk-pk}$  current ripple. This leads to a minimum inductance requirement of  $397\mu H$ .

The final inductor designed has an inductance of  $560\mu H$  when measured under no load. This is very close to the theoretical estimate of  $566\mu H$  estimated at no load. At full load of  $60A$ , the theoretical inductance drops to  $435\mu H$  as the core begins to saturate. The resultant current ripple is  $8.21A_{pk-pk}$  or  $13.7\%$  of max current. This meets the design requirement and can be used even though the core is starting to saturate at max current. The design uses three ferrite cores stacked on top of one another with dual 11 AWG windings in parallel to take advantage of mutual inductance and reduce ohmic losses. At maximum load, the total losses will be  $67.87W$ , with a temperature rise of  $91$  degrees Celsius. The entire calculation can be seen in Appendix A.2.

The voltage ripple is a function of the current ripple which was designed to be  $8.21A_{pk-pk}$  in the inductor calculation. A design criterion of less than  $0.1\%$  voltage ripple was set and (4.7) can be used to find capacitance based on voltage ripple [29].

$$C = \frac{\Delta I_L}{8 \times f_s \times \Delta V_o} \quad (4.7)$$

In 4.7,  $C$  is the capacitance,  $\Delta I_L$  current ripple,  $f_s$  switching frequency, and  $\Delta V_o$  output voltage peak-to-peak ripple. The resultant minimum capacitance that meets the voltage ripple specification is  $513\mu F$ . An aluminum electrolytic capacitor with a capacitance of  $1mF$  was chosen based on standard availability.

#### 4.4.6 System Hardware

The firmware for both DC/DC converters is realized by one Texas Instruments Delfino TMS320F28335 microcontroller. The daughter board used in the hardware setup is the same as the one used in the AC/DC module except with some hardware changes for the low pass filter inputs, and the addition of a second thermistor. The outputs of the PWM stage go to a fibre optic transmitter, Broadcom HFBR-1521Z, and are received by a Broadcom HFBR-2521Z. A fibre optic connection was used for this module due to the DC/DC power

stage being quite far away, to minimize voltage drop, increase noise immunity from the AC/DC power switching stage, and provide additional isolation between the control board and the high-voltage rails. The received signals enter the driver, Broadcom ACNW3130-000E, which produces the voltage going to the gate of the IGBT. The voltages going to the gate of the IGBT are created by the Powerex VLA106-15242. It uses the same low-voltage power supplies used elsewhere in the system to make voltages of  $+15V$  and  $-8V$  on the board. The IGBT switches, Powerex CM100DY-12H, are based on a two switch per leg configuration capable of withstanding  $600V$  and  $100A$ . A thermistor from Murata NXFT15XH103FA2B025, is attached to each module for temperature management. Both transistors are mounted on an aluminum heatsink with one fan. The entire module can easily be disconnected through a connection strip to allow access to the hardware underneath or change it all together.

The DC/DC modules have been designed for  $6kW$  of power transfer. However, as there are two independent converters, the total power going through both converters cannot exceed  $6kW$ . Each converter can handle the full  $6kW$  load and has been designed to do so.

#### 4.4.7 Complete DC/DC module

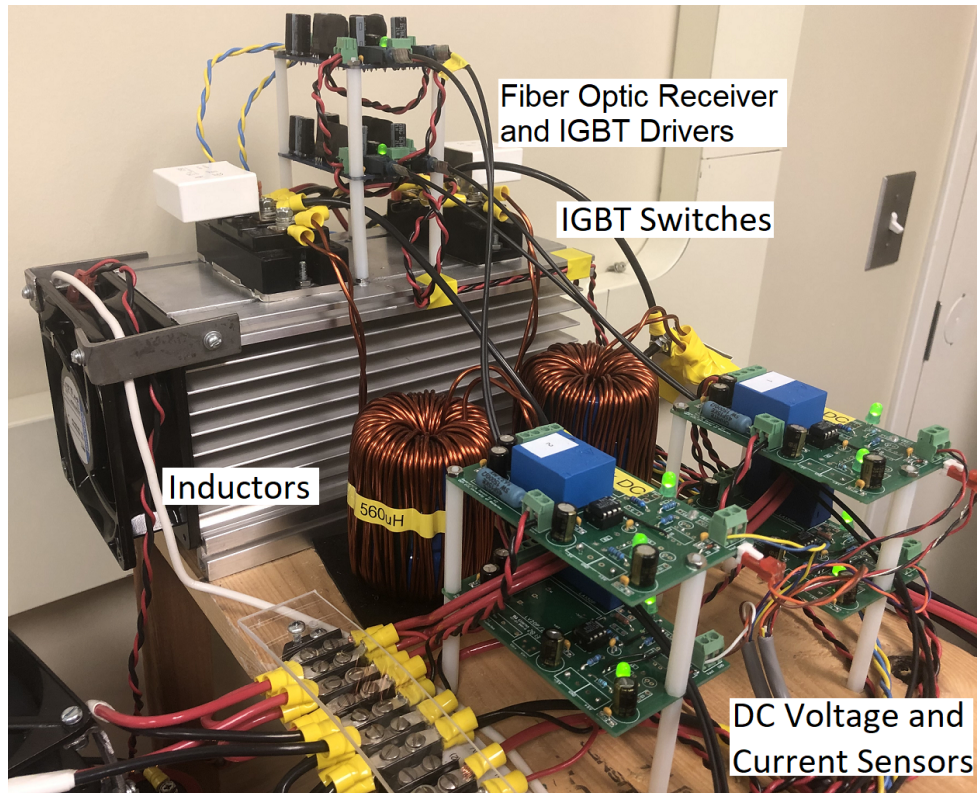
The complete DC/DC module can be seen in Figure 4.8. All components of the system are shown in Figure 4.8(a) and the controller is shown in 4.8(b). The only components not seen are the DC side bulk capacitors which are seen in the DC/AC Module images.

## 4.5 DC/AC Design

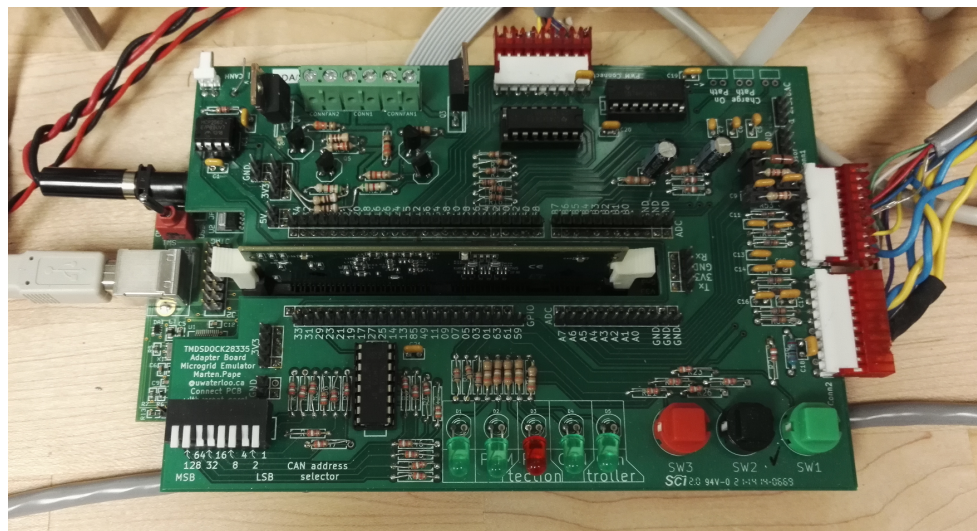
### 4.5.1 Topology

The motors are the fundamental components of the hardware in the loop test bed. The motors were chosen based on performance capability and being readily available. The motor selection criteria was as follows:

- Size: The size of the motor could not be too large to fit in a lab bench setup. The weight is roughly proportional to the size and the motor could not be too heavy to be placed on the test bed bench.
- Performance: The motor must be able to run a full drive cycle meeting torque, speed, and acceleration requirements.



(a) DC/DC Module Power Electronics, Sensors, and Drivers



(b) DC/DC Module Controller

Figure 4.8: DC/DC Module of Test Bed

- Price: The price of the motor must be reasonable for a test lab setup while providing adequate specifications that are attainable in a lab environment.

These three requirements set the criteria for the ideal motor in the HIL setup. The Advanced Motors and Drives ACX-2043 induction machine, was selected to meet all these requirements. The motor specifications are listed in in Table 4.1. The drawback of this motor is that it is a low voltage, high current device, resulting in a relatively low top speed due to back EMF and a high torque capability for a test bed. Due to the way the scaling approach works, both of these issues are easily resolved.

Table 4.1: Advanced Motors and Drives ACX-2043 Induction Motor Specifications

Motor Nameplate Ratings	
Power	5.69kW
RPM	4021rpm
Voltage	49.7V
Current	101.1A
Frequency	137.1Hz
Poles	4
Phase	3
Motor Internal Parameters	
Stator Resistance $R_s$	4.870m $\Omega$
Stator Leakage Inductance $L_{ls}$	25.20 $\mu$ H
Magnetizing Inductance $L_m$	1.055mH
Rotor Leakage Inductance $L_{lr}$	22.00 $\mu$ H
Rotor Resistance $R_r$	6.670m $\Omega$

Two of these motors were selected for the test bed. As they are the same motors, they can be easily connected together due to both having rotor shafts at the same height, allowing for easy coupling. The motor was provided with one side of the rotor being attached to the back wall of the motor through a bearing mount while the mating side of the motor was left open and a motor cradle was required to be designed to support the rotor.

The schematics of the speed and torque motor module are shown in Figure 4.9 and Figure 4.10 respectively. For the speed motor, the power section is shown in Figure 4.9(a),

the control logic in Figure 4.9(b), and the flux and torque estimators in Figure 4.9(c). For the torque motor, the power section is shown in Figure 4.10(a), the control logic in Figure 4.10(b), and the flux and torque estimators in Figure 4.10(c).

## 4.5.2 Controller and Hardware

Each motor is controlled by a Texas Instruments Delfino TMS320F28335 which runs the entire field-oriented control (FOC) algorithm. The hardware also runs the PWM, ADC, I2C, UART, and QEP hardware blocks. The IGBT module used is an Infineon IFS150V12PT4 capable of handling up to  $150A_{rms}$  and  $850V_{dc}$ , with a switching frequency of  $20kHz$ . The drivers used are on an Infineon MA040E12 Evaluation board. The PCB makes four isolated power supplies where one power supply is capable of driving the bottom three transistors of each leg with high current, while the other three have lower current driving capability for the three top transistors. The QEP block is used to measure the speed of the motors. The I2C controller is used for communications between the modules, and the UART is used to send data one way to the computer.

## 4.5.3 Motor Cradle and Shaft

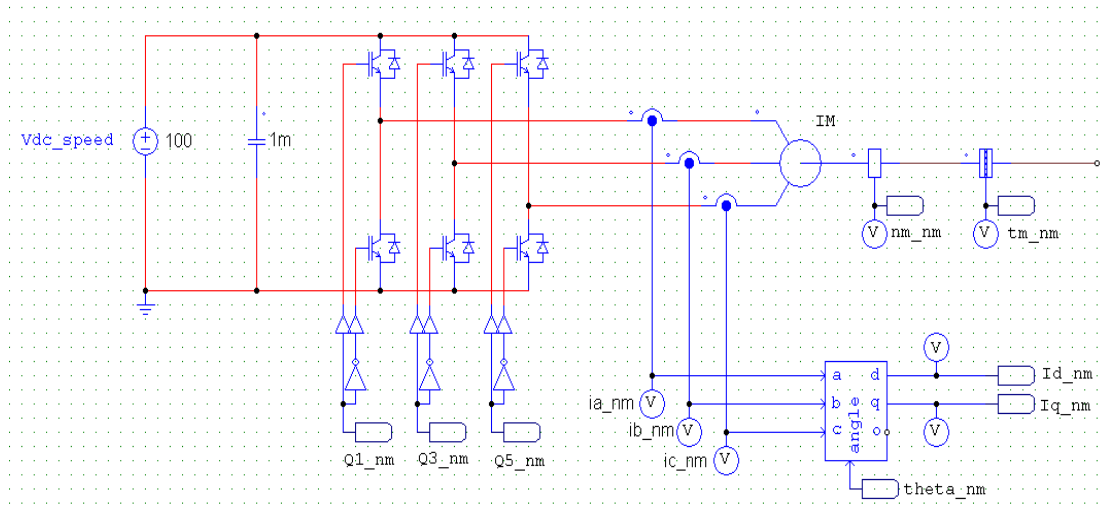
### 4.5.3.1 Motor Cradle

A motor cradle was designed to with the following requirements:

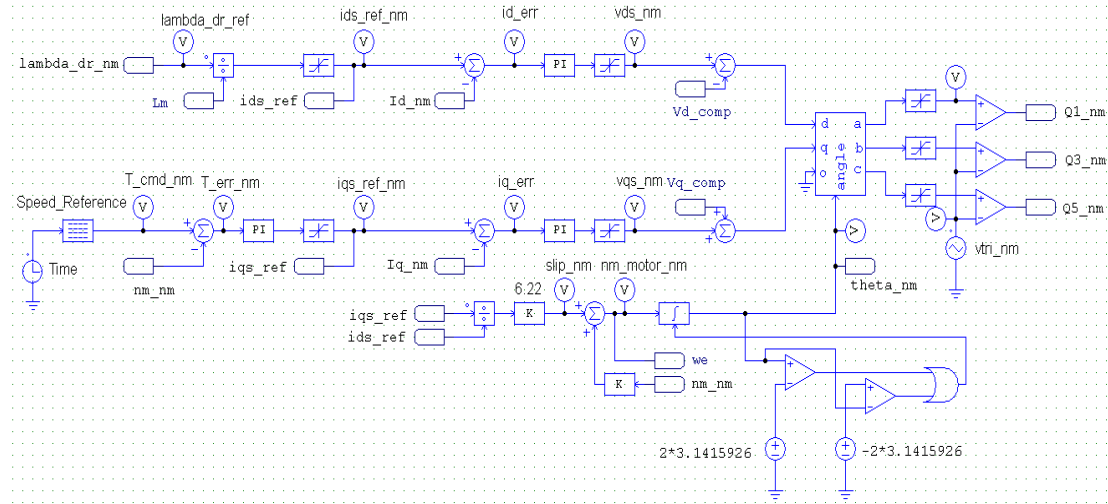
- Support the open end of the rotor.
- Allow the motor to be moved easily for system expansion, alignment, and maintenance.
- Permit the support of a rotational load, if required.
- Keep the cost low for a lab test bed setup.

The design of the final motor cradle is shown in Figure 4.11. It is comprised of five unique parts being the back plate, front plate, three identical brackets connecting the front and back plates, one unique bracket to avoid motor case protrusions and connect the front and back plates, and a coupling to connect the rotor shaft with the front plate.

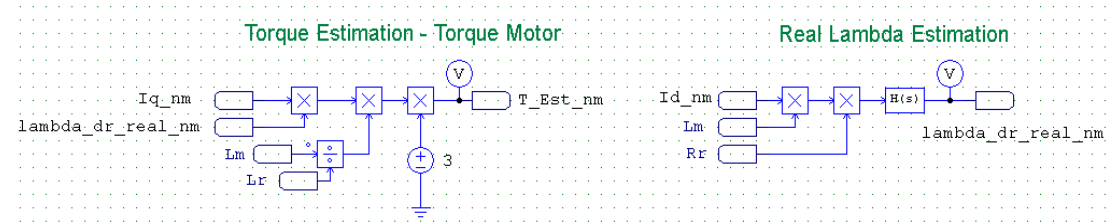
The entire motor with its cradle is connected to t-slot extrusions. End-feed fasteners sit in the grooves of the aluminum extrusions which are connected to the motor cradle with screws through holes in the brackets. The t-slot extrusions are bolted to the table in various places to prevent movement.



(a) DC/AC Speed Module Power Section

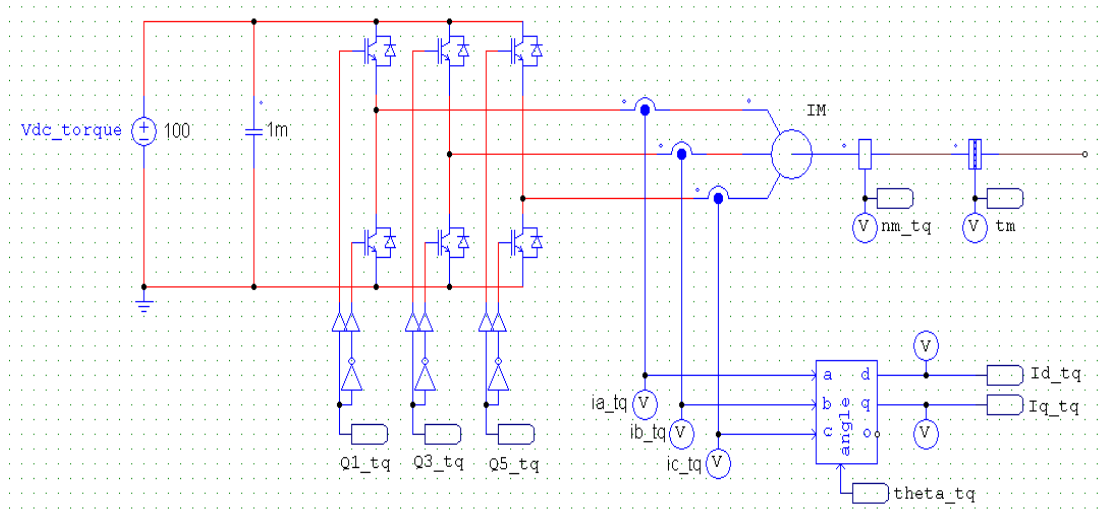


(b) DC/AC Speed Module Control Logic Section

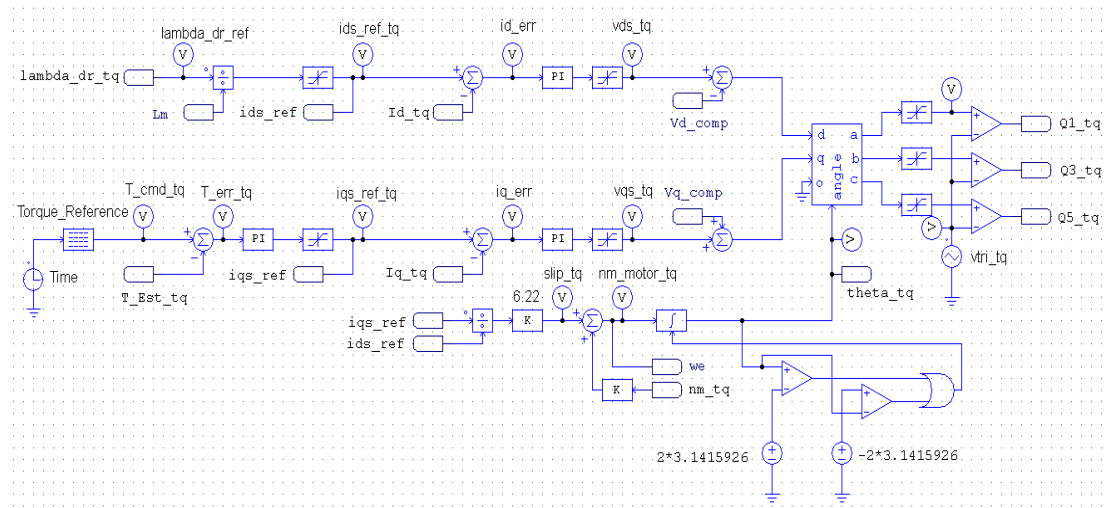


(c) DC/AC Speed Module Estimators Section

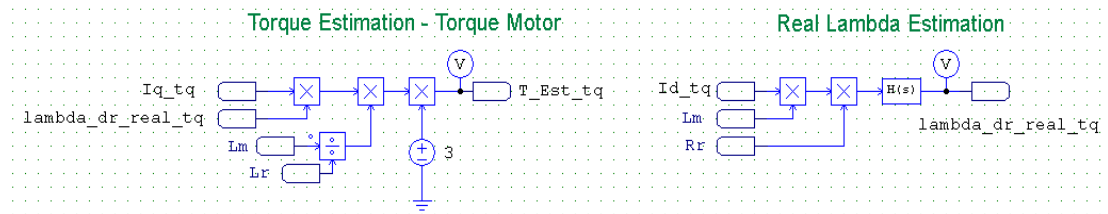
Figure 4.9: DC/AC Speed Module of Test Bed



(a) DC/AC Torque Module Power Section



(b) DC/AC Torque Module Control Logic Section



(c) DC/AC Torque Module Estimators Section

Figure 4.10: DC/AC Torque Module of Test Bed

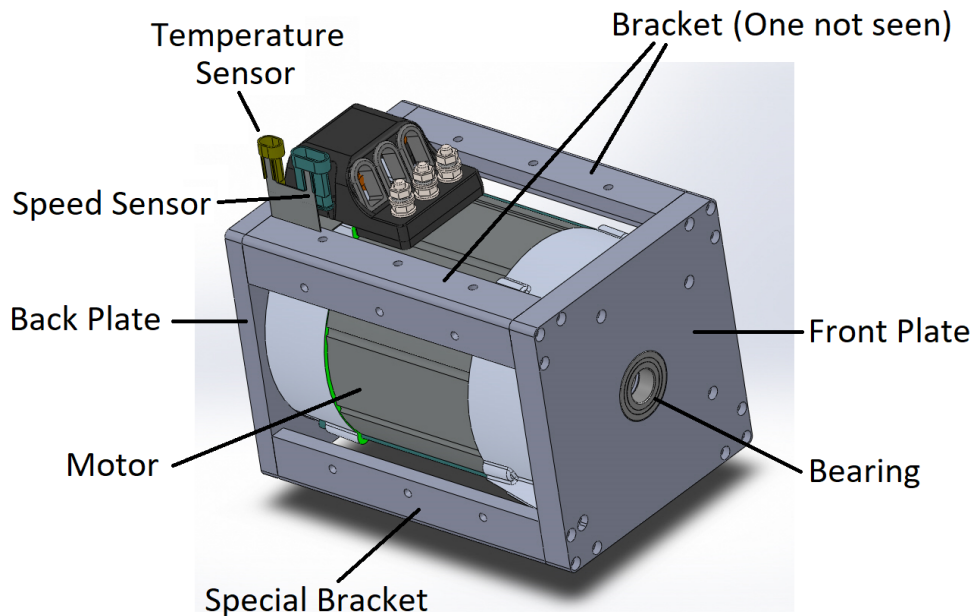


Figure 4.11: Motor with Cradle

To ensure the rotor is centered with respect to the stator, a coupling is press fit onto the rotor shaft. A bearing is then fitted using an interference fit onto the coupling. A bearing is then press fitted into the inside of the front plate. On the outside of the front plate, a smaller bearing is press fitted into the front plate. The external bearing is used to support any radial forces that may act on the motor shaft. The coupling design is shown in Figure 4.12. The rotor stub can be seen in the center of the image. Moving towards the right, the coupling, internal bearing, front plate, and external bearing can be seen sequentially. All parts of the cradle were fabricated out of 5051 aluminum.

Complete dimensioned CAD drawings for the motor shaft can be found in Appendix E.1.

#### 4.5.3.2 Motor Shaft

The motor shaft requirements were as follows:

- Minimize radial forces being transferred back to the motor.
- Keep the cost low for a lab test bed setup.

To meet the first requirement, the shaft was made as short as possible to still allow a



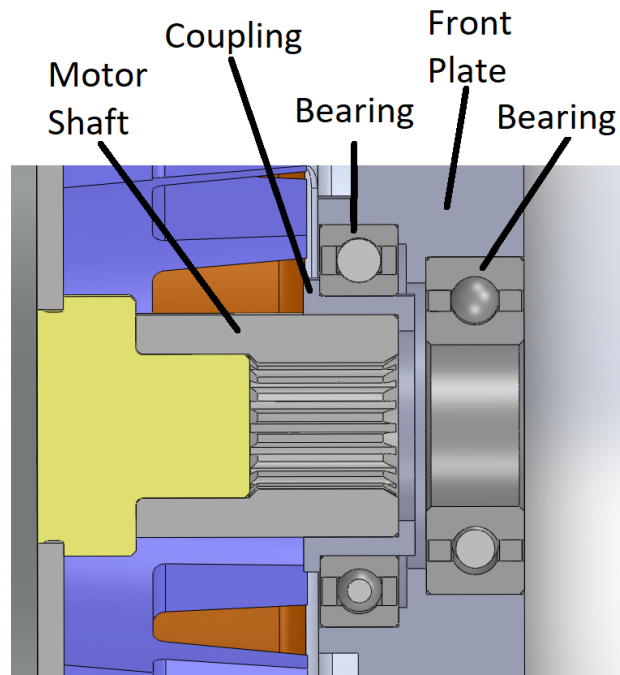


Figure 4.12: Motor Cradle Coupling

torque coupling to connect the two shafts together. The mass was also kept to a minimum to minimize the amount of inertia introduced into the test bed. To mate with the coupling, the mating key was designed as part of the shaft. The shaft was fabricated out of 6061 aluminum. The image of the shaft can be seen in Figure 4.13.

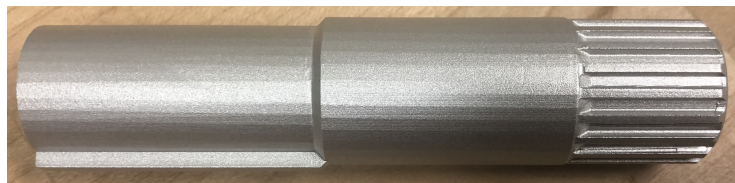


Figure 4.13: Motor Shaft

Complete dimensioned CAD drawings for the motor shaft can be found in Appendix E.2.

To connect the shafts of the two motors together, a coupling was used. Two of the parts are identical, where the shaft slides into the steel flange and the torque is transferred through the keyed element in the shaft, while the third part transfers the torque from

one flange to the other. The flange is a Lovejoy Inc. 6S x 3/4" S-Flex Coupling Flange while the torque transferring component is a Lovejoy Inc. 6JE S-FLEX ethylene propylene diene monomer (EPDM) rubber. The coupling can handle an angular misalignment of  $\pm 2$  degrees between the two shafts, is rated for speeds up to 6000rpm, and can handle a maximum torque transfer capability of 50.8Nm. The motor shaft coupling is shown in Figure 4.14.

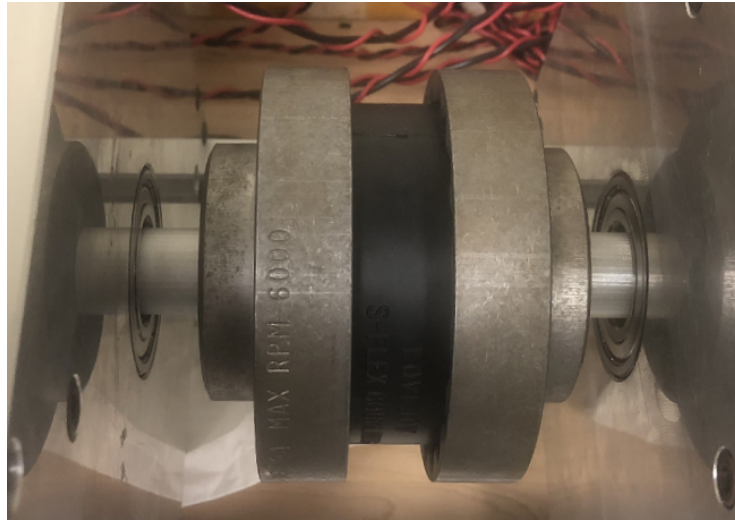


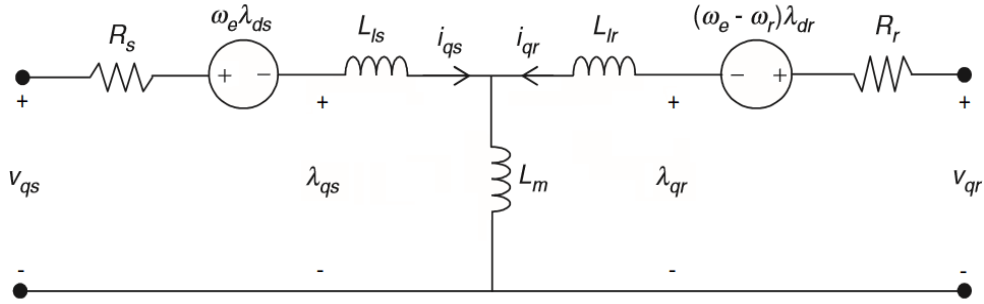
Figure 4.14: Motor Shaft Coupling

#### 4.5.4 Motor Control

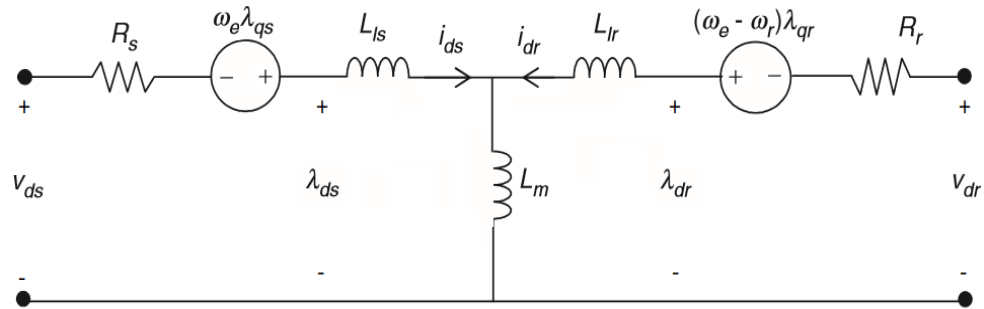
The induction motor equivalent circuit can be represented in the  $d^e$  and  $q^e$  axes by the motor schematics shown in Figure 4.15. The motor quadrature axis schematic is shown in Figure 4.15(a) and the motor direct axis schematic is shown in Figure 4.15 (b).

Based on the above schematics, the equations for the machine can be shown by the matrix in (4.8) [11].

$$\begin{bmatrix} v_{qs} \\ v_{ds} \\ v_{qr} \\ v_{dr} \end{bmatrix} = \begin{bmatrix} R_s + sL_s & w_e L_s & sL_m & w_e L_m \\ -w_e L_s & R_s + sL_s & w_e L_m & sL_m \\ sL_m & (w_e - w_r)L_m & R_r + sL_r & (w_e - w_r)L_r \\ -(w_e - w_r)L_m & sL_m & -(w_e - w_r)L_r & R_r + sL_r \end{bmatrix} \begin{bmatrix} i_{qs} \\ i_{ds} \\ i_{qr} \\ i_{dr} \end{bmatrix} \quad (4.8)$$



(a) Induction Machine Q-Axis Schematic



(b) Induction Machine D-Axis Schematic

Figure 4.15: Synchronously Rotating Reference Frame Motor Schematics [11]

In (4.8),  $v$  is the motor voltage,  $i$  motor current,  $\omega$  speed,  $R$  resistance,  $\lambda$  flux linkage,  $s$  differential operator  $d/dt$ , and  $q, d, s, r, m$ , and  $e$  the subscripts representing the quadrature axis, direct axis, stator, rotor, magnetization, and the electrical reference frame, respectively.

Based on Appendix D, the motor slip and time constant can be derived from the motor equations. The time constant,  $\tau$ , is given by (4.9). This time constant is used in the calculation of slip in the control loop for the motor.

$$\tau = \frac{(L_{lr} + L_m)}{R_r} = \frac{(22\mu H + 1.055mH)}{6.67m\Omega} = 0.161s \quad (4.9)$$

In (4.9),  $\tau$  is the time constant,  $R_r$  the rotor resistance,  $L_{lr}$  is the rotor leakage inductance, and  $L_m$  the magnetization inductance.

### 4.5.5 Slip

In an induction motor, the rotor is always rotating behind the stator magnetic field while operating as a motor. To control the speed of the motor, the slip is controlled based on the quadrature and direct axis current references.

The slip speed of the motor is shown by (4.10) with the complete derivation shown in Appendix D.1.

$$\omega_{sl} = \omega_e - \omega_r = \frac{R_r i_{qs}}{L_r i_{ds}} \left( 1 + s \frac{L_r}{R_r} \right) \quad (4.10)$$

In (4.10),  $\omega_{sl}$  is the slip speed,  $\omega_e$  the electrical speed,  $\omega_r$  the rotor speed,  $R_r$  the rotor resistance,  $i_{qs}$  the quadrature axis stator current,  $L_r$  the rotor inductance,  $i_{ds}$  the direct axis stator current, and  $s$  the differential operator  $d/dt$  in Laplace domain. The derivative component,  $\tau = L_r/R_r$ , identified in the previous section defines how quickly the flux of the motor can change. Therefore, for the purposes of standard motor operation, the flux reference will not change unless operating in the field-weakening mode.

### 4.5.6 D-Axis Flux

The induction motor requires flux to generate a torque. In FOC, flux is controlled by the d-axis component of the stator current, whereas the torque is controlled by the q-axis component. Using Park's transform, the flux component of stator current can be estimated by (4.11).

$$i_{ds} = \frac{\sqrt{\frac{2}{3}} \times V_{rated}}{2 \times \pi \times f_{rated} \times (L_m + L_{ls})} = \frac{\sqrt{\frac{2}{3}} \times 49.7}{2 \times \pi \times 137.1 \times (1.055mH + 25.20\mu H)} = 43.61A_{pk} \quad (4.11)$$

In (4.11),  $i_{ds}$  is the flux component of the stator current,  $V_{rated}$  the motor rated voltage,  $f_{rated}$  the motor rated frequency,  $L_m$  the motor magnetizing inductance, and  $L_{ls}$  the motor stator leakage inductance. The final value of  $43.61A_{pk}$  is the steady state current needed to achieve the rated motor characteristics. This current flows through the motor windings at all times and provides no useful work in terms of torque. The derivation for (4.11) is shown in Appendix D.2.

### 4.5.7 Motor Power

The electronics hardware for both motors was made to be identical, with identical limits. At the rated motor operating conditions, the maximum torque that can be produced is  $13.51Nm$  with  $101.1A_{rms}$  of current and up to  $4021rpm$ , before field weakening is implemented according to (4.12) which is derived in Appendix D.1 [30].

$$T_e = \frac{3P}{2} \frac{L_m^2}{L_r} i_{ds} i_{qs} \quad (4.12)$$

For the purposes of the test bed, both the motor torque and speed capabilities of the test bed are well within the requirements. As the electronics support even higher current capability, there is a mode of operation known as field boosting, where the d-axis flux reference is increased at lower speeds above rated flux. This has the adverse effect of bringing the machine closer to saturation, where the losses will greatly increase [31]. This method would require further testing to determine if core saturation is occurring. An alternative is to continue increasing the quadrature reference until the phase current reaches the maximum hardware capability. At  $150A_{rms}$ , if the d-axis current is kept at rated value, the quadrature current reference can reach a maximum of  $143.5A$  shown by (4.13). This results in a peak torque capability of  $19.40Nm$  that can be achieved for a short period of time.

$$I_{max,pk}^2 = I_{ds,pk}^2 + I_{qs,pk}^2 \quad (4.13)$$

### 4.5.8 Quadrature Encoder Pulse

The speed of both motors is measured through a rotary encoder that provides 64 pulses per revolution on two channels offset by 90 degrees from each other. To increase the speed resolution, both rising and falling edges on each channel are counted, effectively creating 256 pulses per revolution. This provides the smallest measurable angle change of 1.40625 degrees. To get at least one pulse every time the control loop runs, the lowest speed that the motor can run at is  $23.44rpm$ . There is another technique that uses the time period for speed measurements and updates the speed after a set time period so that multiple pulses are obtained and can be divided by the set time period. This provides finer accuracy at low speed, but creates a necessary point to switch between time and frequency based on measurements and was not chosen to be used in the code. Instead, a rolling average filter was implemented to smooth out speed fluctuations, especially at low speed, with a small increase in rise time and overshoot with a step input reference.

### 4.5.9 Current and Voltage Sensors

The voltage and current sensors used in this module are the same as those used in the DC/DC converter comprising of the LEM LV 20-P and LA 150-P. The three-phase voltage on the speed motor was measured to verify motor voltages and allow the possibility of sensorless control in the future. The torque motor does not have any voltage sensors in an effort to save costs as sensorless control was decided not to be used. The voltage sensors are used to measure each phase voltage up to  $\pm 100V_{pk}$ . The current sensors were both designed for the maximum capability of the IGBT at  $\pm 150A_{rms}$ . The low voltage DC level is also monitored to shut down the system in the event the voltage level starts to fall or the communication between modules fails.

The schematics and equations for measuring the AC voltages and currents can be seen in Figure C.1 in Appendix C.1. The component BOM used for the AC sensors are shown in Table C.6 and Table C.7 in Appendix C.4.

### 4.5.10 Motor Operating Regions

Using indirect field-oriented control (IFOC), the induction motor can be operated in different regions shown in Figure 4.16.

Under the motoring mode, the induction machine is able to operate in three different zones. From rest until the base speed, the motor operates in the maximum torque region, where power linearly increases with speed. In this mode, the flux reference is usually constant unless it is reduced trying to minimize losses. Above the base speed, the motor operates in the field weakening mode where the motor is able to achieve constant power and greater speed at the expense of torque and greater slip. The torque performance is reduced with a reduction of flux at a ratio proportional to the inverse of the speed,  $1/\omega$ . To operate the motor at an even greater speed, the flux is reduced at a ratio proportional to the inverse of the speed squared  $1/\omega^2$ , and hence the torque drops at the same rate and the slip remains constant. The power of the motor decreases even further as the stator current decreases while the stator voltage remains constant [32].

To operate in the generation mode of operation, the quadrature current reference reverses sign, and two of the phases in the abc-frame swap places with each other. This allows the motor to operate in two quadrants, with voltage reversal to operate in quadrants 3 and 4 not being allowed. The same limitations outlined for motoring operation are still valid in the generation operation. At any point of operation outlined above, the torque can be lower.

The field weakening mode of operation for the test bed is not required due to the scaling capabilities presented but has been implemented in the controller. The operating region beyond field weakening has not been implemented and is presented here for awareness only. Regenerative braking is accommodated, as it is required for the test bed operation. There is also a mode of operation called field boosting whereby the motor can temporarily increase its current to generate a large increase in torque at the expense of lower efficiency and higher losses. This mode is available for the motor to access during regular operation and no limit in the controller has been placed to restrict this mode.

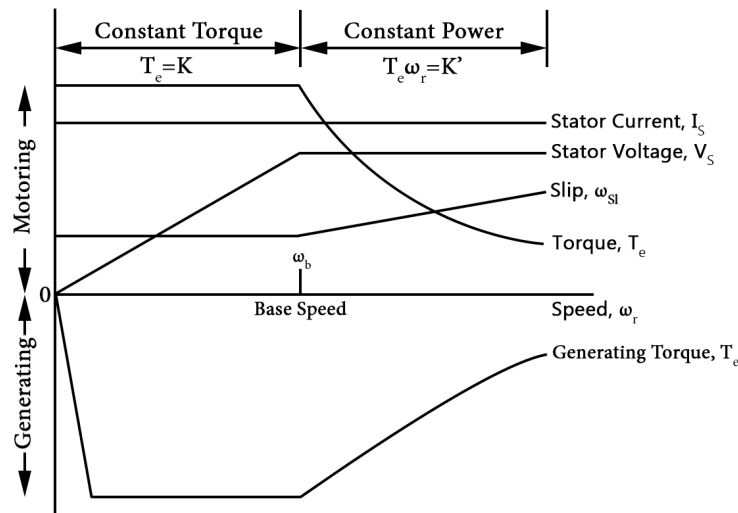


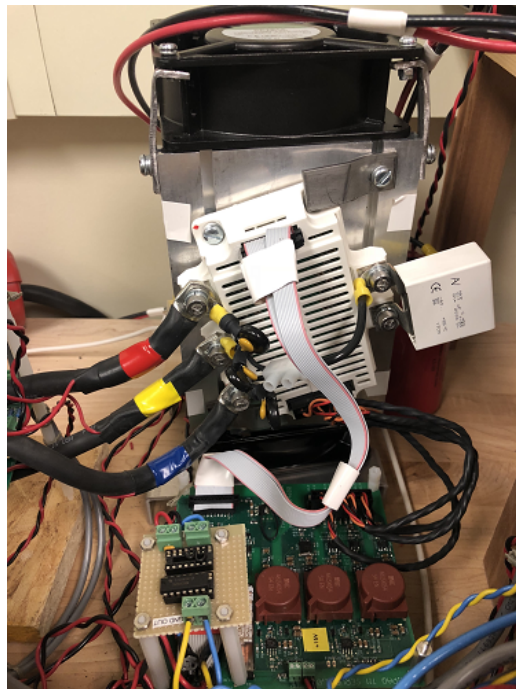
Figure 4.16: Induction Machine Modes of Operation [32]

#### 4.5.11 Complete DC/AC module

The complete DC/AC modules can be seen in Figure 4.17. The motor, cradle, shaft, and controllers are shown in Figure 4.17(a). The speed motor IGBT module, gate driver with power supplies, and mechanical hardware are shown in Figure 4.17(b). The load motor IGBT module, gate driver with power supplies, and mechanical hardware are shown in Figure 4.17(c).

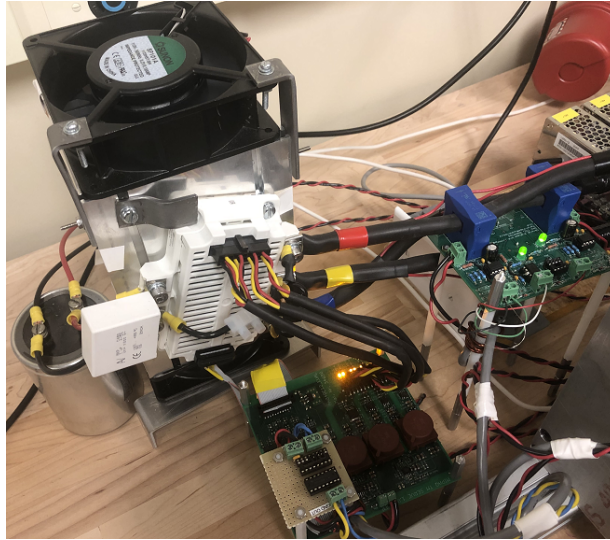


(a) DC/AC Module Motors and Controllers



(b) DC/AC Module Speed Motor Electronics





(c) DC/AC Module Torque Motor Electronics

Figure 4.17: DC/AC Module of Test Bed

## 4.6 Communication

To coordinate the operation of all three control boards together, a means of communication between controllers is required. The I2C communication protocol was chosen utilizing a multi-master coordination approach. The multi-master coordination scheme relies on every module connected to the bus behaving like a slave until a message is ready to be sent out. Each slave has its own address and each message is sent directly between a master and a slave. If bus contention occurs, the slave that is waiting for the bus checks if the bus is free. If the bus does not become free after the maximum time allowed for a message to be sent, the slave is able to force the master off the bus and take control to send out its own message [33]. This communication approach was proven to be very reliable and fast enough to coordinate a full system shutdown in the event a fault occurs. The speed of the bus was set at 400kHz for quick message transfer.

To get data off the microcontrollers, the UART communication protocol was used in unidirectional mode for both DC/AC modules. A UART to USB module, Microchip MCP2200, was used to easily interface to the computers USB ports without the need to change logic levels to RS-232. When the system is running a drive cycle test, data is transmitted to the computer with a resolution of 10ms. The data transfer speed was set to 921,600 baud as the fastest available baud rate for this integrated circuit (IC). To

compensate for timer differences and drift between the two motor controllers, the traction motor controller sends out a synchronization pulse to the load motor controller at a 1s interval on the I2C bus. The load motor controller relies on its own timer to create the reference torque set points until the next synchronization pulse is received. In the event synchronization between the two controllers is lost, a global command to shut down the entire system is sent.

The system’s communication scheme is shown in Figure 4.18.

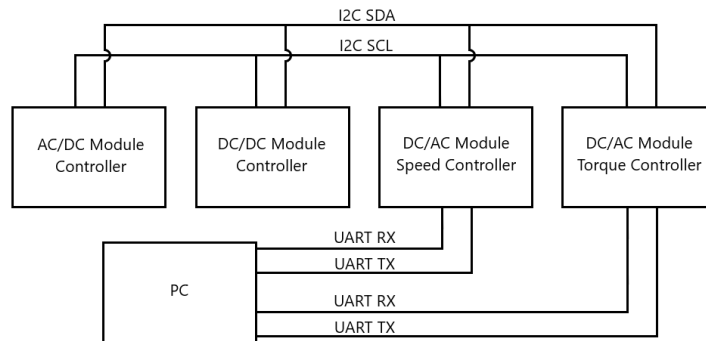


Figure 4.18: Test Bed Communication Scheme

In 4.18, I2C is the Inter-Integrated Circuit communication protocol, SDA the serial data line, SCL the serial clock line, UART the Universal asynchronous receiver-transmitter communication protocol, RX receive, and TX transmit.

For both of these protocols, the transfer of data occurs automatically. The code loads the data into the direct memory access (DMA) in the microcontroller, and the hardware sends it out when it is able to, without any further interaction from the user code.

## 4.7 HIL Test Bed Results

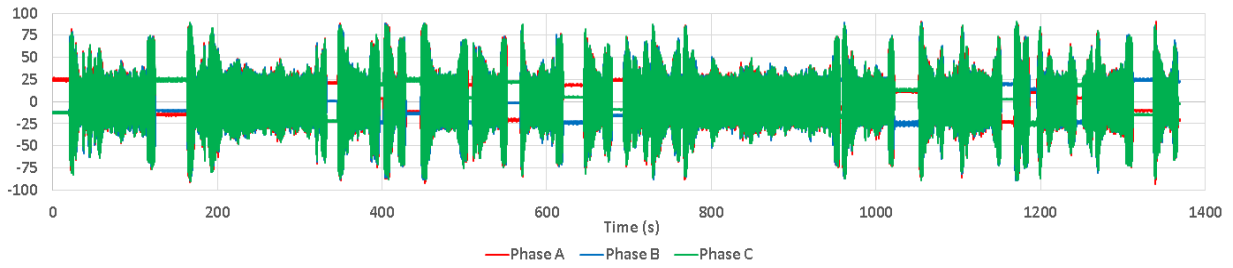
The scaled UDDS drive cycle was run on the HIL test bed. To confirm the simulation and theoretical results, the entire UDDS drive cycle model was run and validated. The speed motor is the traction motor of the vehicle and the load motor emulates all the forces acting against the vehicle. The setup is identical to the one in simulation. The colors have also been kept similar to those in the simulation for comparison purposes. The test bed results for the entire drive cycle are shown in Figure 4.19.

In Figure 4.19, the results of running the UDDS drive cycle on the HIL test bed are shown. Figure 4.19(a) shows the AC currents in the traction motor. Similarly to the simulation results, the points where the motor currents are constant indicates the motor has stopped rotating and is maintaining its magnetic field flux. All three phases are shown with the colors red, blue, and green on the graph, representing phases A, B, and C, respectively. The traction motor control loop is designed to track only the speed of the shaft while staying within the current limits of the hardware. In the event the speed is unable to be maintained, the inner current controllers become limited, causing the current reference, and hence the torque to be capped. The speed reference and the tracked speed are shown in Figure 4.19(b). This figure shows that the traction motor tracks the reference speed precisely.

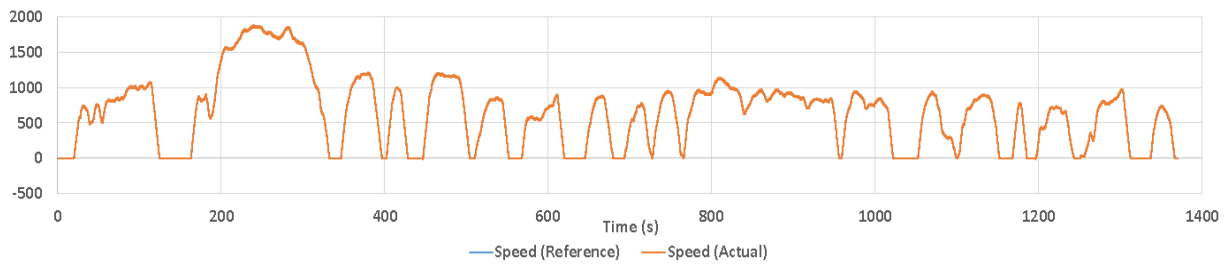
The load motor reference and tracked torques are shown in Figure 4.19(c). This figure implies the losses in the HIL test bed when compared to an ideal case shown in simulation. The results show that in the majority of cases, the load motor is lowering the torque that the traction motor is required to output on the shaft. The fact that the load motor is adding torque to the system so that the traction motor is able to follow the UDDS cycle while maintaining the conservation of energy is an indicator that the system has loss. The losses show what the models in simulation cannot predict with ease and the advantage of the HIL test bed when refining models and system designs. However, with the particular test bed design, as the speed is increased, the losses increase proportionally, indicating the majority of losses experienced are due to friction.

Due to the design of the test bed, the load motor is able to compensate for these losses in real-time by knowing its own traction motor and shaft torques. This advantage removes the requirement to have the HIL system mapped out in an efficiency vs. torque vs. speed graph with lookup tables in code. The added effect of temperature makes this task even more difficult.

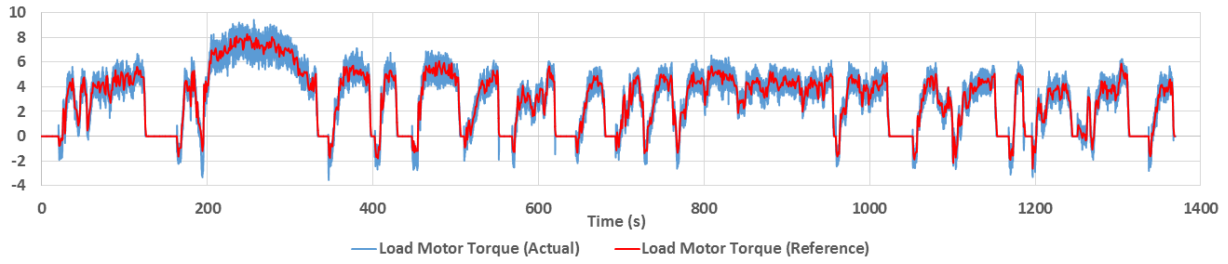
The traction motor tracked torque is also shown in Figure 4.19(d). It can be seen that the torque is being compensated by the load motor very well and the traction motor is outputting the desired torque at the same rate as in the simulation results. The torque ripples seen in simulation are also seen in the actual test bed, which can be explained by the high  $di/dt$ , and hence fast changes in torque calculated after every iteration of the control loop. Finally, the mechanical power of the traction motor is shown in Figure 4.19(e), as a product of the motor shaft speed and the traction motor torque.



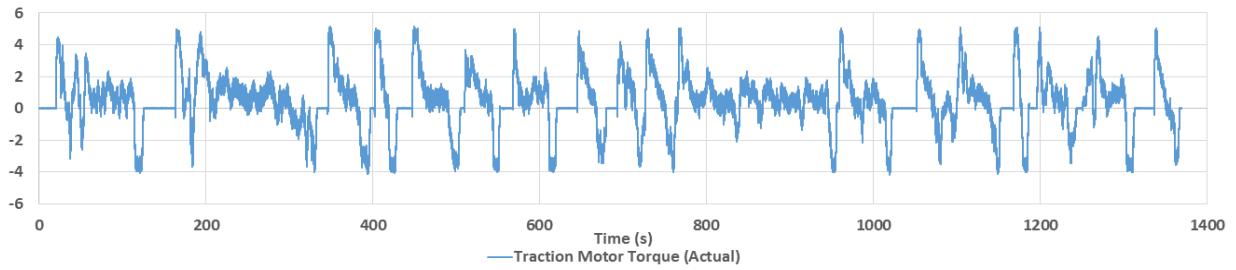
(a) Traction Motor AC Currents in A



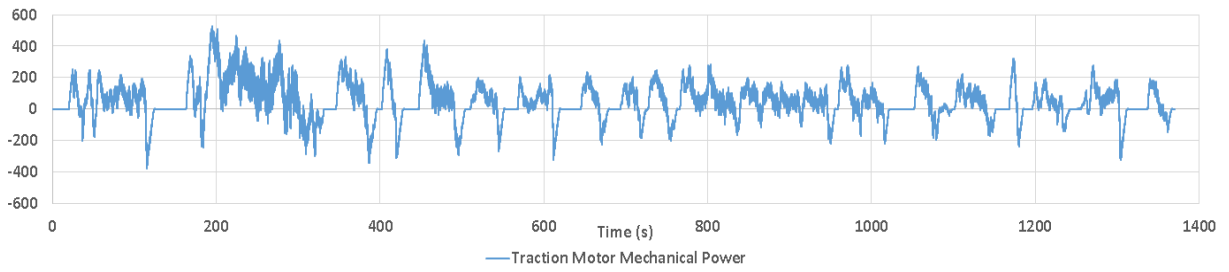
(b) Traction Motor Speed Reference and Tracked Speed in RPM



(c) Load Motor Reference and Tracked Torques in Nm



(d) Traction Motor Tracked Torque in Nm



(e) Traction Motor Mechanical Power in W

Figure 4.19: HIL Test Bed Results of Scaled Vehicle

# Chapter 5

## Result Analysis

### 5.1 System Layout

In the previous chapters, the simulation and practical results of the scaled version of the full UDDS drive cycle were presented. To analyze the results in greater detail, in this chapter, the theoretical, simulation, and practical results will be compared side-by-side at different points in time to ensure all three closely agree. Following this, the results will be scaled up independently for each test scenario with the error percentages compared to the theoretical values.

### 5.2 Scaled Result Comparison

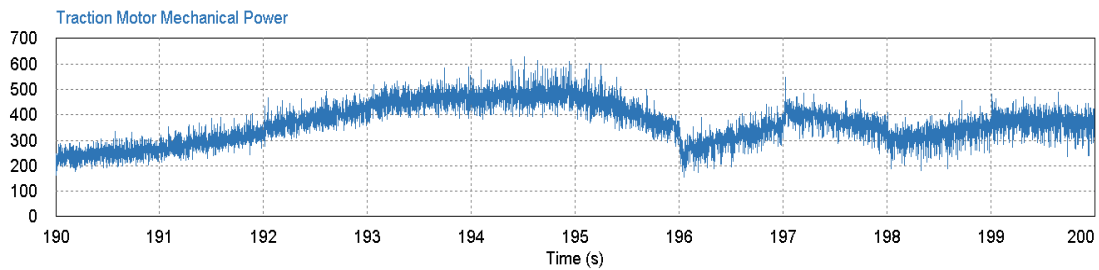
Three different time instants will be taken for consistency and verification each focusing on a different area of the drive cycle. The areas of interest that will be analyzed are the time locations in the scaled UDDS cycle when maximum power, maximum speed, and maximum traction motor torque occur. The purpose of selecting these specific points in the drive cycle is to examine the hardest cases and determine if the scaling approach and test bed implementation is a viable alternative to the full-size vehicle model.

Zoomed-in images showing the moment of time of interest along with 5s before and 5s after, will be evaluated in detail. For the scaling up calculations to the full-size vehicle and percentage error, 0.2s of data before and after the moment of time of interest will be averaged.

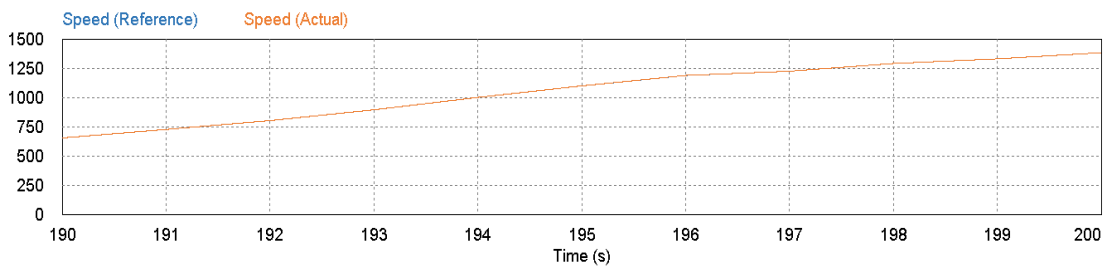
As mentioned in the previous chapter, the advantage of the test bed is that any lossy elements can be compensated for by the load motor. Therefore, it is expected to see all HIL and simulation graphs match with each other except the load motor torque curves.

### 5.2.1 Maximum Power

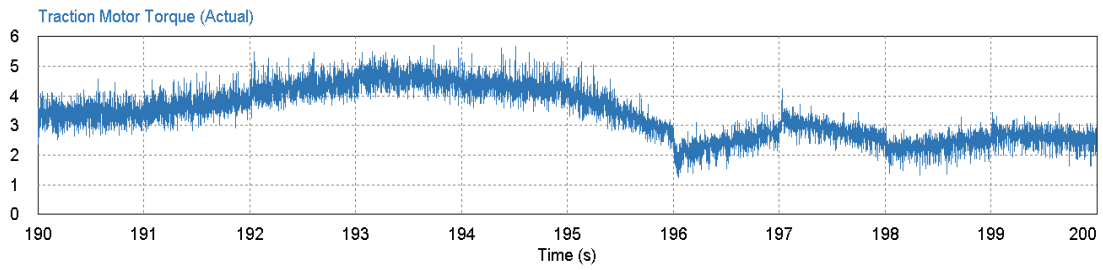
The first set of results correspond to the case of 195s into the UDDS drive cycle at which maximum power occurs. The simulation results are shown in Figure 5.1 and the test bed results are shown in Figure 5.2. The traction motor power is shown in Figures 5.1(a) and 5.2(a), the motor shaft speed is shown in Figures 5.1(b) and 5.2(b), the traction motor torque in Figures 5.1(c) and 5.2(c), and the load motor reference and tracked torques in Figures 5.1(d) and 5.2(d).



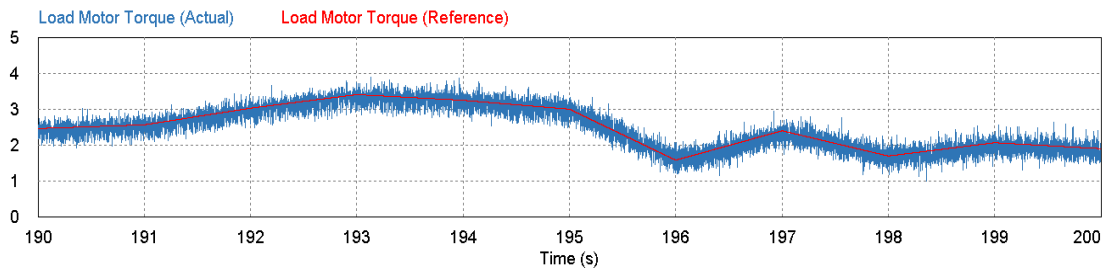
(a) Traction Motor Power (W)



(b) Motor Shaft Speed (RPM)

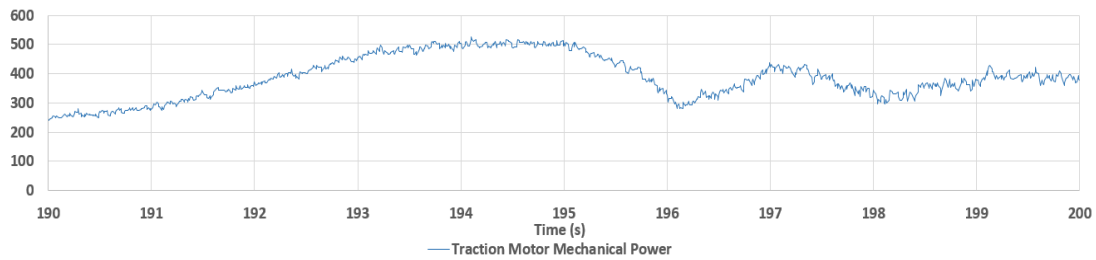


(c) Traction Motor Torque (Nm)

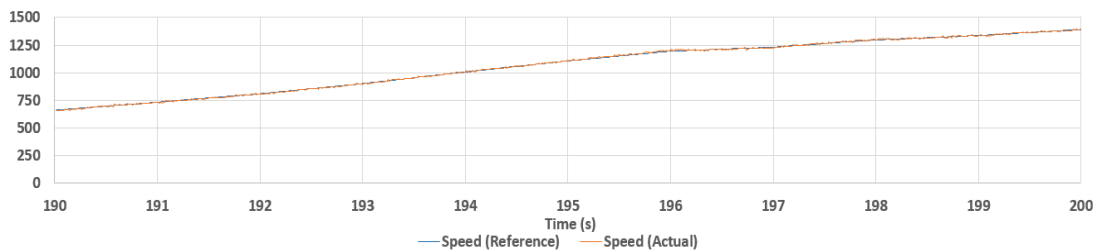


(d) Load Motor Reference and Tracked Torques (Nm)

Figure 5.1: Simulation - UDDS Cycle at 195 Seconds Showing Maximum Power

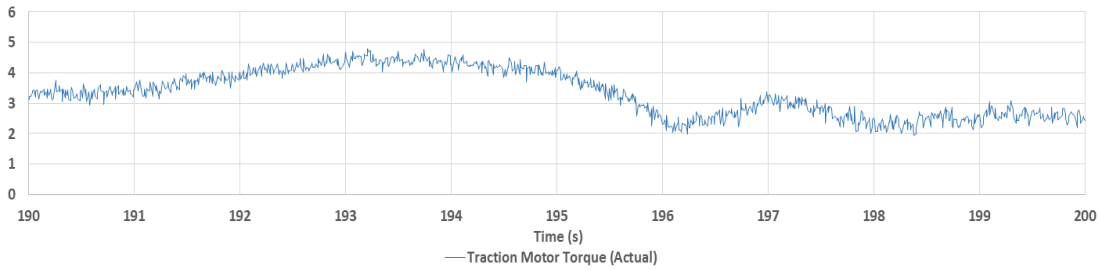


(a) Traction Motor Power (W)

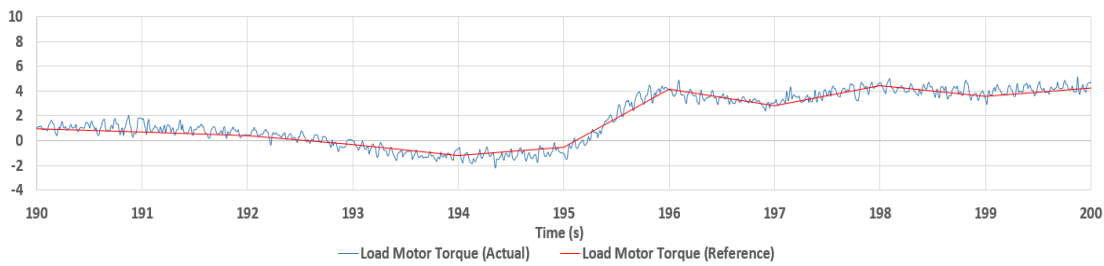


(b) Motor Shaft Speed (RPM)





(c) Traction Motor Torque (Nm)



(d) Load Motor Reference and Tracked Torques (Nm)

Figure 5.2: Test Bed - UDDS Cycle at 195 Seconds Showing Maximum Power

Upon inspection, it is evident that the simulation and test bed results closely agree. In both cases, the speed tracking is seen to be excellent with minimal ripple. The torques of both traction and load motors appear to have more ripple in simulation results compared to the test bed counterpart, which results in the mechanical power in the simulation to also have more ripple than that of the test bed, as it is a product of speed and traction motor torque. A possible reason for this could be that the test bed has a physical coupling element with an EPDM rubber joining the two motor shafts together, allowing some of the torque ripples to be smoothed out. There are also rotational loss elements, such as friction, which may also contribute to a smoother torque profile.

In Figure 5.2(c), it can be seen that the traction motor torque is very similar to the simulation shown in Figure 5.1(c). At the time interval between 195s and 196s into the simulation, there is a sharp  $d\tau/dt$  change for the load motor, where the load motor changes from generating to motoring to emulate the environment properly seen in Figure 5.2(d). Even under this condition, the traction motor is still able to deliver the correct results. In the ideal environment in simulation, the load motor behaves completely differently, seen in Figure 5.1(d), delivering less power during the sharp  $d\tau/dt$  change which can be attributed to no frictional losses.

The specific results for maximum power at  $195s \pm 0.2s$  are taken and compared to the theoretical results, as shown in Table 5.1. The percentage change is shown for the simulation and test bed where the new value is considered to be the simulation or test bed result, respectively, and the old value is considered to be the theoretical calculation.

Table 5.1: UDDS Cycle at Maximum Power (195 Seconds) Comparing Theoretical, Simulation, and Test Bed Results

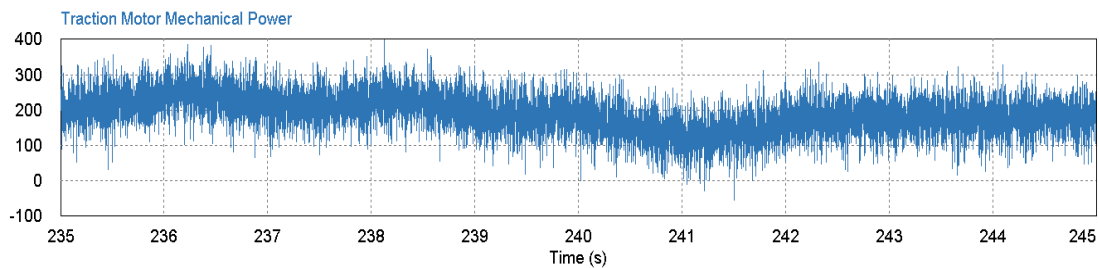
UDDS Cycle - 195s - Maximum Power								
	Theoretical		Simulation			Test Bed		
	Full-size	Scaled Down	Scaled Down	Scaled Up	Error (%)	Scaled Down	Scaled Up	Error (%)
Mechanical Power – P ( $W$ )	45068.77	461.50	472.67	46171.15	2.446	491.70	44403.79	1.475
Traction Motor Torque – $T_T$ ( $Nm$ )	109.51	3.99	4.08	112.23	2.483	3.92	107.80	1.564
Motor Rotational Speed – $\omega$ ( $rpm$ )	3930.10	1105.69	1105.26	3928.58	0.039	1106.66	3933.53	0.087
Linear velocity – $v$ ( $m/s$ )	14.889	5.956	5.953	14.883	0.040	5.961	14.902	0.087

It can be seen from the results in Table 5.1 at maximum power that the error between simulation and the test bed is very minimal consisting of percentage errors lower than 2%. The speed is being tracked better on the simulation than on the test bed; however, the torque on the test bed is tracking more closely to the theoretical reference. Therefore, the error is reduced across both systems.

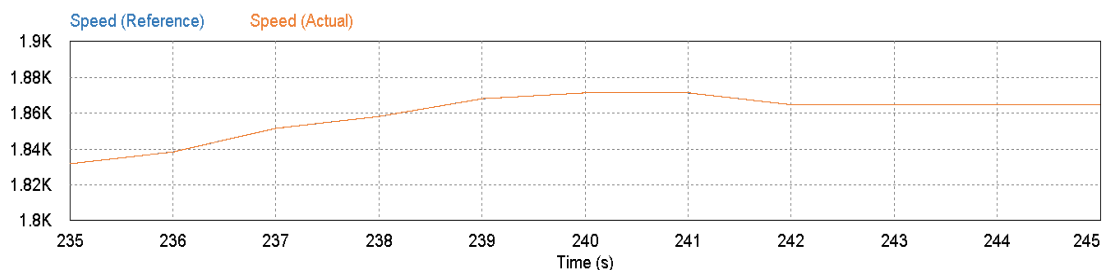
### 5.2.2 Maximum Speed

The second analysis is for 240s into the UDDS drive cycle at which maximum speed occurs. The simulation results are shown in Figure 5.3 and the test bed results are shown in Figure

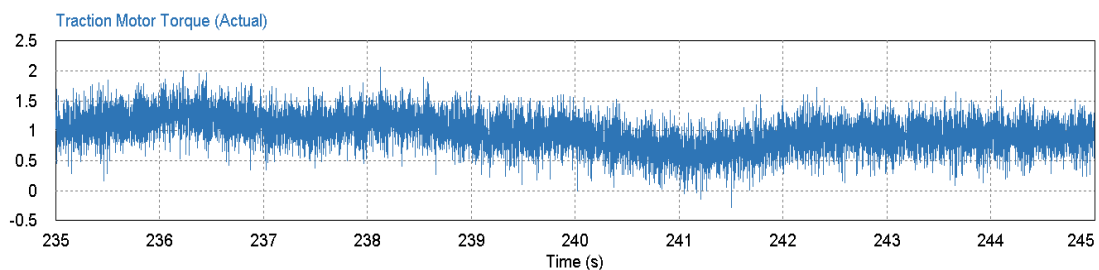
5.4. The traction motor power is shown in Figure 5.3(a) and 5.4(a), the motor shaft speed in Figures 5.3(b) and 5.4(b), the traction motor torque in Figures 5.3(c) and 5.4(c), and the load motor reference and tracked torques in Figures 5.3(d) and 5.4(d).



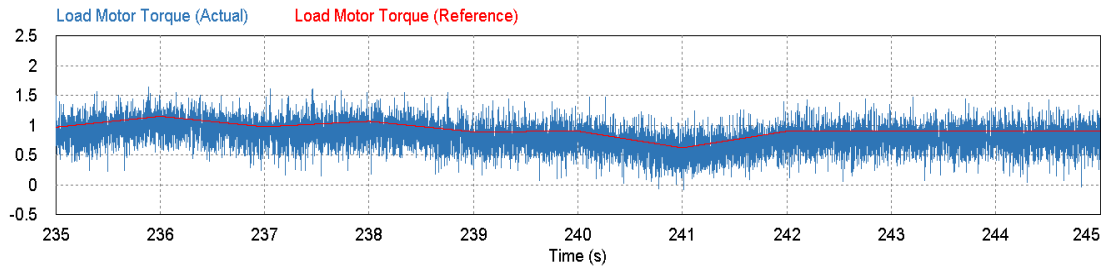
(a) Traction Motor Power (W)



(b) Motor Shaft Speed (RPM)

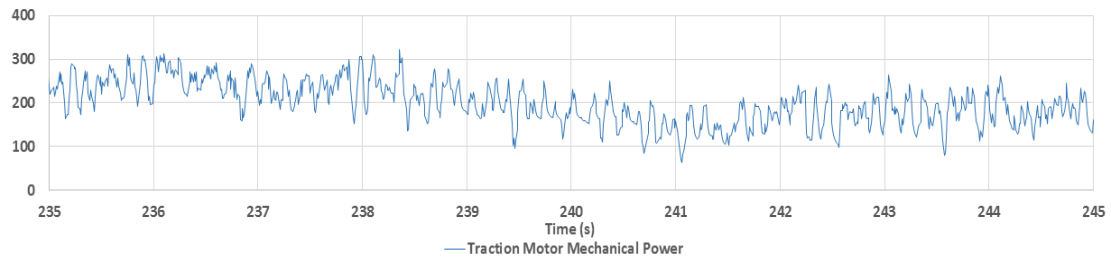


(c) Traction Motor Torque (Nm)

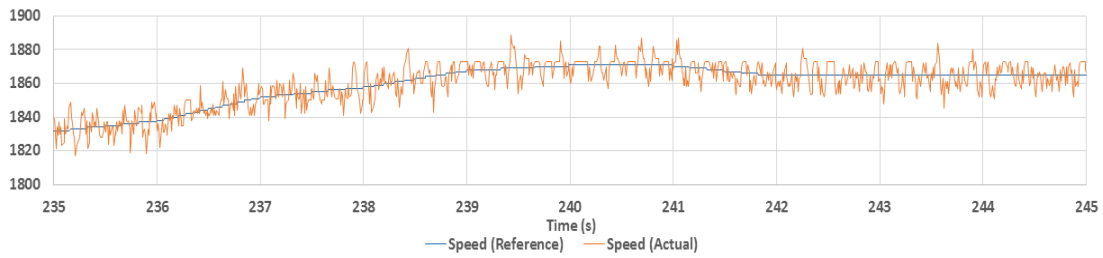


(d) Load Motor Reference and Tracked Torques (Nm)

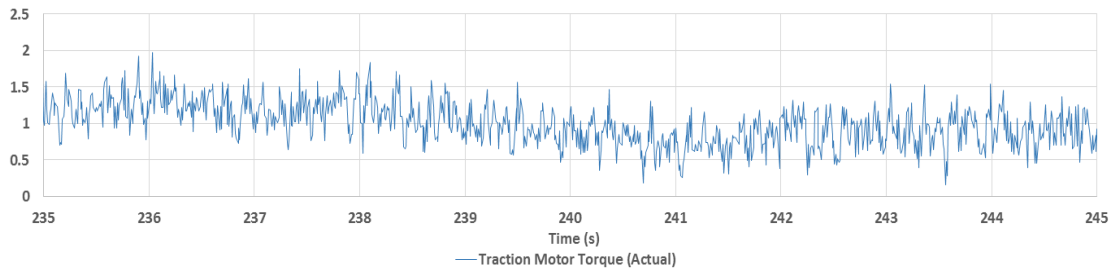
Figure 5.3: Simulation - UDDS Cycle at 240 Seconds Showing Maximum Speed



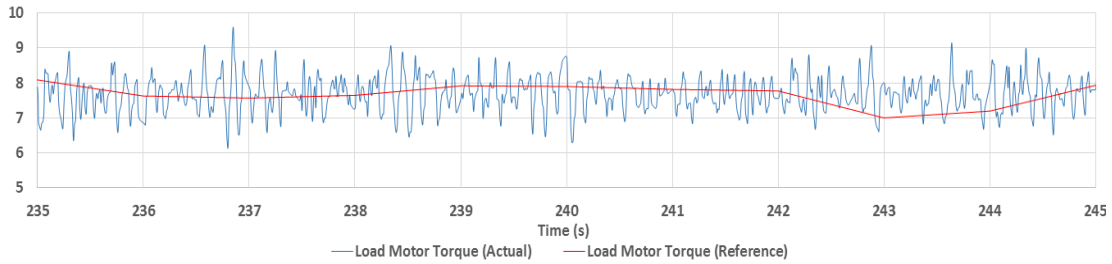
(a) Traction Motor Power (W)



(b) Motor Shaft Speed (RPM)



(c) Traction Motor Torque (Nm)



(d) Load Motor Reference and Tracked Torques (Nm)

Figure 5.4: Test Bed - UDDS Cycle at 240 Seconds Showing Maximum Speed

It can be seen that at maximum speed, the torque ripple appears to be around 50% higher than at maximum power. This can be seen in both the simulation and test bed results. Both the simulation and test bed have torque ripples that oscillate around  $1Nm$  for the traction motor as seen in Figures 5.3(c) and 5.4(c). Irrespective of the ripple, the simulation and test bed motors track their respective torque references very well. Similarly to the maximum power case for the test bed, the torque ripples do not couple directly from load motor to the traction motor. The load motor torque ripple on the test bed reaches up to  $3Nm$  at the worst case while the traction motor torque ripple reaches about  $1Nm$  at the worst case.

The speed control in the simulation is excellent with no visible ripple seen, even at  $20rpm$  per division resolution. The speed ripples seen on the test bed setup oscillate by about  $30rpm$  but the tracking is very good. The combination of ripples of the torque and speed motors result in the mechanical ripple of about  $200W$  at the worst case on both the simulation and test bed. It can also be seen that the load motor is adding a lot of torque to the shaft to lower the amount of power required by the traction motor. Once again, this is very different from the simulation. In section 4.7, the amount of torque assistance from the load motor appears to be strongly correlated to the system mechanical speed, indicating that there are quite large losses that affect the system proportionally with respect to speed.

The specific results for maximum speed at  $240s \pm 0.2s$  are taken and compared to the theoretical results, as shown in Table 5.2. The percentage change is shown for the simulation and test bed where the new value is considered to be the simulation or test bed result, respectively, and the old value is considered to be the theoretical calculation.

It can be seen from the results in Table 5.2 at maximum speed that the error between simulation and the test bed is relatively small consisting of percentage errors of around 5%. One of the major contributors to this larger than normal error is the definition to take samples  $0.2s$  before and after the time point of interest for a large enough sample size.

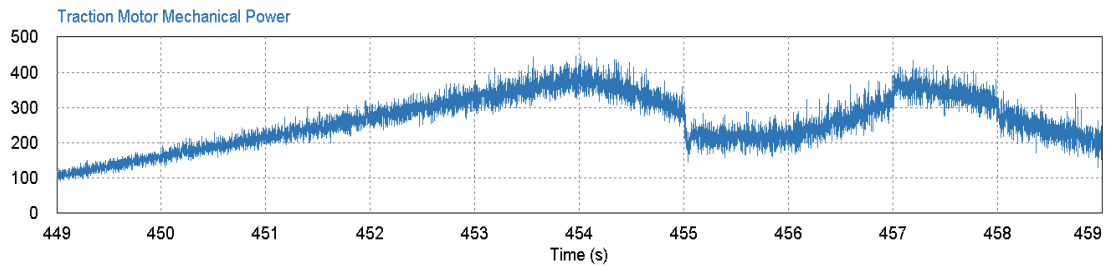
Table 5.2: UDDS Cycle at Maximum Speed (240 Seconds) Comparing Theoretical, Simulation, and Test Bed Results

UDDS Cycle - 240s - Maximum Speed								
	Theoretical		Simulation			Test Bed		
	Full-size	Scaled Down	Scaled Down	Scaled Up	Error (%)	Scaled Down	Scaled Up	Error (%)
Mechanical Power – $P$ ( $W$ )	17333.65	177.50	180.68	17644.99	1.796	172.34	16450.31	5.096
Traction Motor Torque – $T_T$ ( $Nm$ )	24.88	0.91	0.92	25.33	1.798	0.860	23.62	5.068
Motor Rotational Speed – $\omega$ ( $rpm$ )	6651.84	1871.43	1871.26	6651.73	0.002	1870.88	6649.89	0.029
Linear velocity – $v$ ( $m/s$ )	25.200	10.08	10.079	25.200	0.009	10.077	25.193	0.083

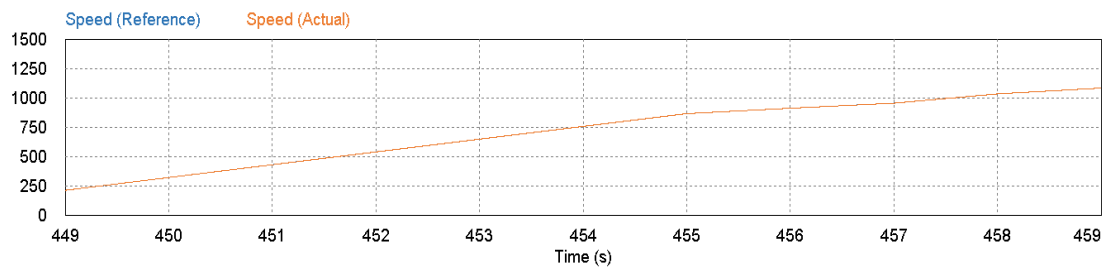
The speed percentage error is excellent with percentage errors of less than 0.03% for both simulation and the test bed.

### 5.2.3 Maximum Torque

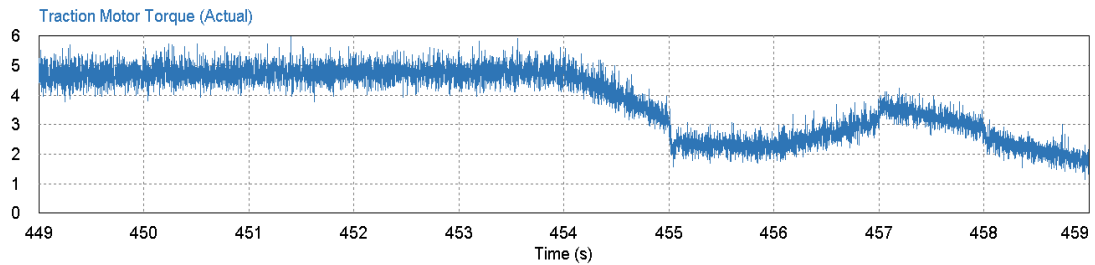
The third analysis is for 454s into the UDDS drive cycle at which maximum torque occurs. The simulation results are shown in Figure 5.5 and the test bed results are shown in Figure 5.6. The traction motor power is shown in 5.5(a) and 5.6(a), the motor shaft speed in Figures 5.5(b) and 5.6(b), the traction motor torque in Figures 5.5(c) and 5.6(c), and the load motor reference and tracked torques in Figures 5.5(d) and 5.6(d).



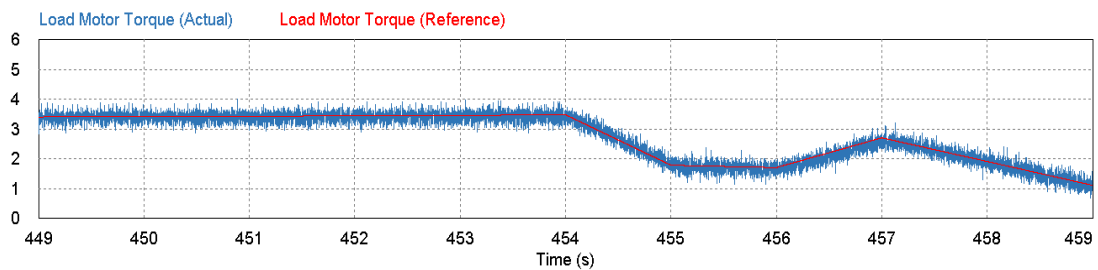
(a) Traction Motor Power (W)



(b) Motor Shaft Speed (RPM)

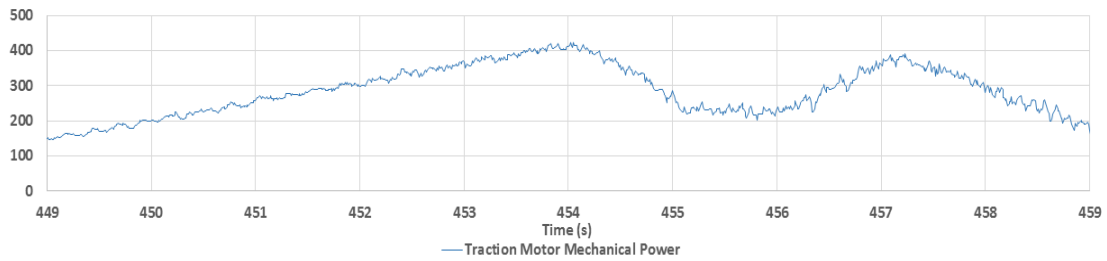


(c) Traction Motor Torque (Nm)

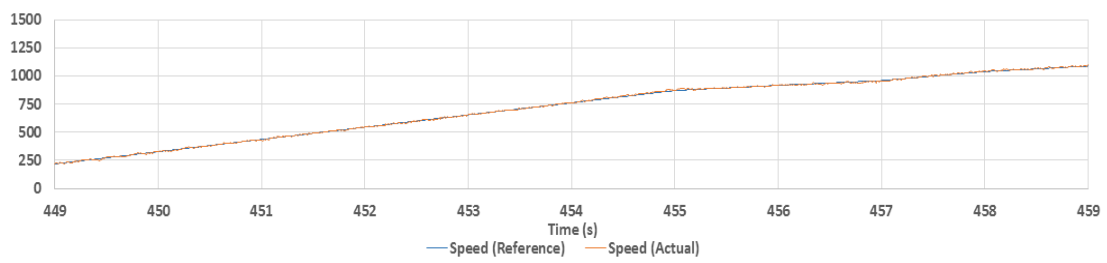


(d) Load Motor Reference and Tracked Torques (Nm)

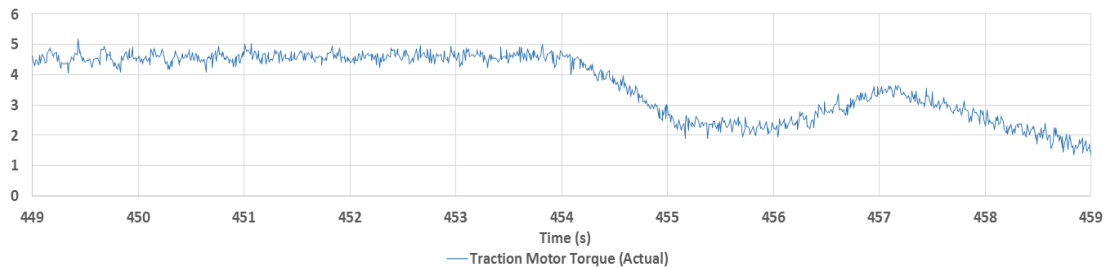
Figure 5.5: Simulation - UDDS Cycle at 454 Seconds Showing Maximum Torque



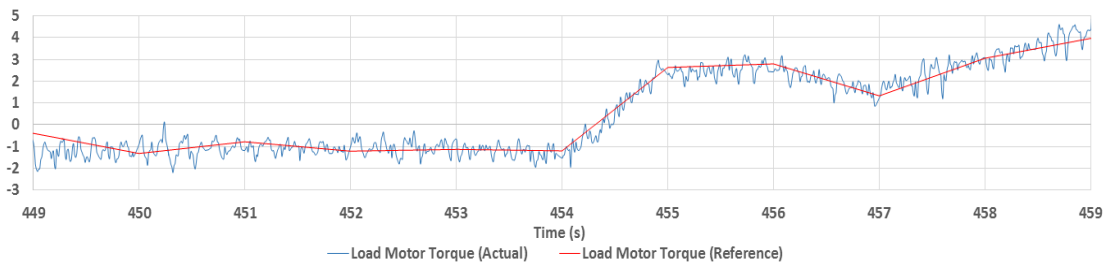
(a) Traction Motor Power (W)



(b) Motor Shaft Speed (RPM)



(c) Traction Motor Torque (Nm)



(d) Load Motor Reference and Tracked Torques (Nm)

Figure 5.6: Test Bed - UDDS Cycle at 454 Seconds Showing Maximum Torque



The torque ripple for the traction motor in both simulation and test bed, shown in Figures 5.5(c) and 5.6(c), starts higher at the beginning of the zoomed-in section and begins to envelope to a smaller torque ripple at peak torque required in the drive cycle. The ripple in simulation and on the test bed is below  $1Nm$ . Load motor torque tracking is excellent for both systems.

The speed tracks very well as usual with almost no ripples seen. The mechanical power graphs seen in Figure 5.5(a) and Figure 5.6(a) also exhibit enveloping in the ripple, but are opposite of the torque pattern, starting small, and growing larger and then becoming constant once peak torque is achieved.

Table 5.3: UDDS Cycle at Maximum Torque (454 Seconds) Comparing Theoretical, Simulation, and Test Bed Results

UDDS Cycle - 454s - Maximum Torque								
	Theoretical		Simulation			Test Bed		
	Full-size	Scaled Down	Scaled Down	Scaled Up	Error (%)	Scaled Down	Scaled Up	Error (%)
Mechanical Power – $P$ (W)	3529.22	371.03	375.83	36702.23	1.294	409.07	35582.93	1.795
Traction Motor Torque – $T_T$ (Nm)	127.68	4.65	4.70	129.36	1.318	4.56	125.17	1.959
Motor Rotational Speed – $\omega$ (rpm)	2710.01	762.43	762.50	2709.36	0.024	763.71	2714.54	0.167
Linear velocity – $v$ (m/s)	10.267	4.107	4.106	10.264	0.024	4.114	10.284	0.167

It can be seen from the results at maximum torque in Table 5.3 that the error between simulation and the test bed is relatively small consisting of percentage errors of less than 2%. The simulation results are very close to the theoretical values, while the test bed results show slightly larger errors. The speed error for the test bed is less than 0.2%, implying that the actual speed is extremely close to the reference target. Overall, the torque percentage error has been kept to a minimum with reproducible results.

# Chapter 6

## Conclusion and Recommendations

### 6.1 Conclusion

In this thesis, a systematic approach to down-scaling full-size electric vehicles' parameters and environmental conditions to a level that can be handled by the small-scale hardware-in-the-loop simulation test bed developed in the lab has been achieved. The approach for taking the full-size vehicle parameters down to a model vehicle level has been shown utilizing an arbitrary scaling factor, where the scaled vehicle model can be physically built or transferred onto a test bed setup. The approach for transferring the results obtained from the simulation and hardware-in-the-loop test bed back to either the scaled down vehicle model or the full-size vehicle have been shown to successfully work. This was done by running the complete UDDS drive cycle at a scaled level with a theoretical gearbox implemented in software.

The system setup consists of two electric motors whose shafts are connected together through a coupling. One electric machine, the traction motor, was tasked with controlling the speed, while the other electric machine, the load, was tasked with controlling the torque of the shaft. A sensed field-oriented control approach was implemented for both motors with SVPWM switching to the IGBTs.

Three important operating points were investigated to ensure the testbed was performing as desired over the scaled UDDS drive cycle. The areas examined for scrutiny were maximum power, maximum speed, and maximum torque. For all three cases, the motor shaft speed tracking in simulation was shown to have almost no ripple with the actual speed following the reference speed very precisely. The same test on the bed setup was

shown to result in a peak-to-peak ripple of about  $30rpm$  that was observed during the maximum speed test case.

The torque ripple results for the simulation and test bed were also shown to be very similar. For all three cases, the torque ripple in simulation was shown to have an average peak-to-peak ripple of approximately  $1Nm$ , with the worst case having a peak-to-peak ripple of approximately  $1.5Nm$  in the maximum torque case. The torque ripple for the test bed was shown to vary and be closely correlated with speed, with the ripple increasing as the speed increased. The load motor, tasked with controlling the torque, was seen to have a torque ripple larger than what was observed for the traction motor. It is seen that the coupling between the two motors provides some damping to the torque oscillations and torque ripples are smoothed out to some extent at the traction motor. During the worst case, at maximum speed, the load motor has a peak-to-peak torque ripple of approximately  $3Nm$  while the traction motor is seen to have a peak-to-peak torque ripple of approximately  $1Nm$  in the same case.

Due to the simulation being performed in an ideal environment, the transfer of energy from one motor to the other is perfect. On the test bed, the transfer of energy is associated with losses. The load motor compensates the system more as the speed increases indicating the losses are speed-related and can be attributed mainly to rotational friction losses.

The results of scaled UDDS drive cycle run in simulation and on the test bed are scaled up to that of a full-size vehicle. The simulation results are shown to be very good with the error being less than 3% for the maximum power case and less than 2% for the maximum speed and maximum torque cases. The results of the drive cycle on the test bed also demonstrate a low percentage error of less than 2% for the maximum power and maximum torque cases, and less than 6% for the maximum speed case.

The results obtained from the simulation and on test bed show that the scaling approach to verifying the design of a full-size vehicle results in data containing minimal error and can speed up the time to market for the development of next generation electric vehicles.

## 6.2 Recommendations

The system performs very well with its current design state. However, there are some areas of improvement that can be addressed to make performance even better.

One of the main areas for concern is the available CPU processing power left on the Texas Instruments TMS320F28335. To perform the current motor control functions, the

traction and load motor microcontrollers utilize approximately 93% of their available processing power. The majority of processing power is used up by the ADC and Park's transformations. To implement any further improvements to the system such as monitoring voltages for sensorless field oriented control, the microcontroller will need to be upgraded to a faster and more sophisticated model. It would also be worthwhile to redesign the daughter board that sits on top of the control card to reduce EMI from the PWM signals and implement the additional features required by the motor controller, such as a UART transceiver on the board and proper quadrature encoder pulse input connectors.

Another area of improvement is reducing the amount of friction on the motor shaft to improve the efficiency of the system. The interference fit between the motor coupling and bearing that fits into the front face is too tight and creates frictional losses when the motor is turning. The motor shafts could also be aligned by a laser instead of by eye to reduce vibrations in the system and allow it to go to its maximum speed more easily.

A third area of improvement would be optimizing the flux vs. loss characteristics of the motors. Currently, the direct axis flux reference is kept constant. However, for optimal efficiency, the flux reference can be lowered when the full torque capability of the motor is not being used at the expense of a decrease in the rate of rise of commanded torque. This should improve the motor efficiency further.

A final area for improvement is changing the two motor controllers' IGBT modules from 150A capability to ones that can handle 300A. This would allow the maximum torque capability of the motors to be increased from  $19.40Nm$  to the maximum peak torque that the motor can handle, i.e.,  $70.50Nm$ . This would allow the maximum design power of the AC/DC and DC/DC modules to be realized. As a long term goal, the electric motors can be changed to ones with higher rated voltage to allow for a higher test bed motor shaft speed

# References

- [1] K. Fang, Y. Zhou, P. Ma, and M. Yang, “Credibility Evaluation of Hardware-in-the-Loop Simulation Systems,” in *2018 Chinese Control And Decision Conference (CCDC)*, Shenyang, China, Jun. 2018, pp. 3794–3799.
- [2] A. Bouscayrol, “Different types of Hardware-In-the-Loop simulation for electric drives,” in *2008 IEEE International Symposium on Industrial Electronics*, Cambridge, United Kingdom, Jun. 2008, pp. 2146–2151.
- [3] W. Hongyu, Y. Zhiqiang, F. Yong, Q. Yunqian, and L. Zhiming, “Development of pure electric vehicle powertrain controller based on hardware in the loop platform,” in *2015 6th IEEE International Conference on Software Engineering and Service Science (ICSESS)*, Beijing, China, Sep. 2015, pp. 498–502.
- [4] Y. Zhu, H. Hu, G. Xu, and Z. Zhao, “Hardware-in-the-Loop Simulation of Pure Electric Vehicle Control System,” in *2009 International Asia Conference on Informatics in Control, Automation and Robotics*, Bangkok, Thailand, Feb. 2009, pp. 254–258.
- [5] B. Tabbache, Y. Aboub, K. Marouani, A. Kheloui, and M. Benbouzid, “A simple and effective hardware-in-the-loop simulation platform for urban electric vehicles,” in *2012 First International Conference on Renewable Energies and Vehicular Technology*, Hammamet, Tunisia, Mar. 2012, pp. 251–255.
- [6] C. Patil, R. Longoria, and J. Limroth, “Control prototyping for an anti-lock braking control system on a scaled vehicle,” in *42nd IEEE International Conference on Decision and Control (IEEE Cat. No.03CH37475)*, Maui, USA, Dec. 2003, pp. 4962–4967 Vol.5.
- [7] P. Fajri, N. Lotfi, M. Ferdowski, and R. Landers, “Development of an Educational Small Scale Hybrid Electric Vehicle (HEV) Setup,” in *2013 IEEE International Electric Vehicle Conference (IEVC)*, Santa Clara, USA, Oct. 2013, pp. 1–6.

- [8] R. Verma, D. Vecchio, and H. Fathy, “Development of a Scaled Vehicle With Longitudinal Dynamics of an HMMWV for an ITS Testbed,” *IEEE/ASME Transactions on Mechatronics*, vol. 13, pp. 46–57, Feb. 2008.
- [9] P. Lotrakul, P. Pereirinha, and A. Bouscayrol, “Reduced-Scale Hardware-In-the-Loop Simulation of an Urban Electric Minibus Using Energetic Macroscopic Representation,” in *2017 IEEE Vehicle Power and Propulsion Conference (VPPC)*, Belfort, France, Dec. 2017, pp. 1–6.
- [10] C. Mayet, A. Bouscayrol, P. Delarue, E. Chattot, and I. Dekik, “Reduced-Scale-Power Hardware-In-the-Loop Simulation of a Subway Line,” in *2015 IEEE Vehicle Power and Propulsion Conference (VPPC)*, Montreal, Canada, Oct. 2015, pp. 1–6.
- [11] M. Rashid, *Power Electronics Handbook*. New York, USA: Elsevier Inc., 2011.
- [12] B. Li and C. Wang, “Comparative analysis on PMSM control system based on SPWM and SVPWM,” in *2016 Chinese Control and Decision Conference (CCDC)*, Yinchuan, China, May 2016, pp. 5071–5075.
- [13] S. Panda, A. Mishra, and B. Srinivas, “Control of Voltage Source Inverters using PWM/SVPWM for Adjustable Speed Drive Applications,” B. Tech Thesis, National Institute of Technology Rourkela, National Institute of Technology, Sector 1, Rourkela, Odisha 769008, India, May 2009. [Online]. Available: <http://ethesis.nitrkl.ac.in/1133/>
- [14] Z. Li, “Space-Vector PWM With TMS320C24x/F24x Using Hardware and Software Determined Switching Patterns,” Mar. 1999, Texas Instruments Application Report SPRA524. [Online]. Available: <http://www.ti.com/lit/an/spra524/spra524.pdf>
- [15] J. Sabarad and G. Kulkarni, “Comparative analysis of SVPWM and SPWM techniques for multilevel inverter,” in *2015 International Conference on Power and Advanced Control Engineering (ICPACE)*, Bangalore, India, Aug. 2015, pp. 232–237.
- [16] S. Mondal, B. Bose, V. Oleschuk, and J. Pinto, “Space vector pulse width modulation of three-level inverter extending operation into overmodulation region,” in *2002 IEEE 33rd Annual IEEE Power Electronics Specialists Conference. Proceedings (Cat. No.02CH37289)*, Cairns, Australia, Jun. 2002, pp. 497–502 Vol.2.
- [17] A. Shaltout and O. Youssef, “Speed control of induction motors using proposed closed loop Volts/hertz control scheme,” in *2017 Nineteenth International Middle East Power Systems Conference (MEPCON)*, Cairo, Egypt, Dec. 2017, pp. 533–537.

- [18] I. Ludtke and M. Jayne, “Direct torque control of induction motors,” in *IEE Colloquium on Vector Control and Direct Torque Control of Induction Motors*, London, United Kingdom, Oct. 1995, pp. 6/1–6/6.
- [19] P. Krause, O. Wasynczuk, and S. Sudhoff, *Analysis of Electric Machinery and Drive Systems*. New York, USA: John Wiley and Sons, Inc., 2002.
- [20] S. Ziegler, R. Woodward, H. Iu, and L. Borle, “Current Sensing Techniques: A Review,” *IEEE Sensors Journal*, vol. 9, pp. 354 – 376, Mar. 2009.
- [21] S. Prakash and T. Hofman, “Clamping Strategies for Belt-Type Continuously Variable Transmissions: An Overview,” in *2017 IEEE Vehicle Power and Propulsion Conference (VPPC)*, Belfort, France, Dec. 2017, pp. 1–6.
- [22] D. Gunji and H. Fujimoto, “Efficiency analysis of powertrain with toroidal continuously variable transmission for Electric Vehicles,” in *IECON 2013 - 39th Annual Conference of the IEEE Industrial Electronics Society*, Belfort, France, Nov. 2013, pp. 6614–6619.
- [23] P. Fajri, R. Ahmadi, and M. Ferdowsi, “Equivalent vehicle rotational inertia used for electric vehicle test bench dynamic studies,” in *IECON 2012 - 38th Annual Conference on IEEE Industrial Electronics Society*, Montreal, Canada, Oct. 2012, pp. 4115–4120.
- [24] United States Environmental Protection Agency, “Vehicle and Fuel Emissions Testing - Dynamometer Drive Schedules,” Oct. 2015, EPA Urban Dynamometer Driving Schedule (UDDS). [Online]. Available: <https://www.epa.gov/vehicle-and-fuel-emissions-testing/dynamometer-drive-schedules>
- [25] M. Pape, “Design of a Flexible and Modular Test Bed for Studies on Islanded Microgrids,” MSc Thesis, University of Waterloo, 200 University Ave West, Waterloo, ON, N2L 3G1, Canada, Sep. 2015. [Online]. Available: <https://uwspace.uwaterloo.ca/handle/10012/9690>
- [26] A. Yazdani and R. Iravani, *Voltage-Sourced Converters in Power Systems : Modeling, Control, and Applications*. New Jersey, United States: John Wiley and Sons, Inc., 2010.
- [27] G. Grandi and J. Loncarski, “Evaluation of current ripple amplitude in three-phase PWM voltage source inverters,” in *2013 International Conference-Workshop Compatibility And Power Electronics*, Ljubljana, Slovenia, Jun. 2013, pp. 156–161.

- [28] M. Vujacic, M. Hammami, M. Srndovic, and G. Grandi, “Evaluation of DC voltage ripple in three-phase PWM voltage source inverters,” in *2017 IEEE 26th International Symposium on Industrial Electronics (ISIE)*, Edinburgh, United Kingdom, Jun. 2017, pp. 711–716.
- [29] N. Mohan, T. Undeland, and W. Robbins, *Power Electronics: Converters, Applications, and Design*. Toronto, Canada: John Wiley and Sons, Inc., 1995.
- [30] R. Krishnan, *Electric Motor Drives: Modeling, Analysis, and Control*. New Jersey, United States: Prentice Hall, 2001.
- [31] R. Lorenz and D. Novotny, “Saturation effects in field-oriented induction machines,” *IEEE Transactions on Industry Applications*, vol. 26, pp. 283–289, Mar. 1990.
- [32] B. Bose, *Modern Power Electronics and AC Drives*. New Jersey, United States: Prentice Hall, 2002.
- [33] N. Semiconductors, “I2C-Bus Specification and User Manual: UM10204,” Apr. 2014. [Online]. Available: <https://www.nxp.com/docs/en/user-guide/UM10204.pdf>
- [34] Magnetics, “Inductor Design with Magnetics Powder Cores,” <https://www.mag-inc.com/design/design-guides/inductor-design-with-magnetics-powder-cores>, accessed on 2016-07-06.
- [35] Micrometals Alloy Powder Cores, A Division of Micrometals Inc, “Micrometals Alloy Powder Cores - Part Number: FS-250026-2,” <https://www.micrometalsarnoldpowdercores.com/pdf/FS-250026-2-DataSheet.pdf>, accessed on 2017-06-06.
- [36] Magnetics, “Inductor Cores: Material and Shape Choices,” <https://www.mag-inc.com/Design/Design-Guides/Inductor-Cores-Material-and-Shape-Choices>, accessed on 2016-07-14.
- [37] N. Vazquez, H. Lopez, C. Hernandez, R. Osorio, E. Rodriguez, and J. Arau, “A Six-switch Three-Level Current Source Inverter,” in *12th IEEE International Power Electronics Congress*, San Luis Potosi, Mexico, Aug. 2010, pp. 145–148.



# APPENDICES

# Appendix A

## Inductor Core Windings

### A.1 AC/DC Inductor Core Winding

The design of the inductor for the AC side follows the following formulas from the Magnetics website [34]. The design is based around the Micrometals FS-250026-2 core where the datasheet is found on the Micro Metals Arnold Powder Cores website [35].

The parameters for this core and design are as follows:

- $A_{L,nominal} = 89nH/N^2$  (Inductance Factor)
- $A_{L,tolerance} = +/- 8\%$  (Inductance Factor Tolerance)
- $L_e = 14.314cm$  (Effective Magnetic Path Length)
- $V_e = 55.8cm^3$  (Effective Core Volume)
- $ID = 30.48mm$  (Core Minimum Inner Diameter)
- $I_{rms} = 16.67A$  (System RMS Current)
- $I_{ripple,pp} = 30\%$  (Maximum Current Ripple Percentage Allowance)
- $L_{design} = 1.01mH$  (Inductor Inductance Design Specification)
- $D_{11AWG} = 2.39mm$  (11 AWG Wire Diameter)

The specifications for the filter design are as follows:

- Maximum current at the motor fundamental frequency is 20A.
- Current ripple at the 20kHz switching frequency is 20% peak to peak.

Based on prior calculations, it was found that two cores stacked together are needed to meet the design specification and the steps will be simplified to include the core stacking.

The first step is to obtain the number of wire turns needed at no load using the minimum inductance factor shown in equation (A.1).

$$N_{NL} = \sqrt{\frac{L_{design} (nH)}{A_{L,min} \times \# \text{ of cores}}} = \sqrt{\frac{1.01 \times 10^6}{81.88 \times 2}} = 79 \text{ turns} \quad (\text{A.1})$$

The next step is to calculate the DC bias in  $AT/cm$  given by (A.2).

$$H_{first} = 0.4\pi \frac{N_{NL} I_{rms}}{L_e} = 0.4\pi \frac{79 \times 16.67}{14.314} = 114.93 AT/cm \quad (\text{A.2})$$

The initial permeability can be obtained from the manufacturer datasheet under saturation effect, which indicates 92% at the calculated DC bias level.

One can find the number of turns at full load using (A.3) where  $\mu$  is the initial permeability.

$$N_{FL} = N_{NL} \div \mu = 79 \div 0.92 = 86 \text{ turns} \quad (\text{A.3})$$

The DC Bias must be recalculated to account for the increased number of turns.

$$H_{second} = 0.4\pi \frac{N_{FL} I_{rms}}{L_e} = 0.4\pi \frac{86 \times 16.67}{14.314} = 124.9 AT/cm \quad (\text{A.4})$$

Re-examining the datasheet, one can find the initial permeability to be approximately 91% under full load.

The new effective inductance factor can be found using the following equation:

$$A_{L,effective} = A_{L,min} \times \mu = 81.88 \times 2 \times 0.91 = 149.0 nH/T^2 \quad (\text{A.5})$$

The final inductance value of the inductors can now be calculated under both no-load and full-load conditions as follows.

$$L_{NL} = \frac{N_{FL}^2 \times A_{L,min} \times \# \text{ of cores}}{10^6} = \frac{86^2 \times 81.88 \times 2}{10^6} = 1.211mH \quad (A.6)$$

$$L_{FL} = \frac{N_{FL}^2 \times A_{L,effective} \times \# \text{ of cores}}{10^6} = \frac{86^2 \times 74.51 \times 2}{10^6} = 1.102mH \quad (A.7)$$

Utilizing 11 AWG magnet wire, a maximum number of 123 windings can fit inside the inner diameter of the core with each wire strand having a diameter of 2.39mm. To obtain the inductance specification, 86 turns are required which can be achieved. The final inductance of 1.21mH is measured under no load on the final core.

The losses of the inductor can also be found. The core loss can be found according to (A.8) from the inductor core datasheet.

$$CoreLoss = \frac{f}{\frac{a}{Bpk^3} + \frac{b}{Bpk^{2.3}} + \frac{c}{Bpk^{1.65}}} + d \times Bpk^2 \times f^2 \times V_e = 1.896W \quad (A.8)$$

where

$$a = 1.00E+6$$

$$b = 1.812E+8$$

$$c = 3.251E+6$$

$$d = 6.158E-14$$

$$Bpk = 300 \text{ Gauss}$$

$$f = 20000 \text{ Hz}$$

The wire losses can be found according to (A.9).

$$WireLoss = l_{wire} \times N_{FL} \times \rho \times I_{rms}^2 = 0.129 \frac{m}{turn} \times 86turns \times 0.00413 \frac{\Omega}{m} \times 16.67A^2 = 12.73W \quad (A.9)$$

In (A.9),  $l_{wire}$  is the length of wire required to make one complete turn around the core,  $N_{FL}$  number of turns around the core,  $\rho$  resistivity of the wire is 0.00413, and  $I_{rms}$  RMS current in the inductor.

The total power loss of each inductor under full load is 14.626W resulting in a temperature rise of 45.38 degrees Celsius using the equation for temperature rise found on

Magnetics website [36]. The temperature rise and power loss are acceptable under full load.

## A.2 DC/DC Inductor Core Winding

The design of the inductor for the DC/DC converter follows the same formulas as those shown in the AC/DC Inductor design in A.1. The design will be shown for the specifications of the DC/DC converter utilizing the Micrometals FS-250026-2 found on the Micro Metals Arnold Powder Cores website as used in the AC/DC design [35].

The parameters for this core and design are as follows:

- $A_{L,nominal} = 89nH/N^2$  (Inductance Factor)
- $A_{L,tolerance} = +/- 8\%$  (Inductance Factor Tolerance)
- $L_e = 14.314cm$  (Effective Magnetic Path Length)
- $V_e = 55.8cm^3$  (Effective Core Volume)
- $ID = 30.48mm$  (Core Minimum Inner Diameter)
- $I_{pk} = 60A$  (Peak Current)
- $I_{ripple} = 15\%$  (Percent of Continuous Current)
- $L_{design} = 442\mu H$  (Inductor Inductance Design Specification)
- $D_{11AWG} = 25\%$  (Percent of Continuous Current)

The specifications for the filter design are as follows:

- Maximum current at the motor fundamental frequency is 60A.
- Current ripple at the 20kHz switching frequency is 9A peak to peak.

Based on prior calculations, it was found that three cores stacked together are needed to meet the design specification and the steps will be simplified to include the core stacking.

The first step is to obtain the number of wire turns needed at no load - as shown in equation (A.10).

$$N_{NL} = \sqrt{\frac{L_{design} (nH)}{A_{L,min} \times \# \text{ of cores}}} = \sqrt{\frac{0.442 \times 10^6}{81.88 \times 2}} = 39 \text{ turns} \quad (\text{A.10})$$

The next step is to calculate the DC bias in  $AT/cm$  given by (A.11).

$$H_{first} = 0.4\pi \frac{N_{NL}I}{L_e} = 0.4\pi \frac{39 \times 60}{14.314} = 205.57 AT/cm \quad (\text{A.11})$$

The initial permeability can be obtained from the manufacturer datasheet under saturation effect, which indicates 81% at the calculated DC bias level.

One can find the number of turns at full load using (A.12) where  $\mu$  is the initial permeability.

$$N_{FL} = N_{NL} \div \mu = 39 \div 0.81 = 48 \text{ turns} \quad (\text{A.12})$$

The DC Bias must be recalculated to account for the increased number of turns.

$$H_{second} = 0.4\pi \frac{N_{FL}I}{L_e} = 0.4\pi \frac{48 \times 60}{14.314} = 253.8 AT/cm \quad (\text{A.13})$$

Re-examining the datasheet, one can find the initial permeability to be approximately 77% under full load.

The new effective inductance factor can be found using the following equation:

$$A_{L,effective} = A_{L,min} \times \mu = 81.88 \times 0.77 = 63.0 nH/T^2 \quad (\text{A.14})$$

The final inductance value of the inductors can now be calculated under both no-load and full-load conditions.

$$L_{NL} = \frac{N_{FL}^2 \times A_{L,min} \times \# \text{ of cores}}{10^6} = \frac{48^2 \times 81.88 \times 3}{10^6} = 0.566 mH \quad (\text{A.15})$$

$$L_{FL} = \frac{N_{FL}^2 \times A_{L,effective} \times \# \text{ of cores}}{10^6} = \frac{48^2 \times 63.0 \times 3}{10^6} = 0.435 mH \quad (\text{A.16})$$

Utilizing 11 AWG magnet wire, a maximum number of 123 windings can fit inside the inner diameter of the core with each wire strand having a diameter of 2.39mm. To obtain

the inductance specification, 48 turns are required with two wires in parallel. The final inductance of 0.560mH is measured under no load on the final core.

The losses of the inductor can also be found. The core loss can be found according to equation (A.17) from the inductor core datasheet.

$$CoreLoss = \frac{f}{\frac{a}{Bpk^3} + \frac{b}{Bpk^{2.3}} + \frac{c}{Bpk^{1.65}}} + d \times Bpk^2 \times f^2 \times V_e = 3.088W \quad (A.17)$$

where

$$a = 1.00E+6$$

$$b = 1.812E+8$$

$$c = 3.251E+6$$

$$d = 6.158E-14$$

$$Bpk = 300 \text{ Gauss}$$

$$f = 20000 \text{ Hz}$$

The wire losses can be found according to (A.18).

$$WireLoss = l_{wire} \times N_{FL} \times \rho \times I^2 = 0.182 \frac{m}{turn} \times 48turns \times 0.00206 \frac{\Omega}{m} \times 60A^2 = 64.79W \quad (A.18)$$

In (A.18),  $l_{wire}$  is the length of wire required to make one complete turn around the cores,  $N_{FL}$  number of turns around the core,  $\rho$  resistivity of the wire is 0.00206 for two wires in parallel, and  $I$  RMS current in the inductor.

The total power loss of each inductor under full load is 67.87W resulting in a temperature rise of 91.93 degrees Celsius using the equation for temperature rise found on Magnetics website [36]. The temperature rise and power loss are acceptable under full load.

# Appendix B

## Main Controller Code

### B.1 AC/DC Controller Code

The main controller code for the AC/DC converter is given below.

```
void AcDcController::computeStep_Notification(void *context,
    ↪ MeasDataStorage* data)
{
    AcDcController *me = static_cast<AcDcController*>(context);
    float vDc, V0;
    static DQOFrame curRef;
    PWMTriggerDQOSubscriptionData pwmData;

    if (me->enabled)
    {
        //Perform a control loop iteration

        //Limit the output voltage
        V0 = ControllerOperationalSettings::getV0();

        if (V0 > ControllerParameterSettings::getVDcMax())
        {
            vDc = ControllerParameterSettings::getVDcMax();
        }
        else if (V0 < ControllerParameterSettings::getVDcMin())
```



```

    {
        vDc = ControllerParameterSettings::getVDcMin();
    }
    else
    {
        vDc = V0;
    }

    //PI Controller: Vdc error to current reference
    //Quadrature axis reference is always zero
    curRef.d = me->voltController.computeStep(vDc - data->Vdc,
        ↪ 0.0);

    //PI Controller: Current error to PWM voltages
    pwmData.commandVoltages = me->currentController.computeStep
        ↪ (&curRef, &data->curLdq);

    //Synchronize theta for DQ-ABC and ABC-DQ block
    pwmData.theta = adcController.measDataStorage.theta;
    pwmData.vDc = 1.0;

    //Send to PWM module to switch gates
    me->pwmTriggerDQOEvent.notifyAll(&pwmData);
}
}

```

## B.2 DC/DC Controller Code

The main controller code for the DC/DC converter is given below.

```

void DcDcController::computeStep_Notification(void *context,
    ↪ MeasDataStorage* data)
{
    DcDcController *me = static_cast<DcDcController*>(context);
    float vDc, V0;
    static ABCFrame curRef;
    PWMTriggerABCSubscriptionData pwmData;

```

```

if (me->enabled)
{
    //Perform a control loop iteration for Controller 1 & 2

    //Limit the output voltage
    V0 = ControllerOperationalSettings::getV0(); //V0 is
        ↪ reference for both DC Voltage rails

    //Vdc is on the high side of DC max
    if ((V0 > ControllerParameterSettings::getVDC_a_Max()) || (
        ↪ V0 > ControllerParameterSettings::getVDC_b_Max()))
    {
        if (V0 > ControllerParameterSettings::getVDC_a_Max())
        {
            vDc= ControllerParameterSettings::
                ↪ getVDC_a_Max();
        }
        else //V0 is larger than Vdc_b max
        {
            vDc= ControllerParameterSettings::
                ↪ getVDC_b_Max();
        }
    }
    //Vdc is on the low side of DC min
    else if ((V0 < ControllerParameterSettings::getVDC_a_Min())
        ↪ || (V0 < ControllerParameterSettings::getVDC_b_Min())
        ↪ )
    {
        if (V0 < ControllerParameterSettings::getVDC_a_Min())
        {
            vDc = ControllerParameterSettings::
                ↪ getVDC_a_Min();
        }
        else //Vo is smaller than Vdc_b min
        {
            vDc = ControllerParameterSettings::
                ↪ getVDC_b_Min();
        }
    }
}

```

```

        }
    }
    //catch any other edge cases
    else
    {
        vDc = V0;
    }

    //PI Controller: Vdc error to current reference
    curRef.a = me->voltController_a.computeStep(vDc - data->
        ↪ Vdc_a, 0.0);
    curRef.b = me->voltController_b.computeStep(vDc - data->
        ↪ Vdc_b, 0.0);

    //Negate results because current sensor is backwards
    curRef.a = -curRef.a;
    curRef.b = -curRef.b;

    //PI Controller: Current error to PWM voltages
    pwmData.commandVoltages.a = me->dcCurrentController_a.
        ↪ computeStep(curRef.a - data->idc_a, 0.0);
    pwmData.commandVoltages.b = me->dcCurrentController_b.
        ↪ computeStep(curRef.b - data->idc_b, 0.0);

    pwmData.vDc = 1.0;

    //Send to PWM module to switch gates
    me->pwmTriggerABCEvent.notifyAll(&pwmData);
}
}

```

### B.3 DC/AC Speed Controller Code

The main controller code for the DC/AC Speed controller is given below.

```

void MotorController::computeStep_Notification(void *context,
    ↪ MeasDataStorage *data)

```

```
{
```

```
MotorController *me = static_cast<MotorController*>(context);  
float V0, temp;  
DQOFrame curRef, decouplingRef;  
PWMTriggerDQOSubscriptionData pwmData;  
  
if (me->enabled)  
{  
    //Limit the speed  
    V0 = ControllerOperationalSettings::getV0();  
  
    if (V0 > ControllerParameterSettings::getRpmSpeedMax())  
    {  
        rpmSpeedRef = ControllerParameterSettings::  
            ↪ getRpmSpeedMax();  
    }  
    else if (V0 < ControllerParameterSettings::getRpmSpeedMin())  
    {  
        rpmSpeedRef = ControllerParameterSettings::  
            ↪ getRpmSpeedMin();  
    }  
    else  
    {  
        rpmSpeedRef = V0;  
    }  
  
    //-----  
    ↪  
    //Ramp - Speed Limiter  
    //Set to 1000rpm per 1second to control instantaneous torque  
    //-----  
    ↪  
    temp = (rpmSpeedRef - rpmSpeed);  
  
    if (fabs(temp) >= speedRampStepSize)  
    {  
        if (rpmSpeedRef >= rpmSpeed)
```

```

        {
            rpmSpeed += speedRampStepSize;
        }
        else
        {
            rpmSpeed -= speedRampStepSize;
        }
    }
    else
    {
        rpmSpeed = rpmSpeedRef;
    }

//Set torque (quadrature axis) to zero when motor is stopped
    ↪ for over 25ms
if ((fabs(rpmSpeed) <= 0.1) && ((fabs(fabs(rpmSpeed)-fabs(
    ↪ qepController.speedRPM))) <= 2))
{
    if (motorFieldCounter >= motorFieldHoldTime)
    {
        curRef.q = 0;
    }
    else
    {
        motorFieldCounter++;
        curRef.q = me->speedController.computeStep(
            ↪ rpmSpeed - qepController.speedRPM, 0.0)
            ↪ ;
    }
}
else
{
    motorFieldCounter = 0;
    curRef.q = me->speedController.computeStep(rpmSpeed -
        ↪ qepController.speedRPM, 0.0);
}

//Compute Field Weakening and Limit Id Reference Current

```

```

maxTorque = MOTORCTRL_MAX_POWER/(qepController.speedRPM*2*PI
    ↪ /60);
maxCurRefd = fabs((maxTorque*4*MOTORCTRL_DEFAULT_LR)/(3*
    ↪ MOTORCTRL_DEFAULT_POLES*MOTORCTRL_DEFAULT_LM*
    ↪ MOTORCTRL_DEFAULT_LM*MOTORCTRL_RATED_IQ));

if (fabs(qepController.speedRPM) >= MOTORCTRL_BASE_SPEED)
{
    if (duty_d >= maxCurRefd)
    {
        curRef.d = maxCurRefd;
    }
    else
    {
        curRef.d = fabs(duty_d);
    }
}
else
{
    curRef.d = fabs(duty_d);
}

//Limit D-Axis Current to Hardware Maximum as Secondary
    ↪ Safety
if (curRef.d >= MOTORCTRL_RATED_ID)
{
    curRef.d = MOTORCTRL_RATED_ID;
}
if (curRef.d < 0.0) //Check for negative direct axis current
    ↪ reference
{
    curRef.d = 0.0;
}

//Compute Slip, Theta, and Decoupling
qepController.QEPCalculation(curRef.d, curRef.q);
torque.calculateTorque(curRef.d, data->curLdq.q);

```

```

    decoupling.calculateDecoupling(data->curLdq.d, data->curLdq.
        ↪ q);

    //Compute Speed
    qepController.QEPSpeedCalculation(rpmSpeed);

    //Assign local variable to decoupling computation
    decouplingRef.d = decoupling.vdsDecouple;
    decouplingRef.q = decoupling.vqsDecouple;

    pwmData.commandVoltages = me->currentController.computeStep
        ↪ (&curRef, &data->curLdq, &decouplingRef);

    //Update omega (w) and theta for next iteration
    data->w = qepController.elecSpeedRadAvg;
    data->theta = qepController.theta;

    //Calculate new theta
    pwmData.theta = adcController.measDataStorage.theta;
    pwmData.vDc = 1.0;

    //Call DQ0 to ABC SVPWM method
    me->pwmTriggerDQOEvent.notifyAll(&pwmData);
}
}

```

## B.4 DC/AC Torque Controller Code

The main controller code for the DC/AC Torque controller is given below.

```

void MotorController::computeStep_Notification(void *context,
    ↪ MeasDataStorage *data)
{
    MotorController *me = static_cast<MotorController*>(context);
    float V0, temp;
    DQOFrame curRef, decouplingRef;
    PWMTriggerDQOSubscriptionData pwmData;

```

```

if (me->enabled)
{
    //Limit the torque
    V0 = ControllerOperationalSettings::getV0();

    if (V0 > ControllerParameterSettings::getNmTorqueMax())
    {
        nmTorqueRef = ControllerParameterSettings::
            ↪ getNmTorqueMax();
    }
    else if (V0 < ControllerParameterSettings::getNmTorqueMin())
    {
        nmTorqueRef = ControllerParameterSettings::
            ↪ getNmTorqueMin();
    }
    else
    {
        nmTorqueRef = V0;
    }

    //-----
    ↪
    //Ramp - Torque Limiter
    //Set to 7Nm per 1second so speed can react
    //-----
    ↪
    temp = (nmTorqueRef - nmTorque);

    if (fabs(temp) >= torqueRampStepSize)
    {
        if (nmTorqueRef >= nmTorque)
        {
            nmTorque += torqueRampStepSize;
        }
        else
        {
            nmTorque -= torqueRampStepSize;
        }
    }
}

```



```

    }
}
else
{
    nmTorque = nmTorqueRef;
}

//Limit Feedback Torque
if (motorTorqueFeedback > ControllerParameterSettings::
    ↪ getNmTorqueMax())
{
    motorTorqueFeedback = ControllerParameterSettings::
        ↪ getNmTorqueMax();
}
else if (motorTorqueFeedback < ControllerParameterSettings::
    ↪ getNmTorqueMin())
{
    motorTorqueFeedback = ControllerParameterSettings::
        ↪ getNmTorqueMin();
}

//Set torque (quadrature axis) to zero when motor is stopped
    ↪ for over 25ms
if ((fabs(nmTorque) <= 0.01) && ((fabs(fabs(nmTorque)-fabs(
    ↪ nmTorqueFB))) <= 0.2) && (fabs(qepController.speedRPM
    ↪ ) <= 2))
{
    if (motorFieldCounter >= motorFieldHoldTime)
    {
        curRef.q = 0;
    }
    else
    {
        motorFieldCounter++;
        curRef.q = me->torqueController.computeStep(
            ↪ motorTorqueFeedback - nmTorque, 0.0);
    }
}
}

```

```

else
{
    motorFieldCounter = 0;
    curRef.q = me->torqueController.computeStep(
        ↪ motorTorqueFeedback - nmTorque, 0.0);
}

//Compute Field Weakening and Limit Id Reference Current
maxTorque = MOTORCTRL_MAX_POWER/(qepController.speedRPM*2*PI
    ↪ /60);
maxCurRefd = fabs((maxTorque*4*MOTORCTRL_DEFAULT_LR)/(3*
    ↪ MOTORCTRL_DEFAULT_POLES*MOTORCTRL_DEFAULT_LM*
    ↪ MOTORCTRL_DEFAULT_LM*MOTORCTRL_RATED_IQ));

if (fabs(qepController.speedRPM) >= MOTORCTRL_BASE_SPEED)
{
    if (duty_d >= maxCurRefd)
    {
        curRef.d = maxCurRefd;
    }
    else
    {
        curRef.d = fabs(duty_d);
    }
}
else
{
    curRef.d = fabs(duty_d);
}

//Limit D-Axis Current to Hardware Maximum as Secondary
    ↪ Safety
if (curRef.d >= MOTORCTRL_RATED_ID)
{
    curRef.d = MOTORCTRL_RATED_ID;
}
if (curRef.d < 0.0) //Check for negative direct axis current
    ↪ reference

```

```

    {
        curRef.d = 0.0;
    }

    //Compute Slip, Theta, and Decoupling
    qepController.QEPCalculation(curRef.d, curRef.q);
    torque.calculateTorque(data->curLdq.d, data->curLdq.q);
    decoupling.calculateDecoupling(data->curLdq.d, data->curLdq.
        ↪ q);

    //Compute Speed
    qepController.QEPSpeedCalculation(rpmSpeed);

    //Assign local variable to decoupling computation
    decouplingRef.d = decoupling.vdsDecouple;
    decouplingRef.q = decoupling.vqsDecouple;

    pwmData.commandVoltages = me->currentController.computeStep
        ↪ (&curRef, &data->curLdq, &decouplingRef);

    //Update omega (w) and theta for next iteration
    data->w = qepController.elecSpeedRadAvg;
    data->theta = qepController.theta;

    //Calculate new theta
    pwmData.theta = adcController.measDataStorage.theta;
    pwmData.vDc = 1.0;

    //Call DQ0 to ABC SVPWM method
    me->pwmTriggerDQOEvent.notifyAll(&pwmData);
}
}

```

# Appendix C

## Sensor Design and BOM

### C.1 Sensor Design Schematic

The AC Voltage and Current sensing PCB schematic can be seen in Figure C.1. It is a multi-function board that can be configured based on the Bill of Materials (BOM) to sense current or voltage but not both simultaneously.

From the schematic, the sensed AC current can be converted to a voltage that can be read by the microcontroller. The calculation for the sensing circuitry is given by (C.1) where  $12$  is the bias voltage,  $I_{in}$  current flowing through the hall sensor,  $N_{trans}$  hall effect sensor transformer turns ratio,  $V_{out}$  output voltage of the sensor, and all other parameters are as seen in the schematic.

$$V_{out} = \frac{(12R_1R_2 - [\frac{I_{in}}{N_{trans}}]R_mR_2R_3)}{R_1R_3} \quad (C.1)$$

The same schematic can be used to convert the AC side voltage to a voltage that can be read by the microcontroller. The calculation for the sensing circuitry is given by (C.2), where  $12$  is the bias voltage,  $V_{in}$  high side voltage,  $N_{trans}$  hall effect sensor transformer turns ratio,  $V_{out}$  output voltage of the sensor, and all other parameters are as seen in the schematic.

$$V_{out} = \frac{(12R_1R_2 - [\frac{V_{in}N_{trans}}{R_{sens}}]R_mR_2R_3)}{R_1R_3} \quad (C.2)$$

The DC Voltage and Current sensing PCB schematic can be seen in Figure C.2.

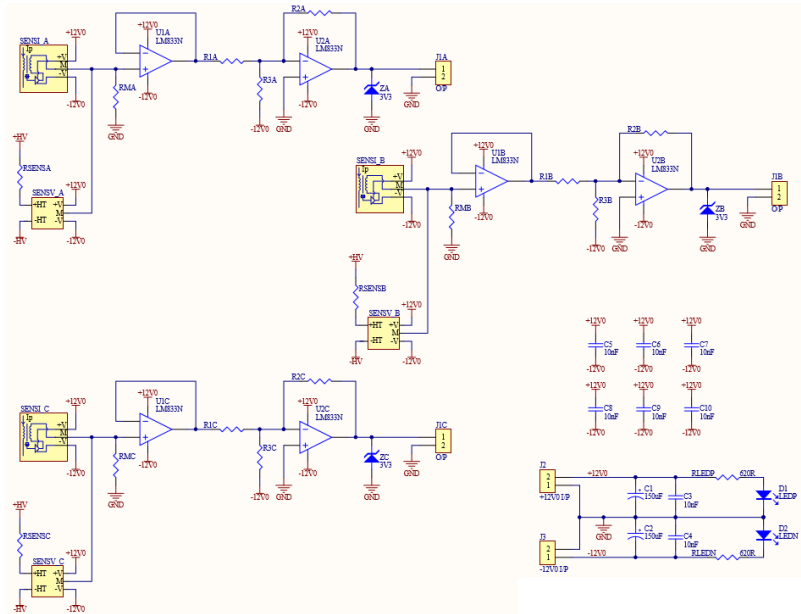


Figure C.1: AC Voltage and Current Sensor Schematic

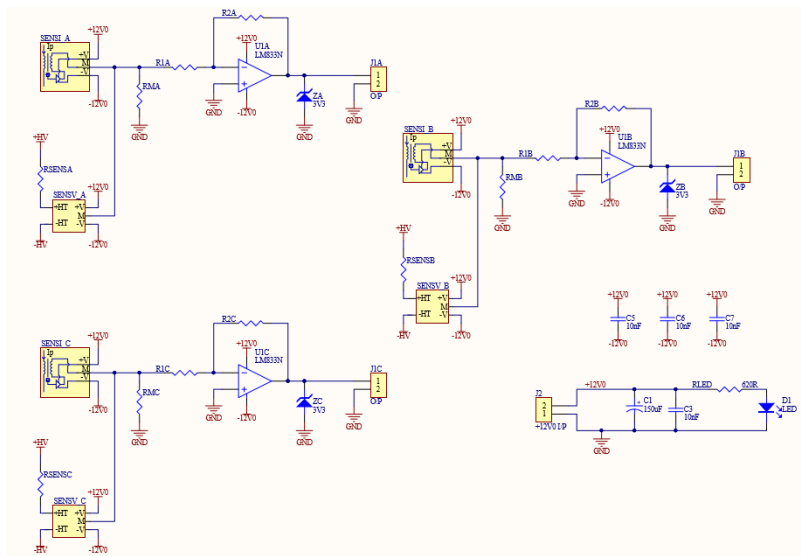


Figure C.2: DC Voltage and Current Sensor Schematic

From the schematic, the sensed DC current can be converted to a voltage that can be read by the microcontroller. The calculation for the sensing circuitry is given by (C.3) where

$I_{in}$  is the current flowing through the hall sensor,  $N_{trans}$  the hall effect sensor transformer turns ratio,  $V_{out}$  the output voltage of the sensor, and all other parameters are as seen in the schematic. Only one opamp stage is used and due to the inverting nature of the connection, the current flow is required to go in the negative direction of the hall effect sensor.

$$V_{out} = \left[ \frac{I_{in}}{N_{trans}} R_m \right] \frac{R_2}{R_1} \quad (C.3)$$

The same schematic can be used to obtain the AC side voltage shown in (C.4), where  $V_{in}$  is the high side voltage,  $N_{trans}$  the hall effect sensor transformer windings,  $V_{out}$  the output voltage of the sensor, and all other parameters are as seen in the schematic. Only one opamp stage is used and due to the inverting nature of the connection, the positive and negative voltage connections on the input side are swapped at the input terminals of the hall effect sensor.

$$V_{out} = \left[ \frac{V_{in}}{R_{sens}} N_{trans} R_m \right] \frac{R_2}{R_1} \quad (C.4)$$

## C.2 AC/DC Module Sensor BOM

Table C.1: AC/DC Module, AC Current Sensor BOM

Parameter	Value	Schematic Reference
Current Sensor	LEM LA 55-P	SENSI_A, SENSI_B, SENSI_C
Resistor	37R4, 0.5W, 1%	RMA, RMB, RMC
Resistor	1K00, 0.25W, 0.1%	R3A, R3B, R3C
Resistor	8K02, 0.25W, 0.1%	R5A, R5B, R5C
Resistor	1K00, 0.25W, 0.1%	R4A, R4B, R4C
Resistor	620R, 0.1W, 1%	RLEDP, RLEDN
LED	Green LED, Vf=2.2V	LEDP, LEDN
Opamp	Texas Instruments LM833N	U1, U2, U3
Zener Diode	Vz=3V3, 0.4W	ZA, ZB, ZC
Capacitor	10nF, 50V, X7R	C3-C10
Capacitor	150 $\mu$ F, 35V, Aluminum	C1-C2
Terminal Block	2 Position, 5mm Pitch	J3A, J3B, J3C

Table C.2: AC/DC Module, AC Voltage Sensor BOM

Parameter	Value	Schematic Reference
Voltage Sensor	LEM LV 20-P	SENSV_A, SENSV_B, SENSV_C
Resistor	15K0, 5W, 1%	RSENSA, RSENSB, RSENSC
Resistor	43R0, 0.25W, 1%	RMA, RMB, RMC
Resistor	3K30, 0.25W, 0.1%	R3A, R3B, R3C
Resistor	10K0, 0.25W, 0.1%	R5A, R5B, R5C
Resistor	1K00, 0.25W, 0.1%	R4A, R4B, R4C
Resistor	620R, 0.1W, 1%	RLEDP, RLEDN
LED	Green LED, Vf=2.2V	LEDP, LEDN
Opamp	Texas Instruments LM833N	U1, U2, U3
Zener Diode	Vz=3V3, 0.4W	ZA, ZB, ZC
Capacitor	10nF, 50V, X7R	C3-C10
Capacitor	150 $\mu$ F, 35V, Aluminum	C1-C2
Terminal Block	2 Position, 5mm Pitch	J3A, J3B, J3C

Table C.3: AC/DC Module, DC Voltage Sensor BOM

Parameter	Value	Schematic Reference
Voltage Sensor	LEM LV 20-P	SENSV
Resistor	39K0, 10W, 1%	RSENS
Resistor	84R5, 0.50W, 1%	RM
Resistor	1K00, 0.25W, 0.1%	R3
Resistor	1K00, 0.25W, 0.1%	R4
Resistor	620R, 0.1W, 1%	RLED
LED	Green LED, Vf=2.2V	LED
Opamp	Texas Instruments LM833N	U1
Zener Diode	Vz=3V3, 0.4W	ZA
Capacitor	10nF, 50V, X7R	C3-C5
Capacitor	150 $\mu$ F, 35V, Aluminum	C1
Terminal Block	2 Position, 5mm Pitch	J3



### C.3 DC/DC Module Sensor BOM

Table C.4: DC/DC Module, DC Current Sensor BOM

Parameter	Value	Schematic Reference
Voltage Sensor	LEM LA 150-P	SENSI
Resistor	20R0, 0.50W, 1%	RM
Resistor	1K00, 0.25W, 0.1%	R3
Resistor	1K00, 0.25W, 0.1%	R4
Resistor	620R, 0.1W, 1%	RLED
LED	Green LED, Vf=2.2V	LED
Opamp	Texas Instruments LM833N	U1
Zener Diode	Vz=3V3, 0.4W	ZA
Capacitor	10nF, 50V, X7R	C3-C5
Capacitor	150 $\mu$ F, 35V, Aluminum	C1
Terminal Block	2 Position, 5mm Pitch	J3

Table C.5: DC/DC Module, DC Voltage Sensor BOM

Parameter	Value	Schematic Reference
Voltage Sensor	LEM LV 20-P	SENSV
Resistor	15K0, 5W, 1%	RSENS
Resistor	120R, 0.50W, 1%	RM
Resistor	1K00, 0.25W, 0.1%	R3
Resistor	1K00, 0.25W, 0.1%	R4
Resistor	620R, 0.1W, 1%	RLED
LED	Green LED, Vf=2.2V	LED
Opamp	Texas Instruments LM833N	U1
Zener Diode	Vz=3V3, 0.4W	ZA
Capacitor	10nF, 50V, X7R	C3-C5
Capacitor	150 $\mu$ F, 35V, Aluminum	C1
Terminal Block	2 Position, 5mm Pitch	J3

## C.4 DC/AC Module Sensor BOM

Table C.6: DC/AC Module, AC Current Sensor BOM

Parameter	Value	Schematic Reference
Current Sensor	LEM LA 150-P	SENSI_A, SENSI_B, SENSI_C
Resistor	20R0, 0.5W, 1%	RMA, RMB, RMC
Resistor	1K00, 0.25W, 0.1%	R3A, R3B, R3C
Resistor	8K02, 0.25W, 0.1%	R5A, R5B, R5C
Resistor	1K00, 0.25W, 0.1%	R4A, R4B, R4C
Resistor	620R, 0.1W, 1%	RLEDP, RLEDN
LED	Green LED, Vf=2.2V	LEDP, LEDN
Opamp	Texas Instruments LM833N	U1, U2, U3
Zener Diode	Vz=3V3, 0.4W	ZA, ZB, ZC
Capacitor	10nF, 50V, X7R	C3-C10
Capacitor	150 $\mu$ F, 35V, Aluminum	C1-C2
Terminal Block	2 Position, 5mm Pitch	J3A, J3B, J3C

Table C.7: DC/AC Module, AC Voltage Sensor BOM

Parameter	Value	Schematic Reference
Current Sensor	LEM LV 20-P	SENSV_A, SENSV_B, SENSV_C
Resistor	10K0, 5W, 1%	RSENSA, RSENSB, RSENS
Resistor	56R0, 0.5W, 1%	RMA, RMB, RMC
Resistor	1K00, 0.25W, 0.1%	R3A, R3B, R3C
Resistor	8K02, 0.25W, 0.1%	R5A, R5B, R5C
Resistor	1K00, 0.25W, 0.1%	R4A, R4B, R4C
Resistor	620R, 0.1W, 1%	RLEDP, RLEDN
LED	Green LED, Vf=2.2V	LEDP, LEDN
Opamp	Texas Instruments LM833N	U1, U2, U3
Zener Diode	Vz=3V3, 0.4W	ZA, ZB, ZC
Capacitor	10nF, 50V, X7R	C3-C10
Capacitor	150 $\mu$ F, 35V, Aluminum	C1-C2
Terminal Block	2 Position, 5mm Pitch	J3A, J3B, J3C

# Appendix D

## Induction Machine Derivations

### D.1 Slip and Torque Derivation

The induction motor circuit can be represented in the  $d^e$  and  $q^e$  axes frame by the schematics shown in Figure D.1. The quadrature axis schematic is shown in Figure D.1(a) and the direct axis schematic is shown in Figure D.1(b).

From Figure D.1, the motor voltage equations can be derived and are shown in (D.1)-(D.4).

$$v_{qs} = R_s i_{qs} + \omega_e \lambda_{ds} + \frac{d}{dt} \lambda_{qs} \quad (\text{D.1})$$

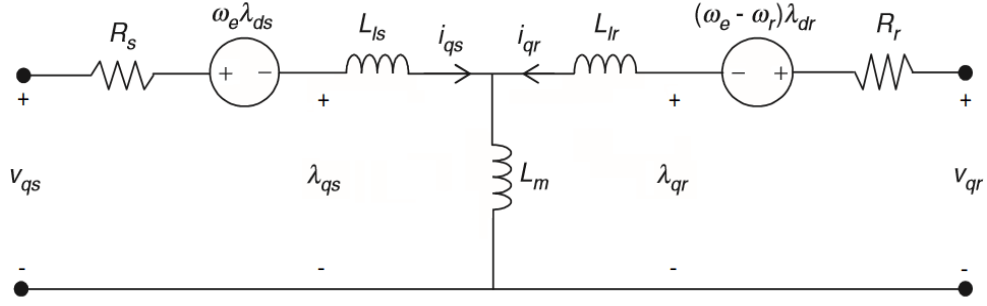
$$v_{ds} = R_s i_{ds} - \omega_e \lambda_{qs} + \frac{d}{dt} \lambda_{ds} \quad (\text{D.2})$$

$$v_{qr} = R_r i_{qr} + (\omega_e - \omega_r) \lambda_{dr} + \frac{d}{dt} \lambda_{qr} \quad (\text{D.3})$$

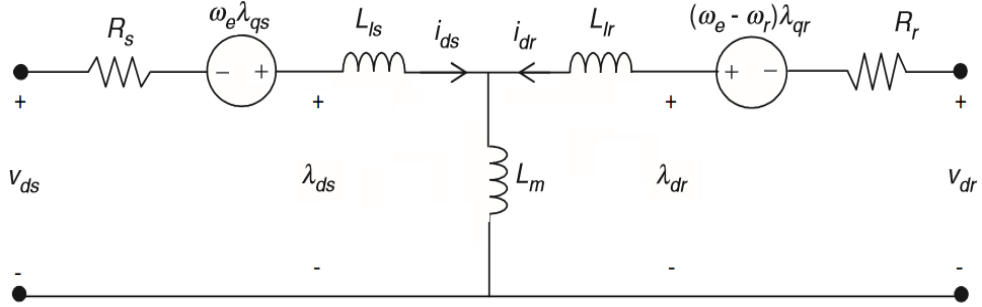
$$v_{dr} = R_r i_{dr} - (\omega_e - \omega_r) \lambda_{qr} + \frac{d}{dt} \lambda_{dr} \quad (\text{D.4})$$

Furthermore, the flux linkages can be expressed by (D.5)-(D.8).

$$\lambda_{qs} = L_s i_{qs} + L_m i_{qr} \quad (\text{D.5})$$



(a) Induction Machine Q-Axis Schematic



(b) Induction Machine D-Axis Schematic

Figure D.1: Synchronously Rotating Reference Frame Motor Schematics [11]

$$\lambda_{ds} = L_s i_{ds} + L_m i_{dr} \quad (\text{D.6})$$

$$\lambda_{qr} = L_r i_{qr} + L_m i_{qs} \quad (\text{D.7})$$

$$\lambda_{dr} = L_r i_{dr} + L_m i_{ds} \quad (\text{D.8})$$

Incorporating (D.5)-(D.8) into (D.1)-(D.4) results in the matrix shown in (D.9) [11].

$$\begin{bmatrix} v_{qs} \\ v_{ds} \\ v_{qr} \\ v_{dr} \end{bmatrix} = \begin{bmatrix} R_s + sL_s & w_e L_s & sL_m & w_e L_m \\ -w_e L_s & R_s + sL_s & w_e L_m & sL_m \\ sL_m & (w_e - w_r)L_m & R_r + sL_r & (w_e - w_r)L_r \\ -(w_e - w_r)L_m & sL_m & -(w_e - w_r)L_r & R_r + sL_r \end{bmatrix} \begin{bmatrix} i_{qs} \\ i_{ds} \\ i_{qr} \\ i_{dr} \end{bmatrix} \quad (\text{D.9})$$

In Figure D.1, motor voltage equations (D.1)-(D.4), flux linkages (D.5)-(D.8), and matrix relation (D.9), the parameters are expressed as follows:  $v$  is the motor voltage,  $i$  the motor current,  $\omega$  the angular speed,  $R$  the resistance,  $\lambda$  the flux linkage,  $s$  and  $d/dt$  the differential operators, and subscripts  $q$ ,  $d$ ,  $s$ ,  $r$ ,  $m$ , and  $e$  representing the quadrature axis, direct axis, stator, rotor, magnetization, and electrical reference frame.

IFOC can be easily implemented in the synchronously rotating reference frame, also known as the magnetic field of the rotor. This requires both direct and quadrature axes to be rotating ahead of the rotor at a slip angle, as shown by (D.10).

$$\omega_e = \omega_r + \omega_{sl} \quad (\text{D.10})$$

For control, the stator flux component of the current,  $i_{ds}$ , must be aligned with the direct axis, and the torque producing current,  $i_{qs}$ , must be aligned on the quadrature axis. Therefore, the rotor flux component of the current on the quadrature axis and its derivative must be zero as shown by (D.11) and (D.12).

$$\lambda_{qr} = 0 \quad (\text{D.11})$$

$$\frac{d}{dt}\lambda_{qr} = 0 \quad (\text{D.12})$$

The machine rotor voltages in the direct and quadrature axes are also set to zero since there is no external voltage applied to the rotor windings and the squirrel cage rotor has end bars that are short-circuiting the rotor conductors. Using (D.9) to create the rotor voltage equations and rearranging (D.5)-(D.8) into current equations, (D.13) and (D.14) can be created.

$$v_{qr} = 0 = \frac{d}{dt}\lambda_{qr} + \frac{R_r}{L_r}\lambda_{qr} - \frac{L_m R_r}{L_r}i_{qs} + (\omega_e - \omega_r)\lambda_{dr} = -\frac{L_m R_r}{L_r}i_{qs} + (\omega_e - \omega_r)\lambda_{dr} \quad (\text{D.13})$$

$$v_{dr} = 0 = \frac{d}{dt}\lambda_{dr} + \frac{R_r}{L_r}\lambda_{dr} - \frac{L_m R_r}{L_r}i_{ds} - (\omega_e - \omega_r)\lambda_{qr} = \frac{d}{dt}\lambda_{dr} + \frac{R_r}{L_r}\lambda_{dr} - \frac{L_m R_r}{L_r}i_{ds} \quad (\text{D.14})$$

The motor flux time constant can be found by rearranging (D.14) as shown by (D.15)

$$\left( \frac{L_r}{R_r} \frac{d}{dt} \lambda_{dr} + \lambda_{dr} \right) = L_m i_{ds} \quad (\text{D.15})$$

If the flux remains constant, then (D.15) is reduced to (D.16).

$$\lambda_{dr} = L_m i_{ds} \quad (\text{D.16})$$

(D.13) can be rearranged to obtain the motor slip as shown by (D.17).

$$(\omega_e - \omega_r) = \omega_{sl} = \frac{L_m R_r}{L_r \lambda_{dr}} i_{qs} = \frac{R_r i_{qs}}{L_r i_{ds}} \quad (\text{D.17})$$

The torque equation for the motor is represented by (D.18) where  $P$  is the number of motor pole pairs.

$$T_e = \frac{3P}{2} (\lambda_{ds} i_{qs} - \lambda_{qs} i_{ds}) = \frac{3P}{2} \frac{L_m^2}{L_r} (i_{ds} i_{qs}) \quad (\text{D.18})$$

## D.2 D-Axis Rated Flux Derivation

From Figure D.1, (D.6) and (D.8) were derived which when combined together create (D.19).

$$\lambda_{ds} = i_{ds} \left( \frac{L_s L_r - L_m^2}{L_r} \right) + \frac{L_m}{L_r} \lambda_{dr} \quad (\text{D.19})$$

At steady state,  $\lambda_{dr} = L_m i_{ds}$  and (D.19) can be simplified to (D.20).

$$\lambda_{ds} = i_{ds} L_s \quad (\text{D.20})$$

Since no torque is being produced,  $i_{qs} = 0$  and thus  $\lambda_{qs} = 0$  which results in the quadrature axis stator motor voltage equation shown by (D.21).

$$v_{qs} = \omega_e \lambda_{ds} = \omega_e i_{ds} L_s \quad (\text{D.21})$$

Rearranging for  $i_{ds}$  results in (D.22)

$$i_{ds} = \frac{v_{qs}}{\omega_e L_s} \quad (\text{D.22})$$

Using an amplitude invariant form of the Park's transform results in (D.23).

$$i_{ds} = \frac{\sqrt{\frac{2}{3}} V_{ll,rms}}{2\pi f_{rated}(L_m + L_{ls})} = \frac{\sqrt{\frac{2}{3}} \times 49.7}{2 \times \pi \times 137.1 \times (1.055mH + 25.20\mu H)} = 43.61Apk \quad (\text{D.23})$$

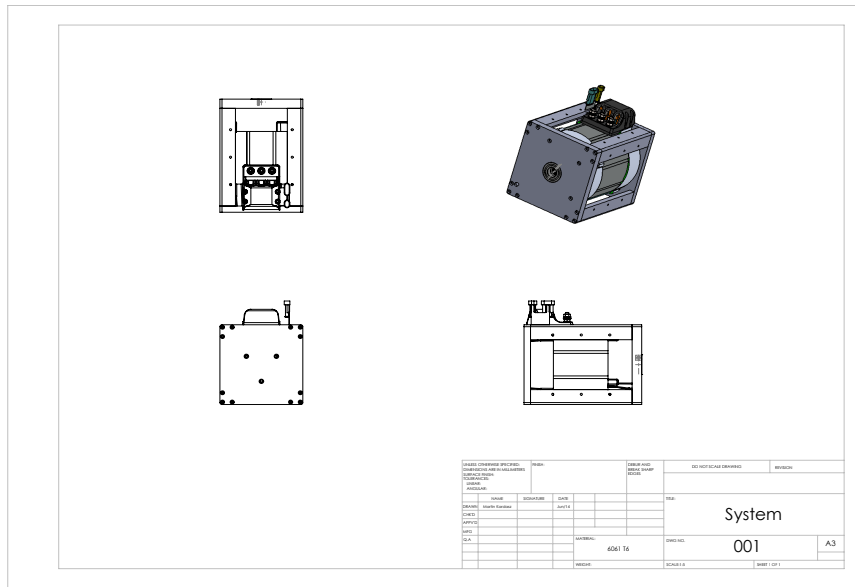
# Appendix E

## Mechanical Design of Motor Cradle and Shaft

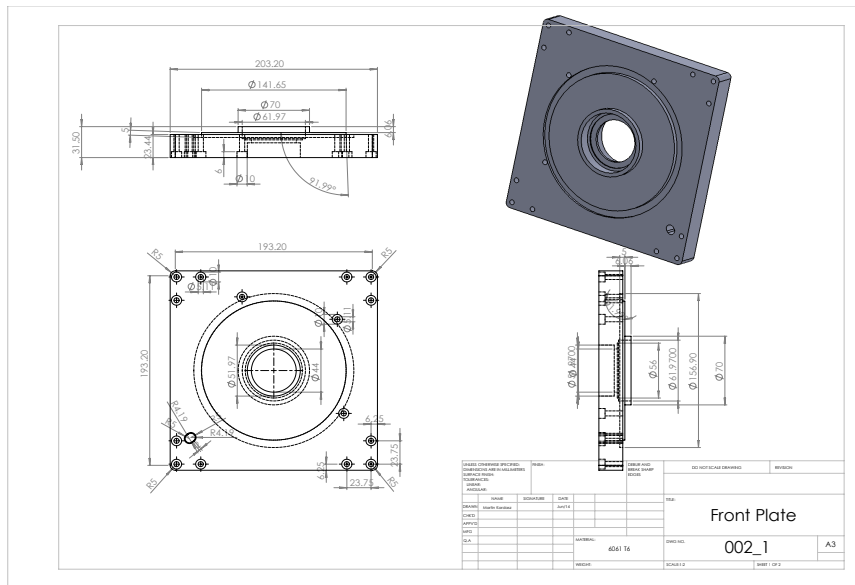
### E.1 Motor Cradle Mechanical Drawings

The mechanical drawings required to create the ACX-2043 motor cradle are shown in Figure E.1. The complete motor cradle system image is shown in Figure E.1(a). The front plate is divided into two images shown in Figures E.1(b) and E.1(c). The back plate is shown in Figure E.1(d). The two brackets used to connect the front and back plates together, due to a protrusion in the motor casing, are shown in Figures E.1(e) and E.1(f). Finally, the mechanical coupling that connects the motor rotor to the bearings and the front plate is shown in Figure E.1(g).

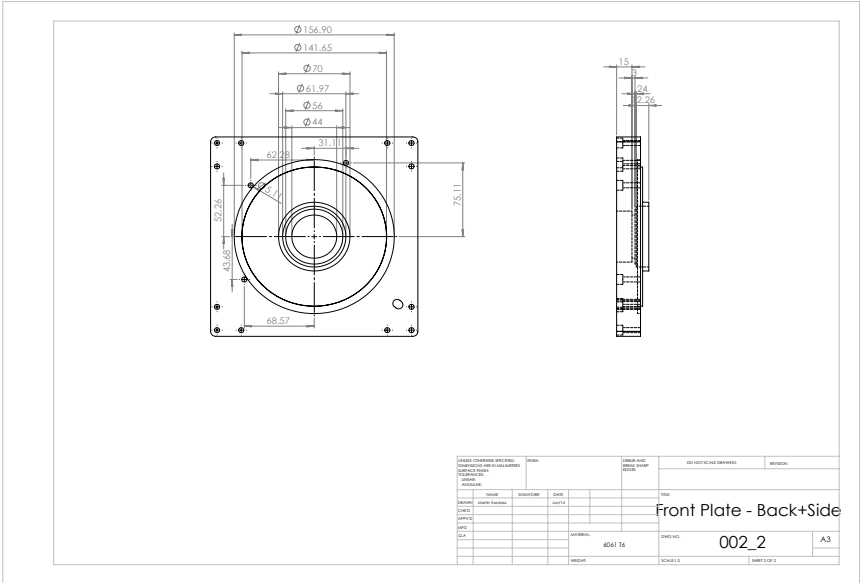




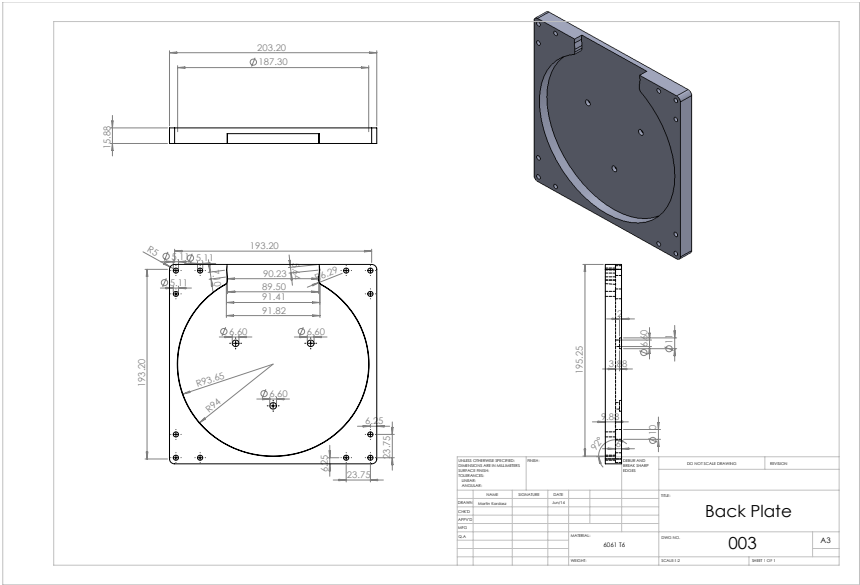
(a) Motor Cradle System Image



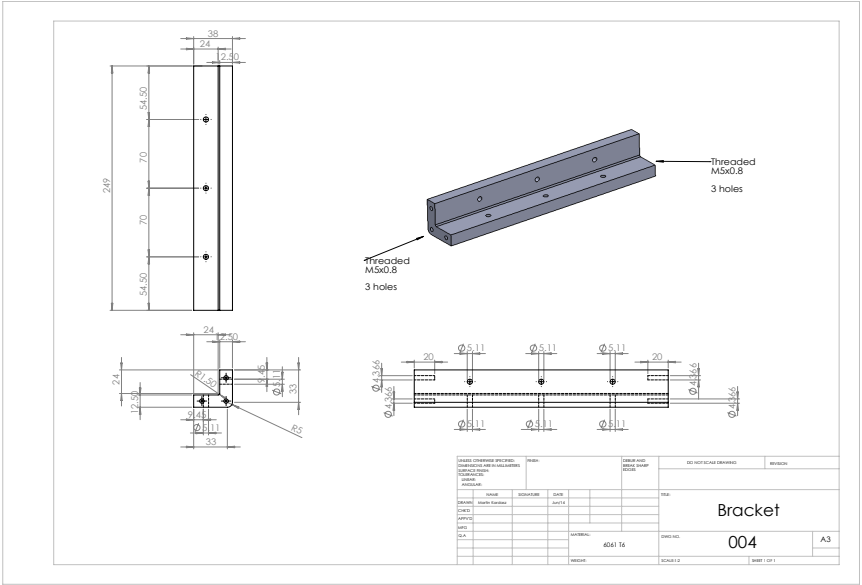
(b) Motor Cradle Front Plate First Part



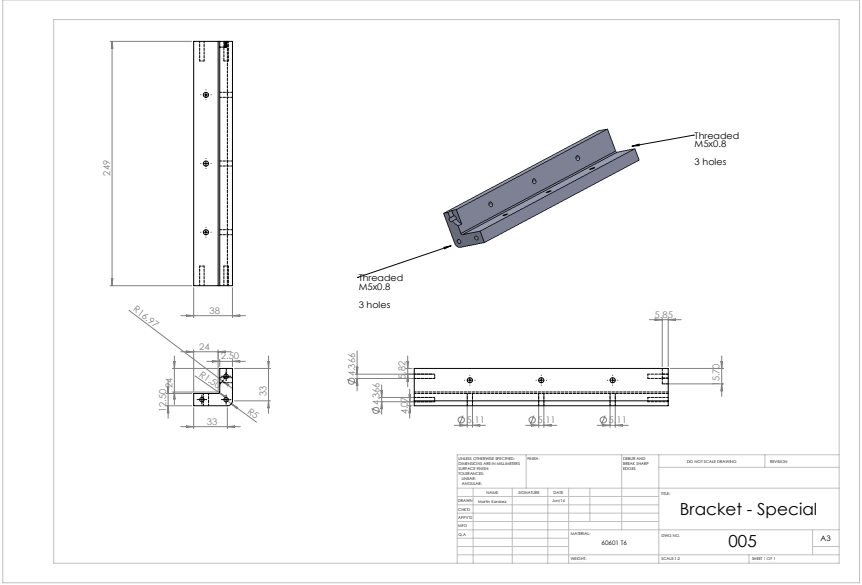
(c) Motor Cradle Front Plate Second Part



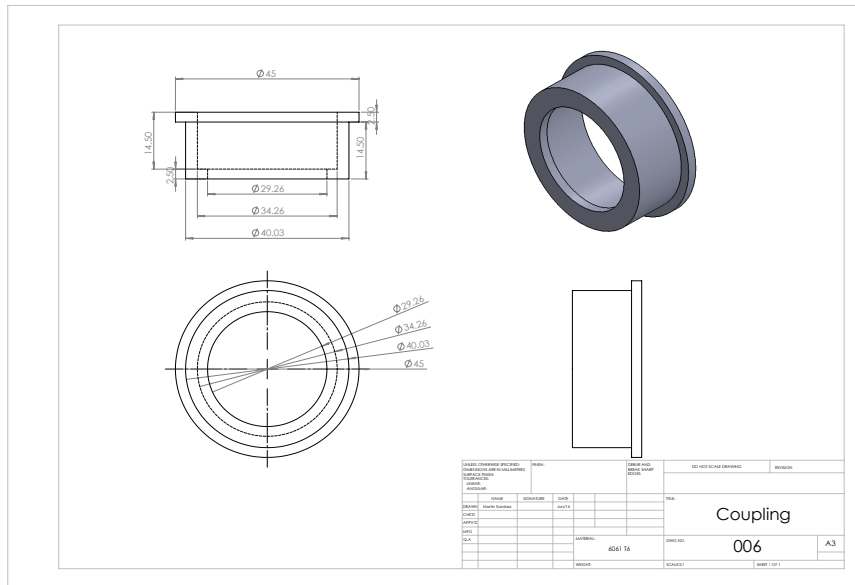
(d) Motor Cradle Back Plate



(e) Motor Cradle Bracket



(f) Motor Cradle Special Bracket



(g) Motor Cradle Coupling

Figure E.1: Motor Cradle Mechanical Drawings

## E.2 Motor Shaft Mechanical Drawings

The mechanical drawing to recreate the mechanical shaft that is used to connect the motors together is shown in Figure E.2. Spline details and shaft keying are also shown in detail.

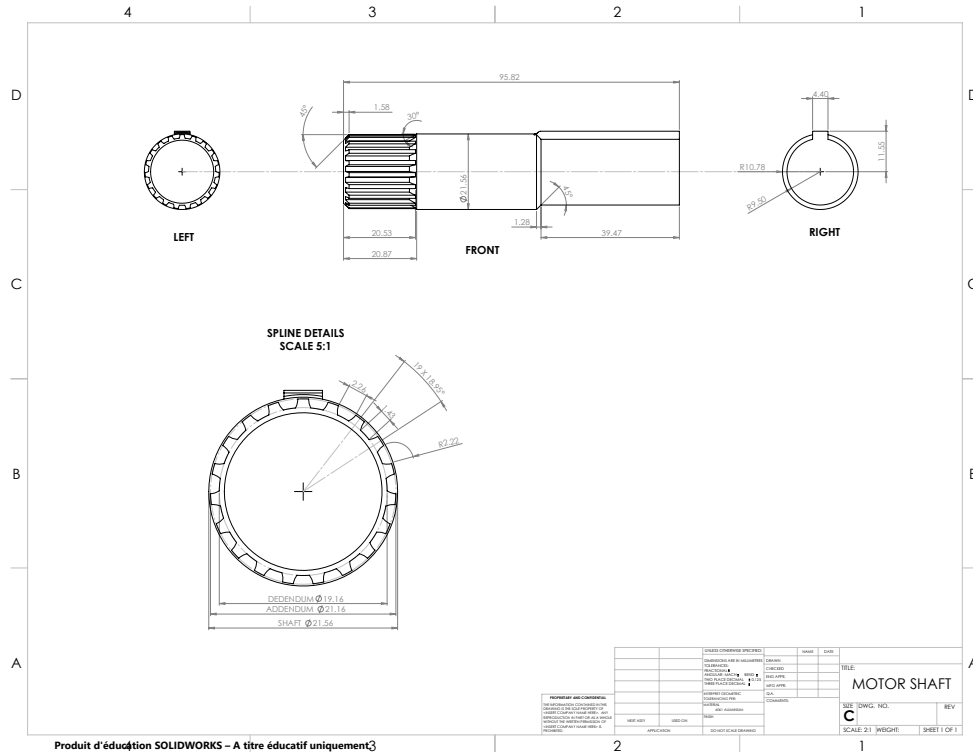


Figure E.2: Motor Shaft

# Appendix F

## AC/DC Module Soft-Start Circuit Derivations

### F.1 Capacitor Discharge Level

The maximum resistance that can be used to discharge all the energy of the test bed within the design specification time that is considered safe is evaluated in this Appendix.

The design specifications are shown:

- $V_{high} = 350V$  is the high-side DC voltage
- $V_{low} = 100V$  is the low-side DC voltage
- $V_{safe} = 5V$  is the system safe DC voltage
- $C_{high} = 750\mu F$  is the capacitance on the high-side DC bus
- $C_{low} = 2mF$  is the capacitance on the low-side DC bus
- $t_{SlowDischarge,max} = 10s$  is the maximum time requirement to allow the system to discharge normally to the safe voltage level
- $t_{FastDischarge,max} = 0.5s$  is the maximum time requirement to allow the system to discharge in an emergency to the safe voltage level

The standard resistor-capacitor (RC) discharge equation used is given by (F.1).

$$V_c = V_s \times e^{\frac{-t}{RC}} \quad (\text{F.1})$$

In (F.1),  $V_c$  is the capacitor voltage,  $V_s$  is the supply voltage,  $t$  the time since the voltage has been removed, and  $RC$  the time constant,  $\tau$ , of the RC discharge circuit. The variables can be renamed in a manner that fits the requirements and according to the design specifications.

The problem is divided into two sections, where initially just the capacitor on the high-side DC bus is discharged until the voltage level is that of the low-side DC bus. At this point, the total capacitance seen by the resistor will be the sum of all capacitances. Therefore the total time is the sum of the times of both sections. The three equations used are (F.2), (F.3), and (F.4) with the parameters staying the same as those described in the design specifications.

$$V_{low} = V_{high} \times e^{\frac{-t_{high}}{RC_{high}}} \quad (\text{F.2})$$

$$V_{safe} = V_{low} \times e^{\frac{-t_{high+low}}{RC_{high+low}}} \quad (\text{F.3})$$

$$t_{max} = t_{high} + t_{high+low} \quad (\text{F.4})$$

Rearranging (F.2) and (F.3) for time yields (F.5) and (F.6).

$$t_{high} = -RC_{high} \times \ln \left( \frac{V_{low}}{V_{high}} \right) \quad (\text{F.5})$$

$$t_{high+low} = -RC_{high+low} \times \ln \left( \frac{V_{safe}}{V_{low}} \right) \quad (\text{F.6})$$

Placing these two equations into (F.4) results in (F.7).

$$t_{max} = -R \left[ C_{high} \times \ln \left( \frac{V_{low}}{V_{high}} \right) + C_{high+low} \times \ln \left( \frac{V_{safe}}{V_{low}} \right) \right] \quad (\text{F.7})$$

Finally rearranging for maximum R yields (F.8).

$$R = -\frac{t_{max}}{\left[ C_{high} \times \ln\left(\frac{V_{low}}{V_{high}}\right) + C_{high+low} \times \ln\left(\frac{V_{safe}}{V_{low}}\right) \right]} \quad (\text{F.8})$$

To meet the normal discharge time requirement, a maximum resistance of  $1090\Omega$  is found as shown in (F.9).

$$R_{max,normal} = -\frac{10}{\left[ 750\mu \times \ln\left(\frac{100}{350}\right) + 2750\mu \times \ln\left(\frac{5}{100}\right) \right]} = 1090\Omega \quad (\text{F.9})$$

To meet the emergency discharge time requirement, a maximum resistance of  $54.48\Omega$  is found as shown in (F.10).

$$R_{max,emergency} = -\frac{0.5}{\left[ 750\mu \times \ln\left(\frac{100}{350}\right) + 2750\mu \times \ln\left(\frac{5}{100}\right) \right]} = 54.48\Omega \quad (\text{F.10})$$



# Appendix G

## Fiber Optic BOM

### G.1 Fiber Optic Transmitter BOM

Table G.1: Fiber Optic Transmitter BOM

Parameter	Value	Schematic Reference
Fiber Optic Transmitter	Broadcom HFBR-1521Z	FiberOpticTransmitter1, FiberOpticTransmitter2
Inverter	Texas Instruments SN74HC04N	Buffer
Inverter Socket	Assmann WSW Components A 14-LC-TT	BufferSo
Transistor	NPN, 40V, 0.2A, ON Semiconductor 2N3904BU	Q1, Q2
Resistor	82R, 0.25W, 5%, Stackpole CF14JT82R0	Rb1, Rb2
Resistor	430R, 0.25W, 5%, Stackpole CF14JT430R	Rc1, Rc2
Fiber Optic Plug	Broadcom HFBR-4501Z	Wire attachment x2
Capacitor	150 $\mu$ F, 35V, Aluminum, Panasonic EEU-FM1V151	C1, C2
Terminal Block	2 Position, 5mm Pitch, Phoenix Contact 1935161	J1, J2, J3

## G.2 Fiber Optic Receiver BOM

Table G.2: Fiber Optic Receiver BOM

Parameter	Value	Schematic Reference
Fiber Optic Receiver	Broadcom HFBR-2521Z	FiberOpticReceiver1, FiberOpticReceiver2
Inverter	Texas Instruments SN74HC04N	Buffer
Inverter Socket	Assmann WSW Components A 14-LC-TT	BufferSo
Isolated Power Supplies	Powerex Inc. VLA106-15242	VLA106_1, VLA106_2
Optoisolator	Broadcom ACNW3130-000E	Opto1, Opto2
Optoisolators Socket	On Shore Technology ED08DT	OptoSo1, OptoSo2
LED	Green LED, Vf=2.2V, Kingbright WP7113GD	DLED
Resistor	220R, 0.25W, 5%, Stackpole CF12JT220R	RLED
Fiber Optic Plug	Broadcom HFBR-4501Z	Wire attachment x2
Capacitor	390uF, 20%, 35V, Rubycon 35ZLH390MEFC8X20	Cap1, Cap2, Cap3, Cap4, Cap5, Cap6
Zener Diode	Vz=16V0, 1W, ON Semiconductor 1N4745ATR	Z2, Z4
Zener Diode	Vz=8V2, 1W, Nexperia 1N4738A,113	Z1, Z3
Capacitor	10nF, 50V, X7R, Kemet C317C103K5R5TA	C1-C4
Capacitor	150μF, 35V, Aluminum, Panasonic EEU-FM1V151	C
Terminal Block	2 Position, 5mm Pitch, Phoenix Contact 1935161	J1, J2, J3